12-17-2015

Spectroscopy of Quasibound and Long-Range Rydberg States of Ultracold 85Rb2

Ryan A. Carollo
University of Connecticut, carollo@phys.uconn.edu

Spectroscopy of Quasibound and Long-Range Rydberg States of Ultracold $^{85}Rb_2$

Ryan A Carollo, Ph.D.

University of Connecticut, 2015

Ultracold atomic physics offers an experimentalist the opportunity to perform sensitive tests and measurements that are not possible at higher temperatures. In this case it allows for access to molecular states, through photoassociation, that are inaccessible to conventional techniques. We use photoassociation to measure quasi-bound levels of the $2\,^1\Sigma_g^+$ state of $^{85}Rb_2$. With these data, we examine a coupling between the short-range Hund's case (c) $2\,(0_g^+)$ component and the long-range $2\,(1_g)$ state, which corresponds to the $1\,^1\Pi_g$ state. A second experiment studies the mechanism of short-range photoassociation and finds our simple model to have strong predictive power. In a third experiment, we photoassociatively form vibrationally excited $a\,^3\Sigma_u^+$ molecules. We then excite these molecules using a frequency-doubled pulse-amplified CW laser to create low-n long-range Rydberg states of $^{85}Rb_2$. Autoionization and ion detection of these states gives high-resolution spectra, which are compared to theoretical potential curves.

Spectroscopy of Quasibound and Long-Range Rydberg States of Ultracold $^{85}Rb_2$

Ryan A Carollo

B.A., Williams College, 2005

M.S., University of Connecticut, 2009

A Dissertation

Submitted in Partial Fullfilment of the

Requirements for the Degree of

Doctor of Philosophy

at the

University of Connecticut

2015

APPROVAL PAGE

Doctor of Philosophy Dissertation

Spectroscopy of Quasibound and Long-Range Rydberg States of Ultracold $^{85}Rb_2$

Presented by

Ryan A Carollo,

Major Advisor 
W.C. Stwalley

Associate Advisor 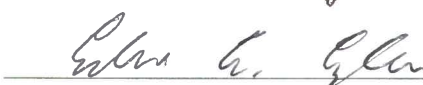
E.E. Eyler

Associate Advisor 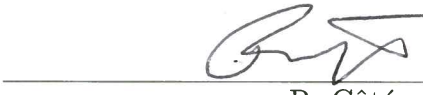
R. Côté

University of Connecticut

2015

To my family

"It ended up taking three years.

They had planned for one. It took longer because things kept breaking and needed to be fixed."

–Neal Stephenson, *Seveneves*

ACKNOWLEDGEMENTS

Doing the research that went into this dissertation has been a long and winding road, and there are many people who have helped me along the way. First, I want to thank my advisor, William Stwalley. His depth of knowledge and intuition for spectroscopy have been a wonderful resource, and have helped to greatly expand my own physical intuition. Next, I would like to thank the co-principle investigators on the ultracold molecules experiment, Edward Eyler and Phillip Gould. Dr. Eyler provided many valuable insights on the experimental apparatus, and both he and Dr. Gould were helpful in analyzing data. I would also like to thank my dissertation co-advisor, Robin Côté.

Graduate school is always difficult and trying, but it is made more pleasant by good company. I want to thank my long-time labmates Michael Bellos and Jayita Banerjee. The long hours Michael and I spent debugging the large UHV chamber were some of the best learning experiences I had. Our two-year postdoc Dave Rahmlow provided invaluable assistance in advancing the level of technology in the lab. I also could not have made the experiments run, or interpreted all of my data, without the assistance of Jennifer Carini.

I enjoyed many hours working through atomic physics problem sets with Jason Byrd, and without the fellowship of Richard Crudo through problem sets and prelim studying, I could not have even made it to lab work. I also deeply appreciate the shop talk and knowledge-sharing of my fellow AMO graduate students Marco Ascoli, Doug Goodman, James Wells, Leland Aldridge, Vince Tagliamonti, and Chad Rogers.

Support and encouragement from Dave Perry were vital to solving many problems. I must also thank Alan Chasse for his skill and advice in building new parts for the experiments. My regular discussions on astronomy and academia with Cynthia Peterson have always been a pleasure and a welcome relief from the challenges of experiments. Physics discussions with Win Smith have also been a pleasure. The support and teaching staff in the department have always been both sympathetic and helpful, so my thanks go out to Kim Giard, Dawn Rawlinson, Carol Artacho Guerra, Michael Rapposch, Heather Osborne, Alessandra Introvigne, Micki Bellamy, and Jeanette Jamieson.

Many thanks to my friends near and far who supported me through this long process, especially those who thought I would always be a student, but didn't mind. Amanda Daddona has been remarkably supportive, and spending time with her and her family has made this journey far more pleasant. My thanks to Anna Grosslein and Merli Guerra, for enriching my dancing life. And thanks to Karen Locke, for some wonderful adventures that kept me grounded in the real world.

Finally, to my family, and especially my parents: thank you for all your love and support on this long journey. It feels good to have arrived.

TABLE OF CONTENTS

LIST OF FIGURES

LIST OF TABLES

Chapter 1

Introduction

This chapter will give background on ultracold molecular physics. The general outlines of the field will be described, as well as foundational techniques used in all of our experimental work. Some of the theory and notation of molecular spectroscopy will also be described.

1.1 Cold Molecules Background

This section contains background information on the scientific uses of cold molecules and the techniques we use to create them.

1.1.1 Laser Cooling and Trapping

The foundation of all of our experimental work is our ^{85}Rb magneto-optical trap, or MOT. MOTs were first developed by Raab *et al.* in 1987 in the group of Steven Chu, for which Chu shared the 1997 Nobel Prize in Physics with Bill Phillips and Claude Cohen-Tannoudji [1,2]. The physics of the MOT are well-explained in Ref. [3] by Metcalf and van der Straten. A brief summary of their operation will be given here.

Perhaps the best place to begin describing a MOT is with a simpler technique called optical molasses [4]. Optical molasses is a technique that achieves

atomic cooling, but not trapping. In one dimension, two counter-propagating laser beams are detuned below a strong atomic cycling transition (usually the D_2 line in the alkali metals) by ~ 1 natural linewidth. If an atom in the beams travels toward one beam, it will see those photons Doppler-shifted closer to resonance, while photons from the opposing beam will be Doppler-shifted further from resonance. The atom will have a higher probability of absorbing the blue-shifted, near-resonance photons.

The absorbed photon carries a momentum of $\vec{p} = \hbar\vec{k}$, which is opposite the atom's momentum by design. When the atom re-emits that photon, it will be in a random direction, covering the full 4π steradians of the sphere isotropically. Thus over many absorption-emission cycles, an atom loses one $\hbar\vec{k}$ unit of momentum per cycle (and also loses $\hbar\omega_\gamma$ in energy), while the spontaneously emitted photon kicks average to zero.

Reducing the atom's momentum is a cooling effect, which occurs when the atom moves toward either beam. If pairs of beams are aligned along all three Cartesian axes, the atom will be cooled when moving in *any* direction. The primary limit on this cooling is the "random walk" in momentum space accumulated by the spontaneous emission of photons. This is called the Doppler limit. Further discussion of optical molasses and the Doppler limit can be found in Chapter 7 of Ref. [3].

A magneto-optical trap adds a quadrupole magnetic field, and circular polarizations, to an optical molasses. Note that the magnetic field does *not* cause direct magnetic trapping of neutral atoms, which would require much stronger fields to be effective. Instead, the magnetic gradient creates a position-dependent Zeeman shift that, combined with appropriate circular polarizations, creates a

position-dependent restoring force. This force is zero at the physical location where the B-field is zero, and increases with increasing distance. Chapter 11.4 of Ref. [3] has full details on this valuable technique.

1.1.2 Cold Molecules

Cold and ultracold molecules have been a subject of ever-increasing interest for well over two decades. Definitions of what "ultracold" means vary, but generally temperatures below 1 mK are considered ultracold, while those below 1 K are cold molecules. Some groups working from Bose-Einstein condensate (BEC) [5,6] precursor atoms only consider molecules to be ultracold if they are at temperatures well below 1 μK.

Our group creates ultracold molecules (both Rb_2 and KRb) through photoassociation. This technique will be explored in more detail in Section 1.1.3. An alternative method of creating ultracold molecules is to form them by magnetoassociation through a Feshbach resonance. If this is followed by stimulated Raman adiabatic passage (STIRAP) [7], ultracold molecules can be transferred to their absolute ground state [8] or triplet rovibrational ground state [9].

There are also techniques for cooling molecules from ambient temperatures. A very versatile method of cooling is buffer-gas cooling, which is effective for both atoms and molecules [10]. This technique has also been used to Bose-condense metastable helium atoms, and could be extended to molecules [11]. For dipolar molecules, the Stark effect can be used to slow beams of molecules in a linear decelerator with a time-varying electric field [12].

At the moment the most limited method for attaining ultracold molecules, but yet the most exciting, is direct laser cooling and trapping. This is much more

difficult in molecules than in atoms because of the many decay paths available, which make finding cycling transitions difficult. Nonetheless, progress has been made. A molecular MOT was first proposed in [13], and laser cooling was demonstrated in [14]. A 2-D MOT was achieved in [15], and finally a full 3-D MOT was demonstrated in [16].

1.1.3 Photoassociation (PA)

The use of photoassociation as a technique for cold and ultracold molecule production began shortly after the development of cold atom trapping with the MOT. The theory of this new technique was developed in Ref. [17]. There are a number of excellent reviews that summarize the state of the field over time, including Refs. [18–20]. Ref. [21] is a review of photoassociation theory.

At a basic level, photoassociation is an electronic excitation during the collision of two atoms that yields an excited-state molecule

$$\mathrm{Rb} + \mathrm{Rb} + \gamma_1 \rightarrow \mathrm{Rb}_2^* \,, \tag{1.1}$$

where Rb_2^* is electronically excited. The electronically excited molecular state will spontaneously emit a photon to decay to a potential that usually asymptotically correlates to the atomic ground-state energy

$$\mathrm{Rb}_2^* \rightarrow \mathrm{Rb}_2 + \gamma_2 \,, \tag{1.2}$$

or to free ground-state atoms with excess kinetic energy ("hot" atoms)

$$\mathrm{Rb}_2^* \rightarrow \mathrm{Rb} + \mathrm{Rb} + \gamma_3 \,. \tag{1.3}$$

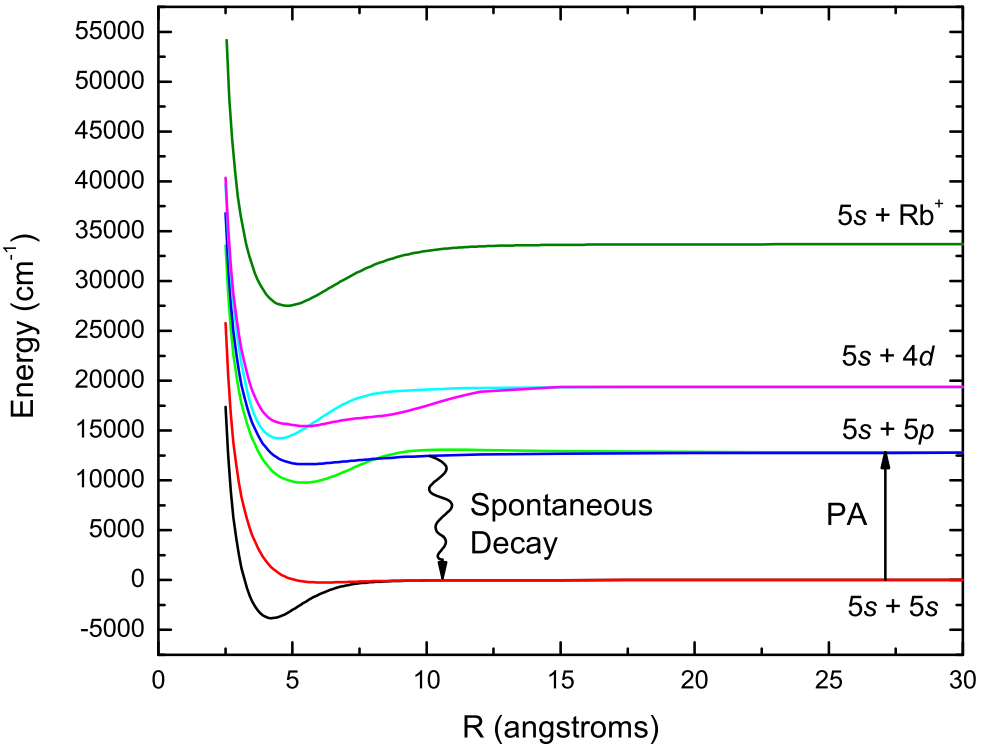

Fig. 1.1: An example of photoassociation. Here, a laser excites transitions at long range to the red of the $5s + 5p$ asymptote (lower in energy). The excited-state molecule spontaneously decays to the $a\,^3\Sigma_u^+$ state, emitting a photon.

Here we use homonuclear Rb_2 as an example, but heteronuclear molecules such as KRb are equally possible, as in [22,23]. It is important to note that excitation can occur to repulsive as well as attractive excited-state potentials [24], although as the atoms are not *associated* after the collision, this cannot properly be called photoassociation. An example of a photoassociation process is shown in Fig. 1.1.

Ultracold photoassociation was one of the earliest advances in molecular spectroscopy to be built upon the success of neutral atom cooling and trapping, being described only two years after the announcement of the MOT [17]. It pro-

vides numerous advantages compared with traditional spectroscopic techniques.

One of the chief advantages of PA spectroscopy is that free $\rightarrow$ bound transitions can have linewidths comparable to bound $\rightarrow$ bound transitions due to the narrow thermal distribution of ultracold samples. As the atomic collisions are truly quantum-mechanical and only low-ℓ partial waves are involved, PA also creates molecules that are slowly rotating, as opposed to the rapidly-rotating molecules of hot samples. PA can also directly access states of many symmetries, not simply those allowed by selection rules from the ground X state [20].

Another of its advantages is that PA can access very long-range molecules. At these large internuclear distances the potentials are governed by the C_3, C_6, C_8, and C_{10} long-range coefficients that are determined by atomic properties rather than more-complex chemical interactions. This reduction in complexity allows precise atomic parameters to be measured [20]. Also of great importance, the molecules that are formed by PA are also translationally ultracold, as they have kinetic energy similar to the atoms from which they are formed. This allows the trapping and further study of these molecules, opening many new experimental possibilities. All of the work in this dissertation is based on PA followed by further manipulation of the resulting ultracold molecules.

1.2 Hund's Cases

The various angular momenta present in a diatomic molecule can couple together in several different ways, each of which defines a different basis set for molecular potentials and has its own set of good quantum numbers. There are five different coupling cases, called Hund's cases, and are denoted as case (a) through case (e). Case (a) and (c) are the only cases where the Born-Oppenheimer separation

of nuclear and electronic motion can be used to calculate true nuclear potential energy curves [25,26]. As case (a) and case (c) are of primary interest to our work, I will describe them here. Detailed descriptions of the other Hund's cases may be found in many references, including [25–27].

Hund's case (a) is generally used to describe short-range molecules. Angular momenta **L** and **S** are each coupled to the internuclear axis, which they precess around. Their projections on the internuclear axis, Λ and Σ, are good quantum numbers, as is their sum, Ω. The nuclear rotation vector, **R**, and the vector $\mathbf{\Omega}$ are coupled to form the total angular momentum vector **J**. In total, the good quantum numbers for case (a) are: Λ, S, Σ, J, Ω, and M_J. Case (a) molecules are designated by the standard term symbol $^{2S+1}\Lambda^{(\pm)}_{(u/g),\Omega}$. This Hund's case is a good description when $A\Lambda$ is much greater than BJ, where A is the spin-orbit coupling constant and B is the rotational constant [25].

Hund's case (c) is used to describe intermediate and long-range molecules. In this case, **L** and **S** couple to each other (rather than to the internuclear axis) to form $\mathbf{J}_a$. Their individual projections Λ and Σ are not good quantum numbers, but the sum Ω (which is the projection of $\mathbf{J}_a$) is well-defined. The total angular momentum **J** remains $\mathbf{R}+\mathbf{\Omega}$, as in case (a). Good quantum numbers for case (c) are: J_a, J, Ω, and M_J [25]. The states of case (c) are designated solely by their Ω value, an index that counts similar-Ω states beginning with the ground state, parity, and nuclear inversion symmetry, if appropriate, e.g. $2\,(0^+_g)$.

1.3 Selection Rules

As discussed in Ref. [20], identical cold atoms collide in a statistical mixture of states, including singlet-*gerade* and triplet-*ungerade* symmetries. This makes it

possible to perform photoassociation to many different states, provided that the Franck-Condon factor and transition dipole moment are favorable.

All quantum-mechanical transitions are described by matrix elements of the form $\left\langle \psi_2 \left| D(\vec{R}) \right| \psi_1 \right\rangle$. Without $D(\vec{R})$, the matrix element $\langle \psi_2 | \psi_1 \rangle = 0$ for $\psi_2 \neq \psi_1$, and for $\psi_2 = \psi_1$, $\langle \psi_2 | \psi_1 \rangle = 1$. With $D(\vec{R})$, the dipole moment operator, certain transitions (matrix elements between non-identical final and initial states) are possible. The mathematical conditions that allow a non-zero matrix element are called "selection rules". For electric dipole (E1) transitions, the following selection rules apply:

1. In homonuclear dimers, transitions must change inversion symmetry, i.e. $g \rightarrow u$ or $u \rightarrow g$ (due to the electric dipole operator $D(\vec{R})$ having u symmetry), and it should be noted that this selection rule is extremely strong. The regime where it is violated is in the case where hyperfine coupling becomes strong compared to the binding energy, such as in ground-state singlet-triplet mixing [28,29].

2. In both Hund's case (a) and case (c), $\Delta\Omega = 0, \pm 1$ must be obeyed. Hund's case (a) must follow additional rules of $\Delta\Lambda = 0, \pm 1$ and $\Delta\Sigma = 0$.

3. In case (a), only singlet $\rightarrow$ singlet or triplet $\rightarrow$ triplet ($\Delta S = 0$) are allowed transitions, although this selection rule is violated as spin-orbit coupling increases in heavier atoms [30] and Hund's case (a) changes to Hund's case (c), where L and S are no longer good quantum numbers.

In terms of vibrational and rotational transitions, no E1 ro-vibrational transitions are allowed within a single given potential for a homonuclear dimer. If there

is a simultaneous electronic transition, ro-vibronic transitions are E1 allowed. For such a ro-vibronic transition, the selection rules are:

1. $\Delta J = \pm 1$. $\Delta J = 0$ is also allowed if $\Lambda \neq 0$ (in case (a)) or $\Omega \neq 0$ (in case (c)).

2. $\Delta M_J = 0, \pm 1$

Vibrationally, any transition is allowed between different potentials if there is a nonzero overlap of the two vibrational wavefunctions (one in each potential), *i.e.* a nonzero Franck-Condon Factor $|\langle \psi_{v'} | \psi_{v''} \rangle|^2 \neq 0$ (described in more detail in Section 1.4), where v' is the upper vibrational level and v'' is the lower vibrational level. The transition strength will depend on the details of the two potentials [30].

1.4 Franck-Condon Factors (FCFs)

Nearly all of the molecular research we undertake involves transitions between different electronic states. These can be free $\rightarrow$ bound, bound $\rightarrow$ bound, bound $\rightarrow$ free, or free $\rightarrow$ free transitions. The transition probability is proportional to the square of the transition moment, $\left\langle \psi'_{v',J'} \right| D(R) \left| \psi''_{v'',J''} \right\rangle$, where $D(R)$ is the R-dependent electronic transition dipole moment. However, the electronic transition dipole moment is often unknown and sometimes difficult to determine from experiment or to calculate. As it is often slowly-varying with R, it is therefore useful to approximate the dipole moment as 1 for all values of R, giving us an element $\left\langle \psi'_{v',J'} | \psi''_{v'',J''} \right\rangle$. This is the overlap integral of the two wavefunctions, $\int \psi^*_{v',J'}(R) \psi_{v'',J''}(R)\, dR$, which is fairly easy to calculate given the potential energy curves of the two states. For the purposes of this dissertation, this quantity squared is called the Franck-Condon factor, usually abbreviated as FCF, and is

proportional to the transition probability. Thus we have FCF $= \left|\left\langle \psi'_{v',J'} | \psi''_{v'',J''} \right\rangle\right|^2$. This definition is the one used by Robert LeRoy in his programs LEVEL 8.0 and 8.2 [31,32].

In addition to being a simple method to estimate transition probabilities, FCFs can also be used to estimate the fraction of molecules lost in bound $\rightarrow$ free transitions, including transitions to repulsive potentials. This is because the sum of FCFs from one level of a given bound state across all target levels of a second state (including levels in the dissociative continuum) must be 1 by mathematical identity. If the bound-bound FCFs sum to less than one, the remaining fraction involves transitions to free states.

In addition to FCFs, another important concept is the Franck-Condon principle, which is that electronic transitions happen quickly compared to nuclear motion. It is similar to the Born-Oppenheimer approximation that assumes slow-moving heavy nuclei, separates electronic and nuclear wavefunctions, and allows the electronic component to be represented by static potentials. This principle implies that electronic transitions are always vertical on a potential energy plot. Combined with the FCF, these concepts imply that transitions are most likely to occur where large maxima and minima in the upper and lower states overlap. Areas of high transition probability can be quickly found by examination of potentials, comparing the outer turning points of various vibrational and electronic states to find matches in internuclear distance. This idea and others are developed and applied in Ref. [33].

1.5 Resonance-Enhanced Multiphoton Ionization

Resonance-enhanced multiphoton ionization (REMPI) is a highly useful and important technique in our work. A brief description of REMPI is given in Chapter 3.3.3 of Ref. [34]. A more extensive overview is given in Ref. [35]. The technique and a few of its uses are outlined here.

Generally, a multiphoton process will be weaker than a single-photon process, unless the intensity is extremely high (each excitation rate scales as I^n, where I is the laser intensity, and n is the photon order of the process, e.g. I^2 for a two-photon excitation). This means that higher-order excitations are likely to produce low excitation rates and weak signals. If an intermediate state exists that is resonant with the laser frequency, however, the process resembles a double-resonance, or $1+1$, excitation and proceeds more rapidly, even though only a single color is used.

Scanning the REMPI laser, one obtains a spectrum that contains information about both the initial and intermediate states. Our spectra typically have closely-spaced vibrational levels in the initial ($X\,^1\Sigma_g^+$ or $a\,^3\Sigma_u^+$) states, and more-widely spaced vibrational levels in the intermediate state. Both of these vibrational manifolds appear, with the intermediate state in the intuitive order (higher levels at higher excitation energy), and the initial states reversed (higher levels appear at lower energy). An example of this type of spectrum is shown in Fig. 3.2, originally published in Ref. [36]. In that figure, a similar REMPI scan is performed over three PA levels, producing similar spectra, with differences that reflect FCFs from the PA level to the $a\,^3\Sigma_u^+$ state, and from the $a\,^3\Sigma_u^+$ state to the $2\,^3\Sigma_g^+$ state.

In addition to enhancing ionization rates, REMPI can also provide access

to forbidden states. If a particular intermediate state is forbidden by one-photon transitions, REMPI with a two-photon resonance to that state may enable study of it. The high efficiency of REMPI can also allow transition to intermediate states that are forbidden by weaker selection rules such as the singlet $\nleftrightarrow$ triplet selection rule. We typically see $1 + 1$ excitation through singlet and triplet intermediate states with equal strength, as long as the $g \leftrightarrow u$ selection rule is obeyed.

1.6 Contents of This Dissertation

This dissertation focuses on photoassociation spectroscopy of ultracold $^{85}Rb_2$ dimers. In this chapter we have given some motivation, background material, and references. In Chapter 2, a detailed description of the experimental apparatus is given. Additional experimental details and procedures can be found in Appendix A. Appendix B contain tables of molecular vibrational levels, rotational constants, and Franck-Condon Factors. The remaining appendices contain the source code of computer programs that have been developed for lab use.

Chapter 3 describes part of a project to measure and analyze the $2\,(0_g^+)$ state of Rb_2 in conjunction with Michael Bellos. The initial measurement was described in Ref. [37] and in his thesis [38]. This chapter analyzes the coupling of two particular levels of different electronic states, and a greatly enhanced formation rate of deeply bound $a\,^3\Sigma_u^+$ state molecules [36].

Chapter 4 describes our model for explaining short-range photoassociation, which our group first observed in Ref. [39]. We carried out an experiment to demonstrate and test this model, and provide data to clarify it.

Next is a high-resolution scan of selected vibrational levels of the lowest-energy example of a new type of long-range Rydberg molecule, in Chapter 5.

First described in Ref. [40], our study of low-n versions (n = 7, 9 – 12) of a long-range Rydberg molecule was limited by the linewidth of our pulsed dye laser. This work provides more spectroscopic details of this unusual molecular state.

Chapter 2

Experimental Setup

2.1 Magneto-Optical Trap (MOT)

As discussed in Section 1.1.1, the basis for all of our work is a magneto-optical trap (MOT). The original mechanical drawings of the MOT chamber are available in Appendix C of Ye Huang's dissertation [34]. A home-built zinc selenide (ZnSe) window transparent to 10.6 μm light from a CO_2 laser, based on the design of Ref. [41], was installed to replace a commercial window. The failure of that commercial window led to a plasma discharge, which in turn led to several design changes discussed in Section 2.3.

2.1.1 Rubidium Source

There are multiple options for a source of alkali atoms in an ultra-high vacuum (UHV) chamber. The simplest is to use an ampoule of Rb behind a valve to let Rb vapor into the apparatus. Another option is to use light-induced atomic desorption (LIAD). In LIAD, a significant amount of metallic Rb is adsorbed on a specialized coating on the chamber walls, and is released by a light or laser pulse, as in Ref. [42]. We have chosen to use SAES getters, which release nearly pure rubidium when heated by a few amperes of electric current. The benefit of these is that they release a well-controlled amount of Rb on demand. After turning off

the current, our UHV chamber returns to unmeasurably low pressure (less than the 1×10^{-10} torr lower limit of our ion pump readout) in under half an hour. In our system, we have an eight-pin feedthrough with one pin as a common, four devoted to Rb getters, and three containing K getters for future experiments. The Rb getter pins each have two getters tack welded in series to enhance the Rb flux and increase time between opening the chamber to replace them. Getters are stable for long periods in UHV, and are even resistant to atmosphere during chamber openings so long as the getter has not yet been activated. Once a getter is activated it cannot be exposed to atmosphere; atmospheric exposure renders them useless by oxidizing the exposed alkali.

Upon first activating a getter, a significant amount of contaminants will be released. This necessitates a careful "degassing" procedure when activating new getters. We have successfully used two methods of degassing. The first, described in Ref. [43], involves slowly turning up the current to a maximum of 5 – 5.5 A and leaving it there for $\geq$ 5 hours, ensuring that the pressure does not rise by more than an order of magnitude during the degassing. The second, described in Ref. [44], uses several 2 – 5 s pulses of 8 A. In both cases, the getters can then be run without fear of contamination with an initial current of $\sim$ 2.5 A. As the getter ages and its Rb is used up, the current required to maintain a particular background pressure will increase up to $\sim$ 5.5 A, at which point no useable Rb will remain.

2.1.2 MOT Lasers

In our system, we use two master lasers and a slave laser. The master lasers are Littrow-type external cavity diode lasers (ECDLs) originally using Hitachi

9 mm 50 mW diodes (part number HL7852G), and now using Thorlabs model L785P090 90 mW 5.6 mm diodes. Each master laser is locked to a saturated absorption Rb cell using home-built electronics [45]. The "trap" master laser is locked to the ^{85}Rb $\left|5s_{1/2}, F = 3\right\rangle \rightarrow \left|5p_{3/2}, F = 4\right\rangle$ transition, which is the MOT cycling transition used for trapping. The "repump" ECDL is locked to the $\left|5s_{1/2}, F = 2\right\rangle \rightarrow \left|5p_{3/2}, F = 3\right\rangle$ transition. Atoms in the $\left|5s_{1/2}, F = 2\right\rangle$ state are "dark" to the trap laser and are therefore untrapped. The laser tuned to this resonance returns them to the upper hyperfine "bright" state that is trapped, hence the name "repump". For stability reasons, the repump laser is actually locked to the highest-energy (F =2,3) crossover resonance (currently leftmost as seen on the oscilloscope), and the wavelength corrected by 31.7 MHz by acousto-optic modulator (AOM) detunings as detailed in Table 2.1 below. It should be noted that the locking scheme can easily be modified to trap ^{87}Rb as well. The trap laser will simply be locked to the equivalent ^{87}Rb transition $\left(\left|5s_{1/2}, F = 2\right\rangle \rightarrow \left|5p_{3/2}, F = 3\right\rangle\right)$; the repump will be locked to its corresponding transition $\left(\left|5s_{1/2}, F = 1\right\rangle \rightarrow \left|5p_{3/2}, F = 2\right\rangle\right)$ and have the AOM detuning changed to correct the crossover offset of 78.5 MHz. If the necessary offsets cannot be achieved, the existing AOM can be run in a double-pass configuration and the ^{87}Rb repump can be locked to the true spectroscopic transition directly.

After the power loss due to the cavity, plus pickoffs for the saturated absorption lock, there is insufficient power in the trap laser to achieve optimal MOT conditions. To increase the available power, we use ≤ 1 mW of trap laser power to injection-lock a slave diode laser. Using > 1 mW of injected power risks burning out the slave diode laser, which can happen with only brief exposure to these powers. The remainder of the trap master laser beam is used for absorption imag-

ing. The 1 mW beam is injected through the side of the output polarizing beam cube of the slave laser's Faraday isolator, with a half-wave plate providing the proper polarization for reverse propagation. The slave laser uses a Sanyo model DL7140-201S 70 mW diode (for future replacements, this diode has been replaced by ThorLabs by part no. L785P090, a 90 mW diode, which we also use for the ECDL master lasers). Injection locking is achieved through temperature and current tuning, and has multiple current values that will work. Our present diode locks at $\sim$ 120 mA and provides adequate power. The locking is observed by a camera that monitors the first-order diffraction of a pickoff of the output beam.

2.1.3 Acousto-Optic Modulators (AOMs)

Many acousto-optic modulators (AOMs) are used on the MOT optics table for frequency control and for switching applications. The MOT trap and repump beams, for example, are switched off during ionizing laser pulses to reduce the production of background atomic ions. A full list of these modulators, their frequencies, and their net frequency effects is given in Table 2.1. Each saturated absorption lock uses one AOM. The trap AOM is double-passed, and the repump AOM is single-passed. These AOMs, when used within a saturated absorption setup, cause a shift to the locking frequency of the laser output of $-\frac{1}{2}$ times the total shift due to the AOM.

The repump laser has one additional AOM that acts as a switch, sending the first-order beam to a fiber coupler. The trap laser has a double-passed AOM in the injection beam path. This double-pass can be used to shift the frequency of the slave laser without misaligning the injection beam, which allows transient cooling for optical trap loading. A description of the alignment procedure for this double-

AOM	Freq. (MHz)	# of Passes	Order	Shift (MHz)
Repump Saturation	76.6	1	+1	−38.3
Repump Switch	70	1	+1	+70
Trap Saturation	70	2	−1	+70
Trap Injection	62/ 90	2	−1	−124/ − 180
Slave Switch	40	1	+1	+40
Probe Switch	70	1	−1	−70

Table 2.1: A list of characteristics of the AOMs used on the MOT optics table. The Probe beam is the on-resonance probe laser used for absorption imaging. The rightmost column, "Shift", describes the total frequency shift imparted to the laser beam after all passes through the AOM.

pass AOM is in Appendix A.2, and the procedure for properly injection-locking the slave laser is in Appendix A.4. The remaining master trap beam passes through a switch AOM and to a fiber for absorption imaging. The slave laser output also passes through a switch AOM, the output of which is fiber coupled.

2.1.4 Fiber Coupling

Every beam used for the MOT, and nearly every beam originating from the MOT optics table, is fiber-coupled to the lower table using polarization-maintaining (PM) single-mode FC-APC fiber. The main advantages of fiber coupling are pointing stability and the isolation of downstream optics from upstream changes. The main disadvantage is power loss, and an occasionally important drawback is polarization rotation for imperfect input polarizations.

Low power is avoided as a problem through the use of a slave trap laser and through high-efficiency "switch" AOMs. The trap switch is over 80% efficient. This gives a fiber output power of 27 – 30 mW for the trap laser and 3 – 4 mW for the repump.

Polarization sensitivity is primarily important for the trap laser. When the input laser polarization is not perfectly aligned to the PM fiber axis, the polarization can rotate randomly due to birefringence along the fiber length [46]. This impacts the MOT by changing the ratio of power in the three arms, as the beam is split by polarizing beam cubes. The observable symptom is a randomly varying MOT fluorescence level that swamps trap-loss photoassociation (PA) signals. To properly align the input polarization using a half-wave plate, a high-quality polarizer is placed on the output to minimize transmission, with the beam monitored by a power meter. When the fiber is mechanically jiggled by tongs (not by hand, as body heat causes slow and uncontrolled birefringence changes), the half-wave plate is adjusted in 0.25° – 0.5° increments to minimize fluctuations (note that the rotation stage is marked in 2° increments). Alignment errors of 0.25° can have noticeable effects on MOT stability. If the polarization has drifted from a prior correct alignment, the total angular shift should be 5° or less.

Interestingly, Ref. [46] states that a 1.8° misalignment should have a ~ 30 dB extinction ratio. We will often see fluctuations on the 5 – 10 percent scale when misaligned by less than 2° and noticeable drift with misalignments of 0.25°, as mentioned above, indicating worse performance. This may be due to a degraded PM fiber, or simply polarization of lesser initial purity than used in their example. It may also be due to nonlinear coupling between the two polarization modes in the fiber core.

The trap and repump beams follow different paths to the MOT chamber. The repump is sent along the horizontal arm only (including retroreflection). The trap beam is split initially by one polarizing beam splitter (PBS). The reflected beam is combined with the repump, and the transmitted beam is sent to the two

vertical X arms. The splitting ratio is controlled by a half-wave plate. The two X arms are also split by a PBS, with a half-wave plate controlling the split ratio.

2.1.5 MOT Characteristics

When well-optimized, the ^{85}Rb MOT has a slightly flat-topped density profile, but is still fairly well-described by Gaussian fitting functions (see Fig. 2.1 for an example fit). Using one- and two-dimensional fits to absorption imaging data, we can obtain our basic MOT parameters, also shown in Fig. 2.1. The MOT peak density should be roughly 7×10^{10} cm^{-3} to 1×10^{11} cm^{-3}. The atom number is controlled primarily by the getter current; I target 7×10^7 atoms, in a range from 5×10^7 to 1×10^8 atoms.

Although the precise power level is not extremely critical, the repump beam is nonetheless very important to the MOT density and number. We discovered that changing the repump beam radius can significantly affect the atom number; increasing the radius increased the capture volume and helped us achieve larger MOTs than the lab had previously.

2.1.6 Absorption Imaging

We gain information about the MOT characteristics through absorption imaging, as shown in Fig. 2.1. Our process was first described in Ref. [47]. Using a probe laser resonant with the rubidium trap transition, we create a negative image of the MOT showing the absorbed or scattered light. A second image is taken of the probe beam without atoms present, and a third "dark" frame is taken without the probe beam. The dark frame is subtracted from the image and probe frames, then the image is divided by the probe to give an absorption frame. Some smoothing

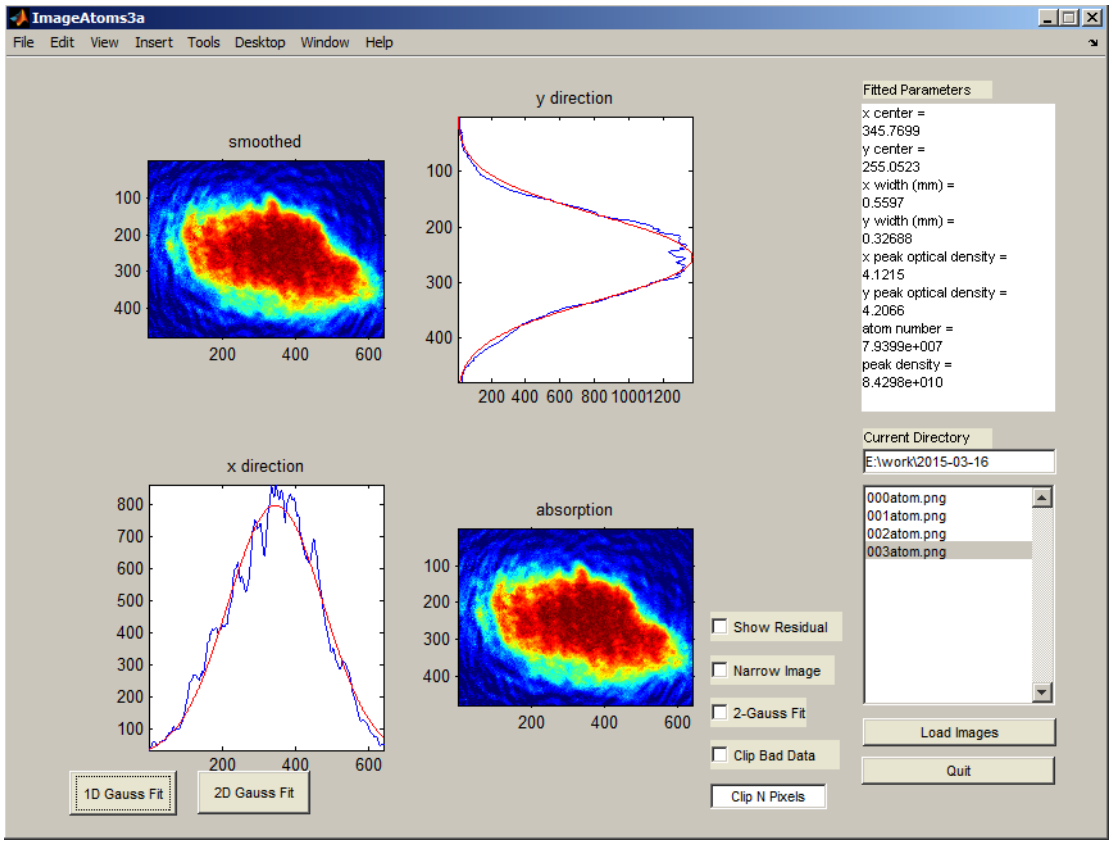

Fig. 2.1: This is the user interface of the ImageAtoms3a MATLAB program. It shows a fairly typical MOT, with 1-dimensional fits and MOT parameters displayed in the right-hand column. Note that standing-wave interference can be observed in the MOT density (e.g. in the 'absorption' plot).

is done, and each pixel is now has a value in the range [0,1]. We take $-ln(x_{ab})$ for each pixel x_{ab}, which gives the optical depth, and perform two more rounds of smoothing before continuing.

The MATLAB program "ImageAtoms3a", the code for which is in Appendix E, carries out the calculations to derive MOT parameters from these images. The MOT can be modeled as either a one-dimensional or two-dimensional Gaussian. The program can also model an overlapping dipole trap, also in one or

two dimensions. One- and two-dimensional Gaussian functions need good starting values for models to converge, so the program uses a multi-step process. To perform a one-dimensional fit, it first adds each row to create a y-axis profile, and each column for an x-axis profile. From these it calculates the center of mass of the MOT and the standard deviation of its density along the x and y axes. These are used as initial guesses in the one-dimensional nonlinear least-squares fit. A two-dimensional fit first calls the one-dimensional routine and uses its output for the two-dimensional initial guesses. In this manner the initial guesses are intelligently chosen, which aids in convergence.

If the box "2-Gauss Fit", which is intended to be used to fit an optical dipole trap overlapped with the MOT, is checked, a separate set of subroutines is called. For single-Gaussian fitting, all of the subroutine names end in a "3". Names of subroutines specific to two-Gaussian fitting end in "3a". The primary difference in these routines is that they use fitting functions containing a second Gaussian. The one-dimensional fit only fits the dipole trap in the y direction, as in the x direction both it and the MOT are essentially the same width and thus indistinguishable in a one-dimensional profile. The initial guess for the dipole trap width in y (found in Gaussian1D_3a, Appendix refmatlab:1D3a) is a fixed 1/15 of the MOT y width, which works well because this approximates the empirical ratio of the dipole trap to MOT widths in our apparatus. The initial guess (also in Gaussian1D_3a) for the dipole trap y position is 0.85$\times$ the MOT y position. While this typical value is appropriate for the beam alignment as it existed when the code was written, it may have to be altered by hand to achieve fit convergence.

An important use of absorption imaging is to calculate the MOT temperature. This can be done by taking images at various time delays after releasing the

MOT and fitting the x and y widths to determine the temperature. This fitting can be done with the "temp_fit3.m" MATLAB routine shown in Appendix E.10. This routine returns a temperature, confidence intervals, and a graph showing the fit so the user can visually confirm the fit quality.

2.2 Trap-Loss Spectroscopy

One of the earliest and most common detection methods for MOT-based ultracold photoassociation spectroscopy is trap-loss spectroscopy. In trap-loss spectroscopy, a photoassociation laser is directed at the MOT and scanned through one or more molecular transitions. Free MOT atoms are then converted to excited-state molecules, which quickly decay back to the ground state with time constants on the order of the atomic decay lifetime (26.2 ns [48]). When they decay, they can either remain bound ground-state molecules, or once again become a pair of free atoms. These new free atom pairs generally will carry more kinetic energy than they did before excitation, and some fraction will not be re-trapped by the MOT. Thus, through escape of free atoms and the non-resonance of molecules, the fluorescence of the MOT will decrease. If this fluorescence is plotted against photoassociation energy, a spectrum of dips will result – a trap-loss spectrum. An example trap-loss spectrum is provided in Fig. 2.2.

The MOT fluorescence is collected by a lens below the chamber and focused on a photodiode. The photodiode signal is amplified by a user-variable current-to-voltage converter before being sent on to be recorded.

The strength of trap-loss signals can vary from one molecular resonance to another. The short-range states we have studied do not produce any observable trap loss at all. In a typical long-range state, we see trap-loss of 2–10%. Smaller

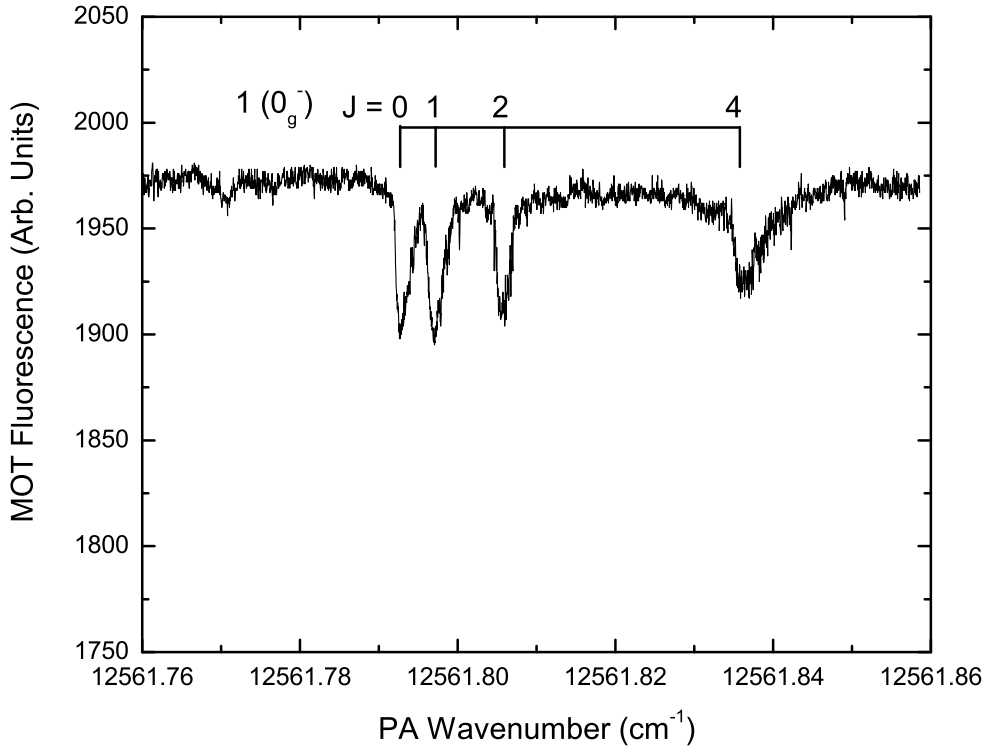

Fig. 2.2: A trap-loss spectrum showing the MOT fluorescence during a Ti:Sapphire PA laser scan. The PA resonance shown is $v' = 173$ of the $1\,(0_g^-)$ state below the $5p_{1/2}$ asymptote.

signals are difficult to detect due to fluctuations in the MOT fluorescence, and excellent MOT stability is required for trap-loss spectroscopy to be effective. The great advantage of the trap-loss technique is that it does not require any additional lasers or internal detectors to be added to the apparatus.

2.3 Ion Detection

Our primary means of data collection is through ion detection with time-of-flight mass spectroscopy, which allows us to distinguish between the desired molecular signal and background atomic signals, while also rejecting any other stray ions that may be present. The detection scheme is shown in schematic form in Fig. 2.3. Our ion detector is an ETP model 14150 discrete dynode multiplier, a photograph of which is shown in Fig. 2.4. An electric field plate opposite the detector is held at +1950 V, a grid between the MOT and detector is held at ~ -300 V, the detector's front grid is at -1950 V, and the detector back is grounded. This detector replaced a MCP (micro-channel plate) detector that failed in a plasma discharge incident. This is the incident briefly mentioned in Section 2.1.

Compared to the MCP, the discrete dynode multiplier offers both advantages and disadvantages. Advantages include improved shelf-life (as it is relatively impervious to atmospheric moisture), significantly higher physical robustness, greater dynamic range, and greater resistance to damage from large ion signals. A significant disadvantage is the design's sensitivity to external magnetic fields. The multiplier functions much as a photomultiplier does, with electrons cascading from dynode to dynode, with each separated by significant open space. If a magnetic field is present, the electrons will be deflected and miss the next dynode, disrupting the signal chain.

In our apparatus, the MOT anti-Helmholtz coils produce a magnetic field sufficient to disrupt the multiplier's function. To address this issue, the ETP detector is installed in a long arm of the vacuum chamber, reducing the magnetic field at its location. It is also surrounded by a custom-manufactured, annealed, grounded cylinder of mu-metal magnetic shielding (140 mm $\times$ 46 mm OD $\times$ 2

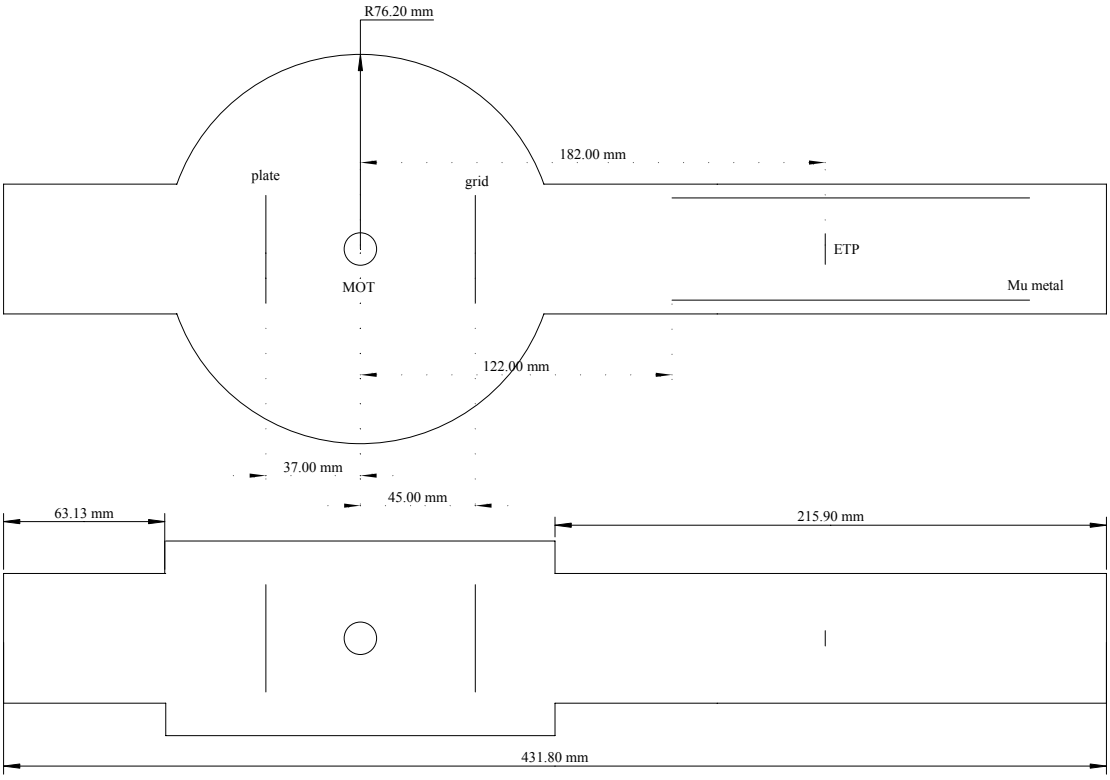

Fig. 2.3: This schematic drawing of the MOT chamber shows the MOT, the electric field plate and grid, the ETP discrete dynode multiplier, and the mu-metal shield. Except for the MOT, all sizes are to scale.

mm thickness), reducing the field below disruptive levels. The shield can be seen in Fig. 2.5. This shield shifts the magnetic field zero point where the MOT sits, so a compensating piece of mu-metal was placed opposite the chamber to re-center the field zero point (and hence the MOT position) to match the chamber center.

Another issue that developed with the new detector was the long free-flight region between the grid and the detector. Since the grid must be supported by a dielectric to maintain its electric potential, we used long Pyrex rods, with the wire to the grid passing through a hollow rod. During operation, stray ions

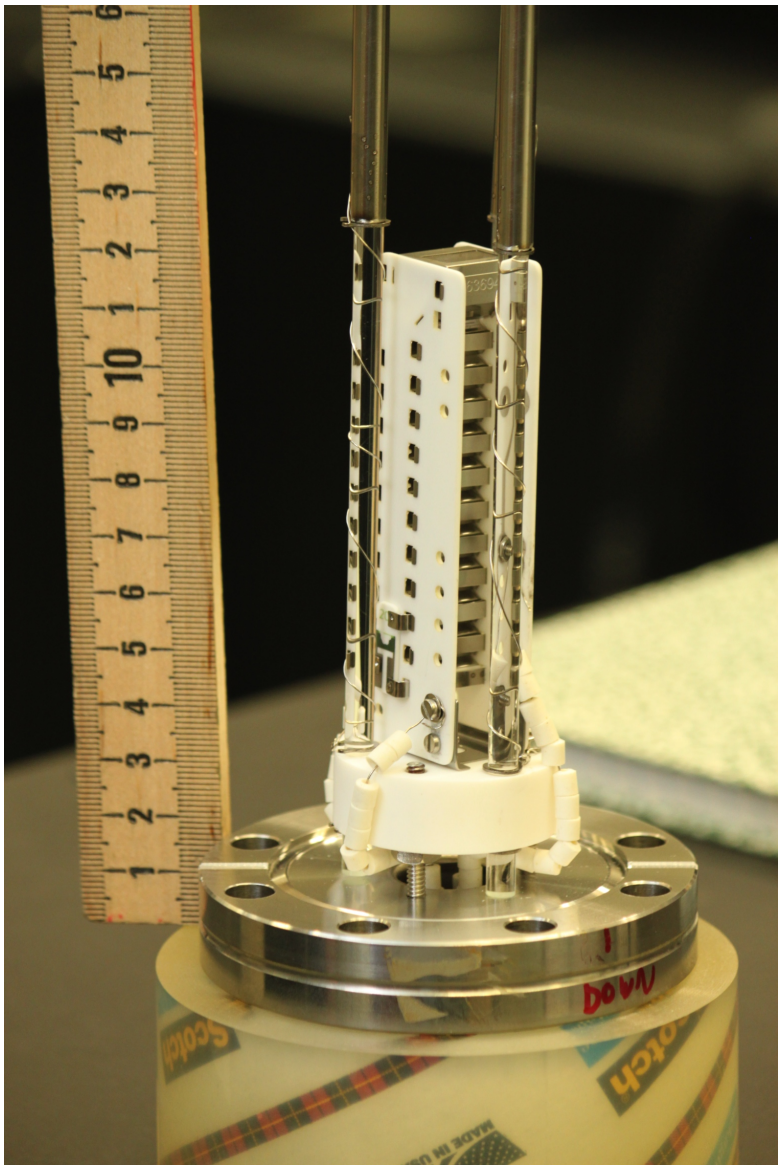

Fig. 2.4: A picture of the ETP model 14150 installed in its assembly. The Pyrex rods support the electric field grid that is a component of the ion optic system. The grounded metal sheaths around the rods prevent charge buildup.

impacted on these rods and charged them. The resulting electric field altered the ion focussing and eliminated our signal. Later simulations with SIMION showed that ion imaging was sensitive to even small (on the order of 10 V) charges on

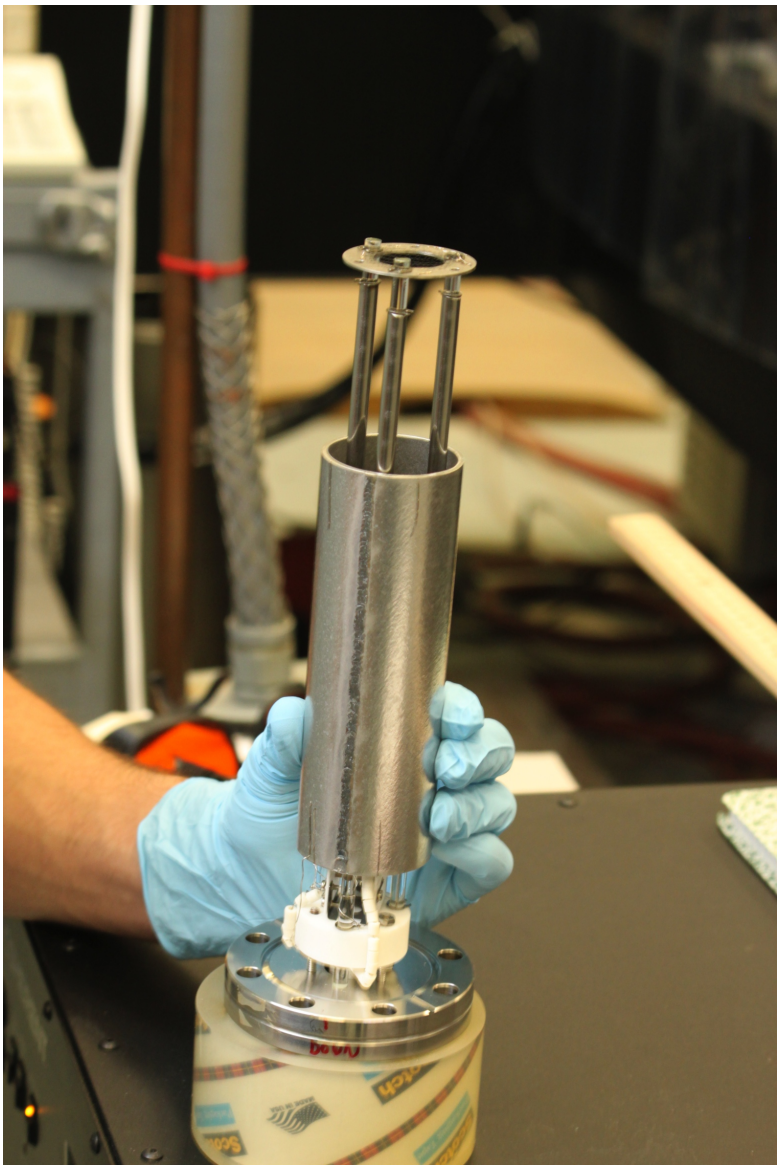

Fig. 2.5: A picture of the electron multiplier assembly with mu metal shielding in place, ready to be installed in the UHV chamber.

these rods. To correct this, we sheathed the Pyrex with grounded stainless steel tubes, held in place between the face of the detector and just before the grid. These tubes can be seen in Figs. 2.4 and 2.5. This solved the issue of the rods accumulating charge.

As a result of the chamber redesign for the discrete dynode multiplier, our time-of-flight discrimination has improved, and the region of space imaged on the detector has decreased. Both of these effects reduce noise and therefore lower the minimum level at which we can detect a molecular signal. An example time-of-flight signal is shown in Fig. 2.6.

To acquire a spectrum, the time-of-flight signal is sent to a boxcar integrator (SRS SR250). The molecular channel (or atomic or background channel, as desired) is integrated over a user-selectable gate (typical gate widths are $\sim 800 \pm 100$ ns) and optionally averaged using rolling exponential averaging over a set number of laser shots. After appropriate averaging (typically 10-shot averaging, as higher numbers require slower PA scans to avoid exponential tails on spectroscopic lines), signals as low as 0.05 ions/laser shot above the background can be distinguished, and signals of 0.2 ions/shot are extremely clear. In one spectrum, an average of three scans, the background has a short-term standard deviation of 0.019 ions/shot, consistent with 0.057 ions/shot signals being detectable by the 3σ standard.

An important characteristic of an ion detector is its "pulse height distribution" (PHD), or in our case a pulse *area* distribution. The PHD gives the range of pulse heights that can be the result of a single ion impacting the front of the detector, thus describing how well ions can be counted. The pulse height and pulse area can be related if most pulse shapes are close to the average pulse shape. For our model 14150 multiplier, a PHD has been published in Ref. [49]. For diagnostic purposes, and to enable calibration of data in ions per shot, we have measured our own pulse area distribution, shown in Fig. 2.7. This distribution matches the published distribution very accurately.

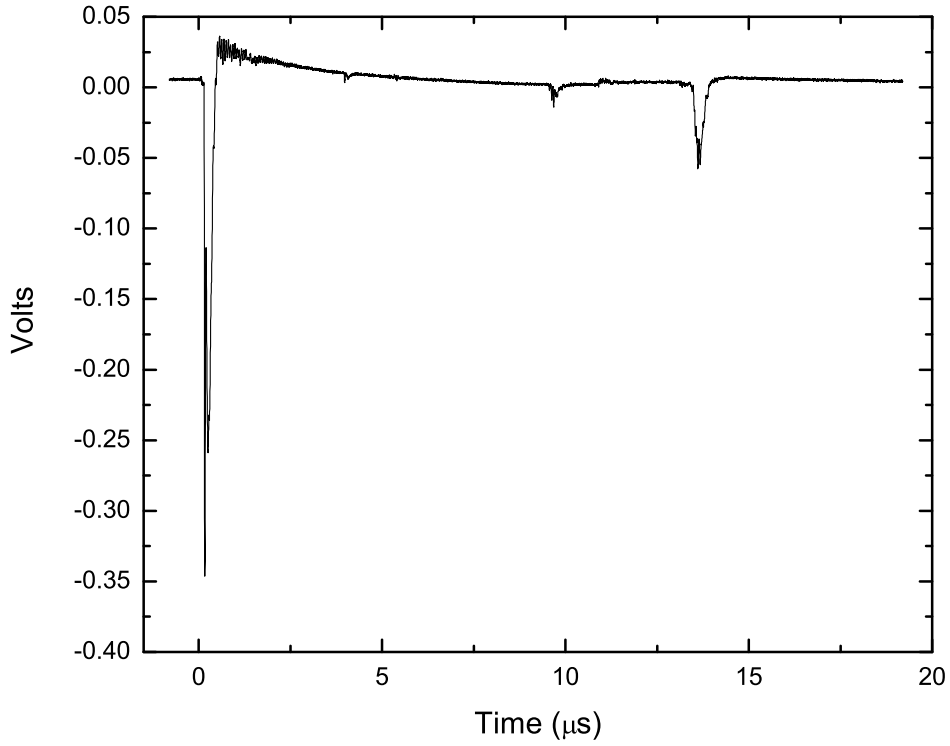

Fig. 2.6: A time-of-flight signal, captured by an oscilloscope on a $50\,\Omega$ impedance setting. Note that all signals are negative-going. The first peak is the "light peak" due to scattered ionizing photons hitting the detector. This acts as a zero-time indicator. Roughly 10 μs later is the strongly-suppressed atomic peak (the MOT is turned off during the light pulse to achieve this. At $\sim 14\,\mu$s, $\sqrt{2}$ times after the atomic peak, the molecular ion peak is visible. The $\sqrt{2}$ time-of-flight factor is due to a force that depends only on the single charge that both atomic and molecular ions possess, and the fact that our dimers have $2\times$ the mass of an atom. The small peak at $\sim 4\,\mu$s is a background ion.

2.4 Pulsed Amplifier

The newest addition to our experiment is a pulsed amplifier, originally built for use in the Rydberg project in Physics laboratory 301, as described in Ref. [50]. The

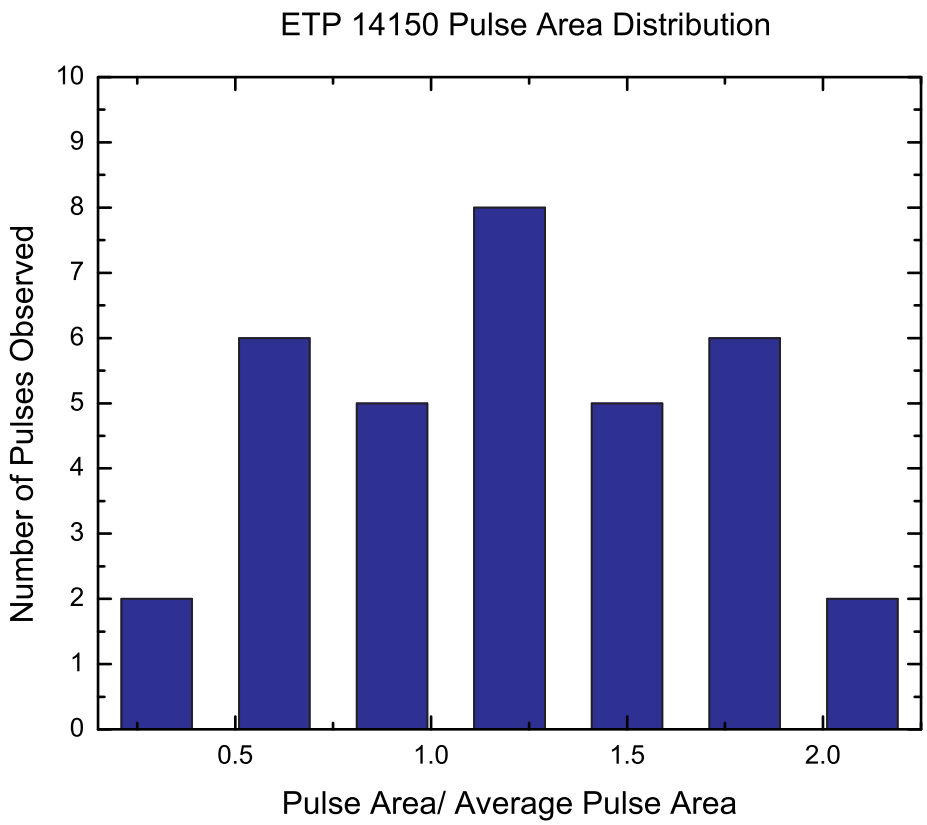

Fig. 2.7: The pulse area distribution for our ETP model 14150 discrete dynode multiplier. The horizontal axis is normalized to the average pulse area, measured in V·s into a 50 Ω impedance.

amplifier, a diagram of which is shown in Fig. 2.8, is composed of three Bethune dye cells pumped by an injection-seeded Nd:YAG laser and seeded by a Coherent 899-29 Ti:Sapphire laser via fiber coupling. A Bethune cell is a specially-designed dye amplifier cell that has much more uniform pumping than standard dye cells, and thus a more uniform beam profile suitable for doubling. It was first described in Ref. [51].

In our version of the amplifier, the first cell is relay imaged onto the second

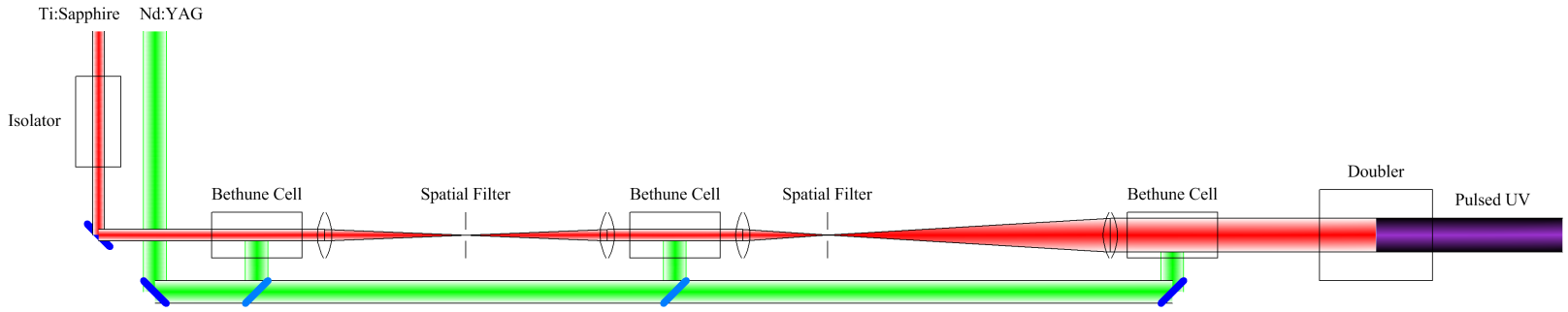

Fig. 2.8: A diagram of the pulsed amplifier. A Ti:Sapphire laser (Coherent 899-29) seeds the first of three Bethune dye cells. The first two have a 1 mm diameter, while the third has a 3 mm diameter. Due to the geometry of the internally reflecting cells, the dye capillary is evenly pumped from all directions.

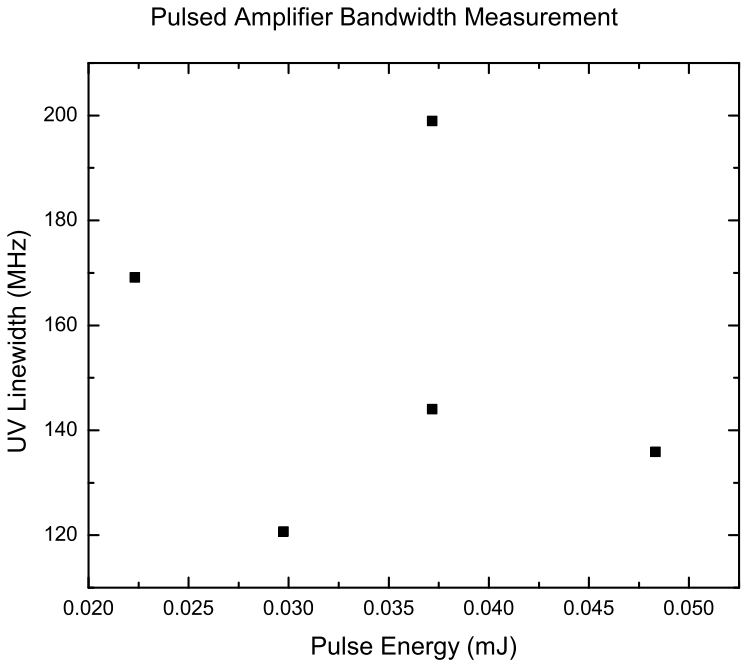

Fig. 2.9: This graph shows low-power measurements of the atomic $7p_{1/2}$ line to determine the UV laser linewidth after frequency-doubling the output of the pulsed amplifier.

by a $4f$ arrangement of 12.5 cm focal-length lenses with a spatial filter pinhole at the focus. As the third amplifier has a diameter 3× larger than the first and second, we use unequal lenses to approximately match the image to the new cell. The lenses have focal lengths of 7.5 cm and 25 cm, giving 3.3× magnification. Again, a pinhole is placed at the focus as a spatial filter. For our pulsed excitation experiment, we use LDS 750 dye in the amplifier chain. Using a stock solution of 0.44 g per liter (typically mixed in a 250 ml batch), we have experimentally determined that a mixture of 100 ml of stock solution with 200 ml of methanol works well in the first two cells. The third cell uses 25 ml of stock solution and 225 ml of methanol, diluting the concentration by a factor of 10.

These concentrations were determined by cuvette measurements of the absorption length for low-concentration dye probed by the Verdi at low power (the Verdi is a 532 nm continuous-wave doubled Nd:YVO4 (vandate) laser, which is a quite similar gain medium to Nd:YAG, and hence a nearly-identical wavelength to the pulsed Nd:YAG pump laser). It should be noted that LDS 750 has relatively poor solubility in methanol, and mixing a stock solution requires several hours on a magnetic stirrer.

The LDS 750 dye lifetime is notably less than Rhodamine dyes. At typical pump energies of ~ 65 mJ, the dye lasts for approximately two months of full-time use before replacement is required.

An important component of producing a narrow-linewidth pulse is using an injection-seed Nd:YAG pump laser. Without injection seeding, the laser develops large, complex sidebands that make spectra unusable. The pump power has also tended to be erratic when the injection seeder is not functioning. When the amplifier chain is working as intended, we measure a linewidth of ≤ 150 MHz, as seen in Fig. 2.9. This linewidth was measured by scanning through the $7p_{1/2}$ atomic line at low pulse energy. This is necessary to remove the effects of power broadening that strongly impact atomic transition linewidths. The measured linewidth is a convolution of the natural atomic linewidth, laser linewidth, and power broadening, as Doppler broadening is negligible at our MOT temperature. Natural linewidth is also fairly insignificant here.

The amplifier chain also shows good doubling characteristics, and the pulse energy of the doubled beam is stable with a standard deviation of only 7.73% of the mean energy, as shown in Fig. 2.10.

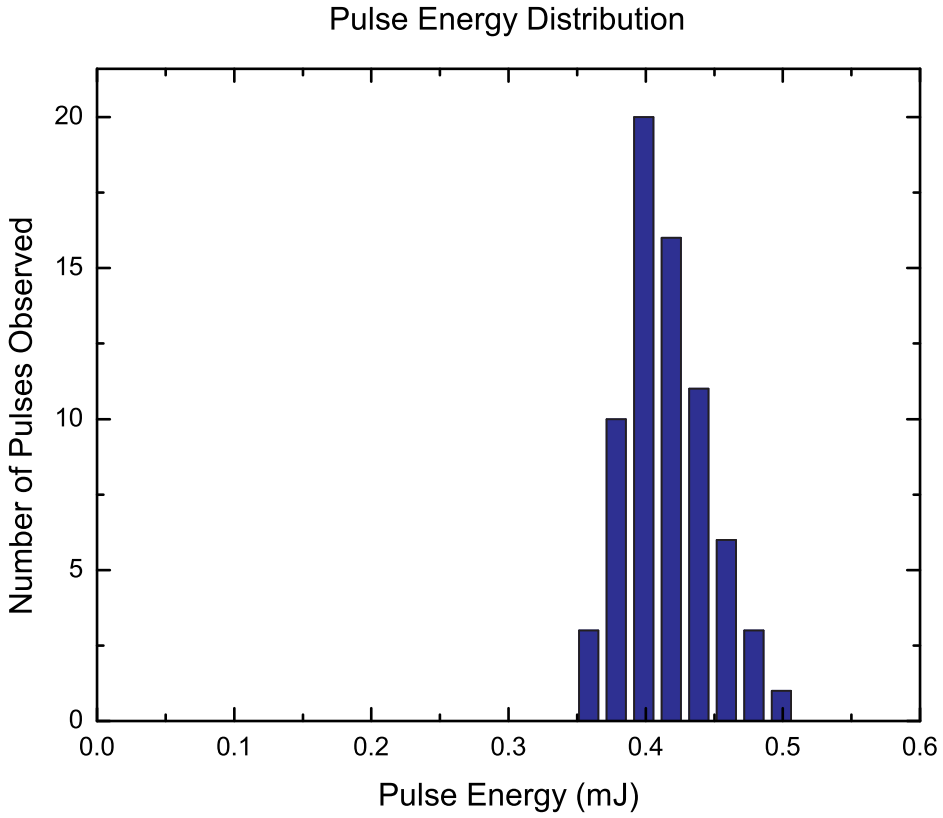

Fig. 2.10: This histogram shows the pulse energies of many UV pulses from the doubled pulsed amplifier. These data were taken with fresh dye, and the Spectr-Physics Quanta-Ray LAB-150 Nd:YAG flashlamps set to $\sim$ 8 on the (unitless) "Lamp Energy" control knob. The standard deviation of the distribution is 7.73% of the mean.

Chapter 3

Resonant Coupling of the $2\,(0_g^+)$ and $2\,(1_g)$ States [1]

3.1 Introduction

Ultracold molecules are currently a topic of much interest in the atomic and molecular physics community. When created through photoassociation (PA) of ultracold atoms, which is one of the simplest experimental techniques, these molecules can be used for high-resolution spectroscopy [19]. For many other applications, there is strong interest in controlling the final state of the molecule. In the case of alkali-metal dimers, levels of both the $X\,^1\Sigma_g^+$ and $a\,^3\Sigma_u^+$ states are stable enough for study. In either state, the vibrational and rotational levels populated are the primary variable that experimenters want to control. Several groups have had success in using PA to produce molecules in $v'' = 0$ of the $X\,^1\Sigma_{(g)}^+$ state in K_2 [52], Cs_2 [53], LiCs [54], NaCs [55], KRb [23], and RbCs [56,57]. Our own group has previously formed $^{85}Rb_2$ molecules in the lowest triplet $a\,^3\Sigma_u^+$ state with vibrational levels $v'' = 32 - 35$ [58] and $v'' = 0$ [39], and formation of $v'' = 0$ molecules was also previously reported in [9].

There is a significant body of literature regarding enhancement of PA via resonant coupling of a short-range molecular state with a long-range state, and

[1] This chapter is reproduced from Ref. [36] by permission, ©American Physical Society, 2013. There have been minor changes in wording and numbering, and an introductory section on resonant coupling, Section 3.4, and Fig. 3.5 have been added.

its use is becoming important in many experiments. Resonant coupling is experimentally useful because the long-range state enhances the PA rate, while the short-range state enhances decay to desirable (typically deeply-bound) levels. Our group has previously studied several such resonant couplings in $^{85}Rb_2$ [59] and $^{39}K^{85}Rb$ [23]. We have also discussed potential applications of these couplings and other predicted couplings in the creation of ground-state diatomic heteronuclear alkali molecules [60]. Other work using resonant coupling includes experiments on NaCs [61] and Cs_2 [62]. Here, we demonstrate a pathway to form molecules in $v'' = 18 - 24$ of the $a\,^3\Sigma_u^+$ state via a near-degenerate resonant coupling between levels of the Hund's case (c) $2\,(0_g^+)$ state at short range and the $2\,(1_g)$ state at long range. The $2\,(0_g^+)$ state correlates with the Hund's case (a) $2\,^1\Sigma_g^+$ state, while the $2\,(1_g)$ state correlates to the Hund's case (a) $1\,^1\Pi_g$ state.

3.2 Experiment

Our experimental apparatus has been described in detail in Ref. [37]. We begin by loading a magneto-optical trap (MOT) with 8×10^7 ^{85}Rb atoms at a peak density of 10^{11} cm^{-3} and a temperature of 120 μK. We then excite free-to-bound transitions to the $2\,(0_g^+)$ state converging to the $5s_{1/2} + 5p_{1/2}$ asymptote. The excited $2\,(0_g^+)$ rovibrational level rapidly decays radiatively to form metastable molecules in the $a\,^3\Sigma_u^+$ state, which are then ionized via $1+1$ resonance-enhanced multiphoton ionization (REMPI) through the $2\,^3\Sigma_g^+$ or $3\,^1\Sigma_g^+$ states and detected by a discrete dynode multiplier. Spectroscopy of these states was previously described in Refs. [34,58]. Molecular ions are discriminated from atomic ions and from scattered light by time-of-flight mass spectrometry.

As we showed in recent work [37], the $2\,(0_g^+)$ state supports quasibound

vibrational levels behind a barrier above the $5s + 5p_{1/2}$ limit. As also described in that work, the rotational distribution of these levels is affected by a ground-state $l = 4$ shape resonance that enhances the photoassociation rates to $J' = 3$ and $J' = 5$ relative to the rates for lower rotational levels, and well above the expected rates for a thermal distribution. Consistent with this, the $J' = 4$ level is not observed, as it is not enhanced by the shape resonance and must come entirely from the thermal sample. All of the levels that we have observed are below the $5s + 5p_{3/2}$ asymptote, where there are also many levels belonging to other electronic states that correlate to that asymptote. One such level of the $2\,(1_g)$ state, $v' = 155\,(\pm 1)$[2] (shown in Fig. 3.1), is nearly energetically degenerate with $v' = 111$ of the $2\,(0_g^+)$ state.

When molecules in the $2\,(0_g^+)$ state decay, they form metastable $a\,^3\Sigma_u^+$ molecules in vibrational levels $v'' = 18 - 24$. A section of a REMPI spectrum produced from the decay of $v' = 111$ and exhibiting the $a\,^3\Sigma_u^+$ vibrational level spacing is shown in Fig. 3.2. A similar spectrum showing molecules produced by the decay of $v' = 107$ is shown for comparison. While also strong, it has a noticeably reduced signal-to-noise ratio, indicating the $v' = 111$ level's usefulness in spectroscopic applications. Also shown is a REMPI spectrum obtained by photoassociating to a small satellite peak of the $v' = 111, J' = 5$ level. This is discussed in more detail in Section 3.5, where this same satellite peak is marked in the PA spectrum of Fig. 3.4(b). For a pure $\Omega = 0$ state such as the $2\,(0_g^+)$ state, there should be no significant hyperfine structure. Nonetheless, decay products of the satellite peak show nearly the same $a\,^3\Sigma_u^+$ state vibrational level distribution

[2] The vibrational numbering is somewhat uncertain, as it is based on *ab initio* potentials and no complete experimental assignment so far exists. We believe, however, that the assignment is good to within ± 1 of the actual vibrational quantum number.

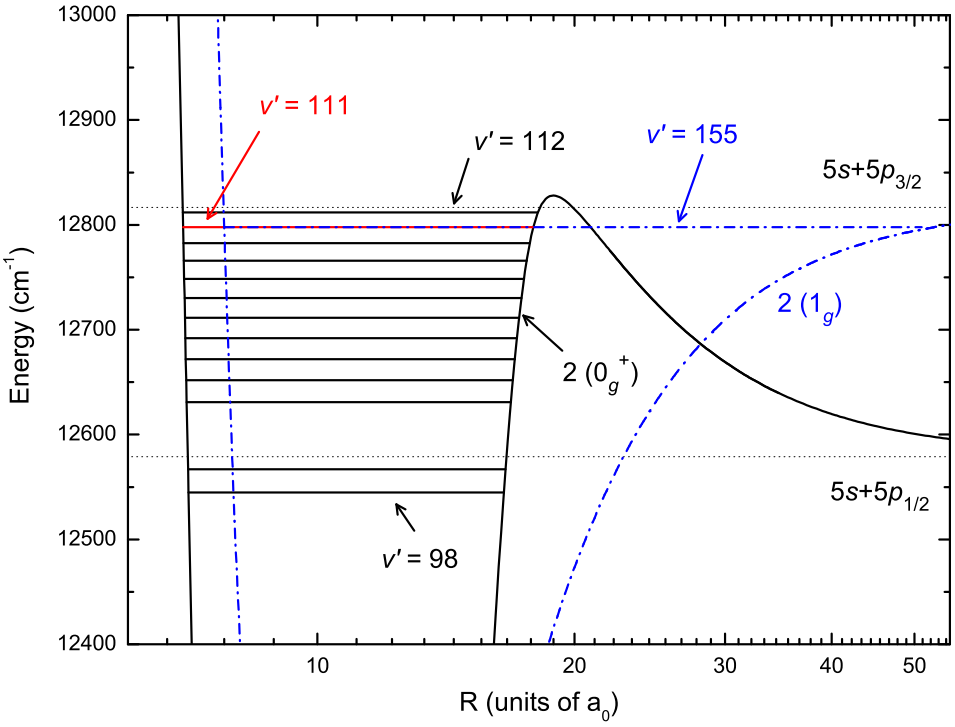

Fig. 3.1: Potential energy curves for the $2\,(0_g^+)$ and $2\,(1_g)$ states as calculated by [63]. The levels of the $2\,(0_g^+)$ state observed in [37] are shown, as is the $v' = 155$ level of the $2\,(1_g)$ state that is energetically near-degenerate with $v' = 111$. Tunneling effects are observed and discussed in [37].

as the $v' = 111$, $J' = 5$ level main peak, showing that they are closely related. This unexpected substructure around $v' = 111$, $J' = 5$ is one of several indications that the long-range $2\,(1_g)$ state is strongly coupled with the $2\,(0_g^+)$ state.

3.3 Molecule Production

A typical PA transition to a molecular level red-detuned from the $5s + 5p_{1/2}$ or $5s + 5p_{3/2}$ asymptote can create trap loss in the MOT of several percent, and

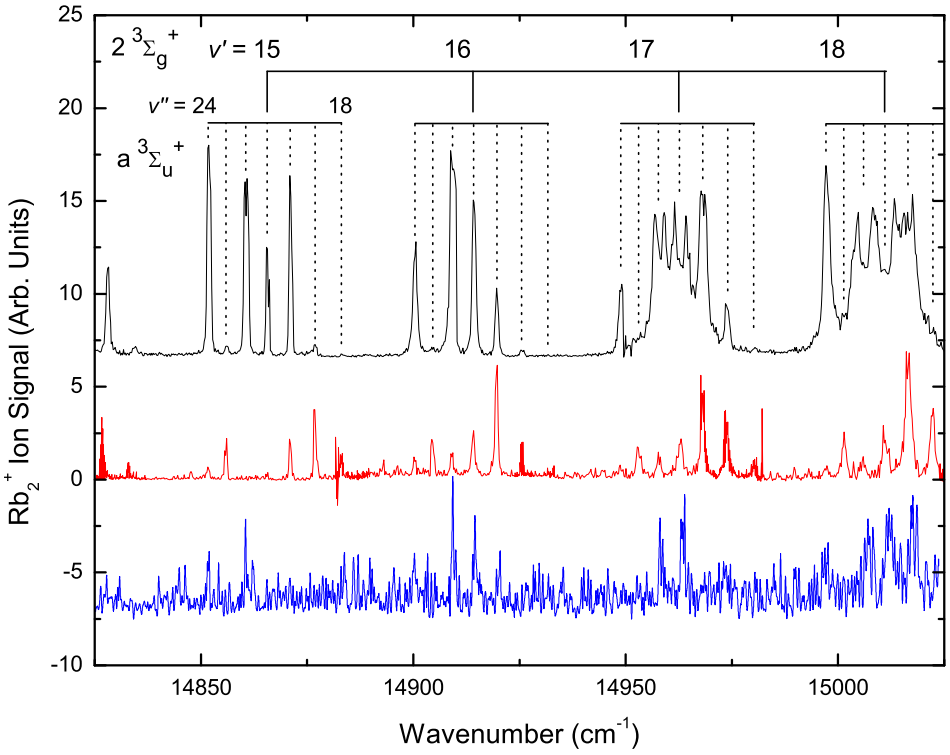

Fig. 3.2: Three REMPI spectra of the same region, using different PA levels to form the molecules. At top (black): a spectrum taken using PA to the resonantly coupled $v' = 111, J' = 5$ level of the $2\,(0_g^+)$ state. At center (red): a spectrum using a typical vibrational level, $v' = 107$, $J' = 3$, which is not resonantly coupled. At bottom (blue): the spectrum taken using a small satellite feature of the $v' = 111$, $J' = 5$ line, which is marked in Fig. 3.4(b). This spectrum is the average of three scans and is enlarged by a factor of 10 for visibility. We believe that this satellite feature represents a level of coupled $2\,(0_g^+)$ and $2\,(1_g)$ character. Vibrational quantum numbers of the initial $a\,^3\Sigma_u^+$ and intermediate $2\,^3\Sigma_g^+$ states are assigned as indicated.

extremely strong PA lines can exceed 50% loss. By comparison, the blue-detuned PA reported in our previous work [39] and in the current experiment [37] has never produced observable trap loss signals. Here, the phrase "blue-detuned" PA

is used to denote PA to levels that are energetically above the atomic asymptote to which they correlate, and thus are quasibound. Other investigations of this spectral region by trap loss have also shown no evidence of blue-detuned PA [64]. Nevertheless, the strongest line in this work, $v' = 111, J' = 5$, yields REMPI signals of 275 ions per REMPI shot or more under favorable conditions. The peak of this transition is clipped and therefore this value is a lower bound on the actual rate. Modeling the clipped line as a pure Lorentzian gives an estimated lower bound for the ion production rate of ~ 540 ions per shot. An unclipped spectrum that has been scaled to match this peak value is shown in Fig. 3.3(b), where the line strength of the non-coupled lines ($J' = 0$–3) is seen to be comparable to the $v' = 110$ spectrum in Fig. 3.3(a). We believe this similarity should exist because the ratios of the lines that are not resonantly coupled are similar, indicating that PA is not strongly affected by other factors such as the $l = 4$ ground-state shape resonance, and that the resonant coupling affects only $J' = 5$.

Fig. 3.3: **(a)** The rotational spectrum of the $v' = 110$ level of the $2\,(0_g^+)$ state as seen in ion detection from the $a\,^3\Sigma_u^+$, $v' = 20$ level, a fairly typical example of a strong PA transition to the $2\,(0_g^+)$ state. **(b)** The spectrum of the $v' = 111$ level detected from the $a\,^3\Sigma_u^+$, $v' = 22$ level, showing the strongly-enhanced $J' = 5$ line. This spectrum has been scaled based on Lorentzian fitting of other spectra, which exhibited clipping. The resulting $J' = 3$ line strength is comparable to that of $v' = 110$ in panel (a). At the top of panel (b) is the MOT fluorescence trap loss spectrum of the long-range $2\,(1_g)$ state. High resolution REMPI and trap loss scans of these coupled states are shown in Figs. 3.4(b) and (a), respectively. In both panels, the lines marked with an asterisk (*) are hyperfine "ghosts" from the lower $F = 2$ ground-state hyperfine level of $^{85}Rb_2$.

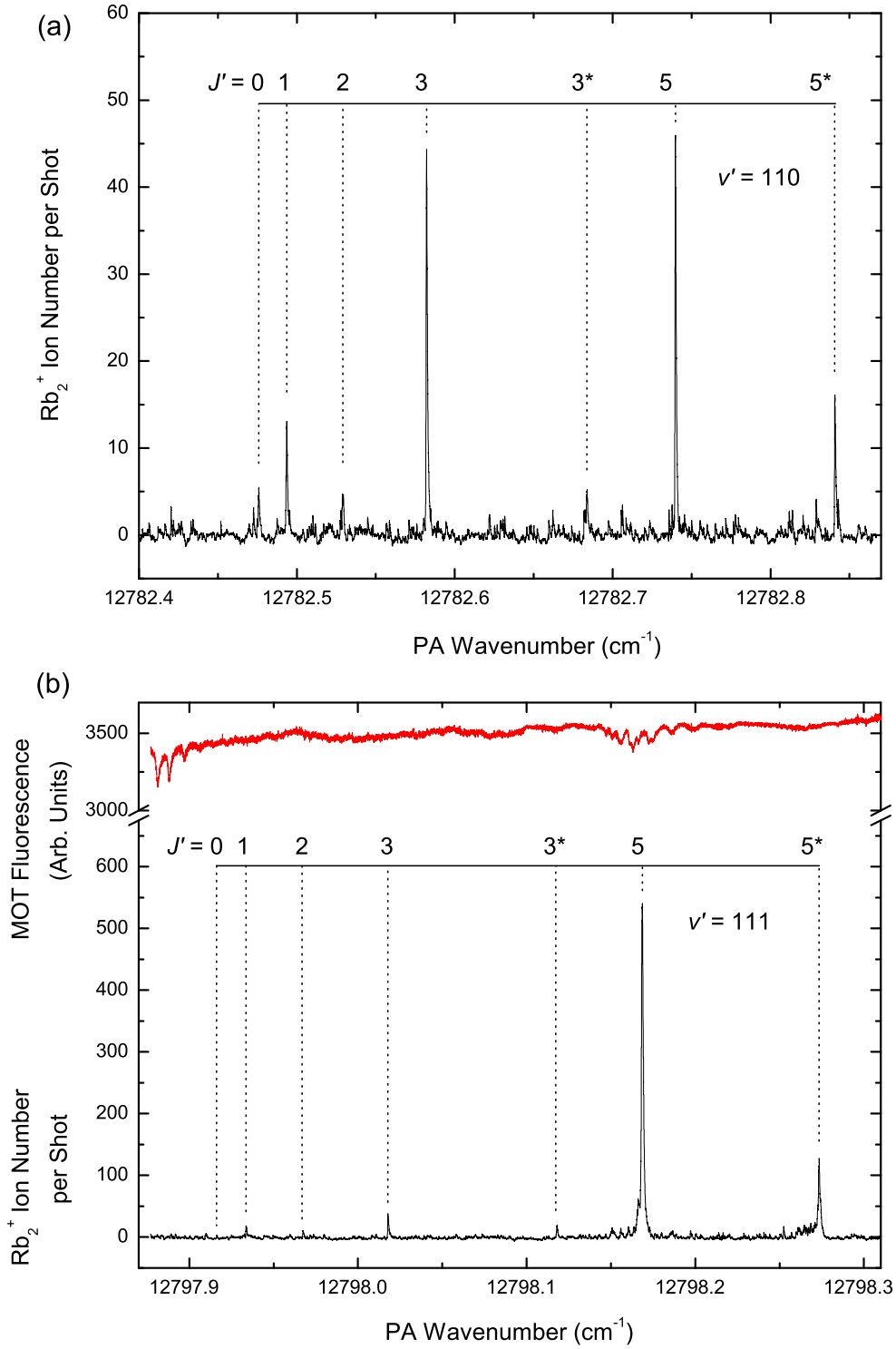
(a)
J′ = 0 1 2 3 3* 5 5*
v′ = 110
Rb2+ Ion Number per Shot
PA Wavenumber (cm-1)
(b)
J′ = 0 1 2 3 3* 5 5*
v′ = 111
MOT Fluorescence (Arb. Units)
Rb2+ Ion Number per Shot
PA Wavenumber (cm-1)

Using the simple method of Ref. [39], we can estimate the PA rate leading to this REMPI signal. The number of ions measured per REMPI pulse is:

$$N_{Rb_2^+} = N_a P_{\text{ionization}} e_{\text{d}} \ , \tag{3.1}$$

where e_{d} is the detector efficiency, $P_{\text{ionization}}$ is the probability of ionization by the REMPI pulse, and N_a is the number of molecules in the relevant vibrational level of the $a\,^3\Sigma_u^+$ state. For a conservative estimate of the PA rate, we will assume a detector efficiency of $e_{\text{d}} = 1$, although it may be somewhat less.

The ionization probability is given by:

$$\begin{aligned} P_{\text{ionization}} = 1 - e^{-Wt} &= 1 - e^{-\frac{\sigma F}{t} t} \\ &= 1 - e^{-\sigma E \lambda/(hc\pi r^2)} \ . \end{aligned} \tag{3.2}$$

Here $W = \frac{\sigma F}{t}$ is the transition rate determined by the photoionization cross section σ and the photon flux F per unit time. In turn, the flux is $F = E\lambda/(hc\pi r^2)$, where E is the pulse energy, λ is the pulsed laser wavelength, and r is the radius of the pulsed beam in the interaction region. The pulse is assumed to have constant intensity, as the laser beam profile is highly non-Gaussian. There is little published data on ionization cross sections in Rb_2, especially for two-photon processes. However, the cross section of the upper REMPI photoionization step is rate limiting, as the bound-to-bound initial step is likely saturated, so we will assume that ionization acts as a one-photon process. Using data from Ref. [65] and allowing for significant deviations due to the different ionization conditions, we will take $\sigma = 1^{+5}_{-0.5} \times 10^{-18}\,\text{cm}^{-2}$. This results in $P_{\text{ionization}} \cong 0.235$, with lower and upper bounds of 0.125 and 0.799. The remaining terms are experimental

parameters, with $\lambda \approx 655$ nm, $E = 5$ mJ, and $r = 1.4$ mm.

With these inputs, and using the modeled peak of $N_{Rb_2^+} = 540$, the population is $N_a \cong 2300$ molecules in the detected vibrational level, $v'' = 22$ of the $a\,^3\Sigma_u^+$ state, with a range of $\sim$ 675–4300 molecules. The PA rate can then be determined using

$$N_a(t) = \frac{R_{\rm PA} P_{\rm FCF} t}{(1 + t/\tau)} \ . \tag{3.3}$$

Here $R_{\rm PA}$ is the PA rate per atom, τ is the time molecules spend in the REMPI interaction region after formation, and $P_{\rm FCF}$ is the Franck-Condon Factor (FCF) that approximates the fraction decaying to an individual triplet level. In our system, cold molecules spend ≈ 5 ms in the REMPI region before their velocity and the acceleration of gravity carry them out. The FCF for decay to the $v'' = 22$ level is 4.36×10^{-2}, as calculated by LEVEL 8.0 [31] using the $a\,^3\Sigma_u^+$ potential from Ref. [29]. The estimated PA rate is thus 1.1×10^7 molecules per second, with a range between 3.1×10^6 and 2.0×10^7 s^{-1}.

An interesting comparison can be made between the PA rate calculated above from ion signals and the rate of PA at the same laser frequency implied by the observed trap loss signal. This trap loss, as seen in Figs. 3.3(b) and 3.4(a), is $\approx 2\%$ at the $2\,(0_g^+)$, $v' = 111$ position. The trap loss is $\approx 4\%$ at the largest peaks of the $2\,(1_g)$ state. For a MOT loaded in the presence of an extra loss mechanism, the relevant rate equation is

$$\frac{dN}{dt} = r_{\rm load} - (\gamma + r_{\rm PA})\, N, \tag{3.4}$$

where $\gamma = 1/\tau$, with τ specifying the MOT loading time without the PA beam, $r_{\rm load}$ is the loading rate of the MOT without PA, and $r_{\rm PA}$ is the loss rate due to

PA. In a steady state, the atom number $N_0 = r_{\rm load}/(\gamma + r_{\rm PA})$. The measured values of τ and N_0 are $\tau = 2 \pm 1$ s and $N_0 = 8 \times 10^7$ atoms. Assuming that the PA laser is scanned slowly enough that the steady state is always maintained, the PA rate per atom is

$$r_{\rm PA} = \gamma \left(\frac{N_0}{N} - 1 \right) \ . \tag{3.5}$$

Using the 2% value, this gives an estimated rate of $r_{\rm PA} = 1.0 \times 10^{-2}$ s^{-1} per atom, with lower and upper bounds of 6.8×10^{-3} and 2.0×10^{-2} s^{-1} per atom, respectively. The total PA rate is 4.1×10^5 molecules per second, with bounds of 2.7×10^5 and 8.2×10^5 s^{-1}.

It should be noted that some trap loss is due to molecules decaying to free atoms, and if some of these are recaptured by the MOT we will underestimate the true PA rate. The fraction of $2\,(0_g^+)$, $v' = 111$ molecules that decay to free atoms is 70%, which could cause the PA rate to be higher by up to a factor of 3. If we use the high estimate for $P_{\rm ionization}$, the resulting 3.1×10^6 molecules per second estimated from the ion counting rate is in only slight disagreement with the estimate based on trap loss and possible recapture.

This in turn is consistent with very strong coupling of the long-range $2\,(1_g)$, $v' = 155$ level and the short-range $2\,(0_g^+), v' = 111, J' = 5$ level. Since molecules formed at short range appear to account for nearly all photoassociated molecules, the wavefunction must be strongly mixed.

For further comparison, we can calculate the molecule formation rate for the $2\,(0_g^+), v' = 110, J' = 5$ level, which does not benefit from resonant coupling, using the same methods. In the spectrum of Fig. 3.3(a), the $a\,^3\Sigma_u^+, v'' = 20$ level is detected via REMPI while the photoassociation laser is scanned. It has a FCF of 6.60×10^{-2}, and a peak ion signal size of 46 ions per shot. This gives

a molecule production rate of 6.0×10^5 per second (with a range from 1.8×10^5 to 1.1×10^6), an order of magnitude less than the 1.1×10^7 molecules per second from the coupled level.

3.4 Resonant Coupling

Resonant coupling is a fairly common phenomenon in molecular spectroscopy, and one that opens areas of study that would otherwise be impossible, *e.g.* due to selection rules or poor Franck-Condon factors. It was recognized as causing perturbations in the Rb_2 $A \sim b$ state complex in 1999 [66] and was used to enhance formation of bound ultracold Cs_2 molecules in 2001 [62]. Beside the present work, resonant coupling has been observed by our group in Rb_2 [59] and KRb [23]. Potential applications of it in each heteronuclear alkali dimer are also discussed in Ref. [60].

Resonant coupling is a mutual perturbation of two (or possibly more) bound ro-vibrational levels. The defining characteristic of this coupling is the existence of a shared wavefunction that exists in both potential wells, which will have an effect on rotational constants. Since there is a perturbation, there will also be a shift in the energy of the individual eigenstates. The Hamiltonian can be written for a two-level system as [27]

$$\mathbf{H} = \begin{pmatrix} E_1 & H_{12} \\ H_{21} & E_2 \end{pmatrix} = \begin{pmatrix} E_1 & 0 \\ 0 & E_2 \end{pmatrix} + \begin{pmatrix} 0 & H_{12} \\ H_{21} & 0 \end{pmatrix} = \mathbf{H_0} + \mathbf{H}_{coupling} \tag{3.6}$$

where $H_{12} = H_{21}^*$ is the interaction energy between the two levels

$$H_{12} = \langle \psi_1 | \mathbf{H} | \psi_2 \rangle \tag{3.7}$$

and E_1 and E_2 are the unperturbed levels. We find $|H_{12}| \approx 3.4 \times 10^{-3}$ cm^{-1} in Section 3.5. If we diagonalize $\mathbf{H}$, we find

$$\mathbf{H}' = \begin{pmatrix} E_+ & 0 \\ 0 & E_- \end{pmatrix} \tag{3.8}$$

with eigenvalues

$$E_\pm = \frac{E_1 + E_2}{2} \pm \frac{1}{2}\sqrt{4\left|H_{12}\right|^2 + \Delta_0^2} = \frac{E_1 + E_2}{2} \pm \frac{1}{2}\Delta \tag{3.9}$$

where $\Delta_0 = E_2 - E_1$ is the spacing between the unperturbed levels and $\Delta = \sqrt{4\left|H_{12}\right|^2 + \Delta_0^2}$ is the perturbed (and therefore measured) level spacing. Due to the perturbation, the levels shift by $\pm\frac{1}{2}(\Delta - \Delta_0) = \pm\frac{1}{2}\left(\sqrt{4\left|H_{12}\right|^2 + \Delta_0^2} - \Delta_0\right)$. The shifted levels can, of course, be written as a linear sum of the unperturbed eigenstates. With proper normalization, these new levels are

$$\psi_- = a\psi_1 - b\psi_2 \tag{3.10a}$$

$$\psi_+ = b\psi_1 + a\psi_2 \tag{3.10b}$$

where

$$a = \left(\frac{\sqrt{4\left|H_{12}\right|^2 + \Delta_0^2} + \Delta_0}{2\sqrt{4\left|H_{12}\right|^2 + \Delta_0^2}}\right)^{1/2} = \left(\frac{\Delta + \Delta_0}{2\Delta}\right)^{1/2} \tag{3.11a}$$

$$b = \left(\frac{\sqrt{4\left|H_{12}\right|^2 + \Delta_0^2} - \Delta_0}{2\sqrt{4\left|H_{12}\right|^2 + \Delta_0^2}} \right)^{1/2} = \left(\frac{\Delta - \Delta_0}{2\Delta} \right)^{1/2} \tag{3.11b}$$

If the coefficients a and b each approach $1/\sqrt{2}$, the levels are equally mixed. If $a \to 1$ and $b \to 0$, $\psi_- \to \psi_1$ and $\psi_+ \to \psi_2$, i.e. there is very little mixed character in the perturbed eigenstate.

Although no electromagnetic transition is taking place, there are nonetheless selection rules that restrict which states can couple, irrespective of how nearly-degenerate they may be. These selection rules were developed by Kronig in Ref. [67] (published in German) and are reprinted in Herzberg (pp. 284 ff.) [27]. The selection rules are:

1. Total angular momentum is conserved; $\Delta J = 0$.

2. Spin angular momentum is conserved; $\Delta S = 0$.

3. For Hund's case (a) and (b), $\Delta\Lambda = 0, \pm 1$; for case (c), $\Delta\Omega = 0, \pm 1$

4. Plane-reflection symmetry (+ or −) must be preserved: $+ \nleftrightarrow -$

5. Nuclear-inversion symmetry must be preserved: *gerade* $\nleftrightarrow$ *ungerade*

Rules 1, 4, and 5 are rigorous, while 3 is Hund's case-dependent. Rule 2 is similar to the $\Delta S = 0$ selection rule for radiative transitions, and becomes weaker with increasing spin-orbit coupling. $\Delta\Lambda = 0$ (or $\Delta\Omega = 0$) perturbations are called *homogeneous* and are generally stronger than $\Delta\Lambda = \pm 1$ ($\Delta\Omega = \pm 1$) *heterogeneous* perturbations. Additionally, while homogeneous perturbations are J-independent, heterogeneous perturbations scale linearly with J [26].

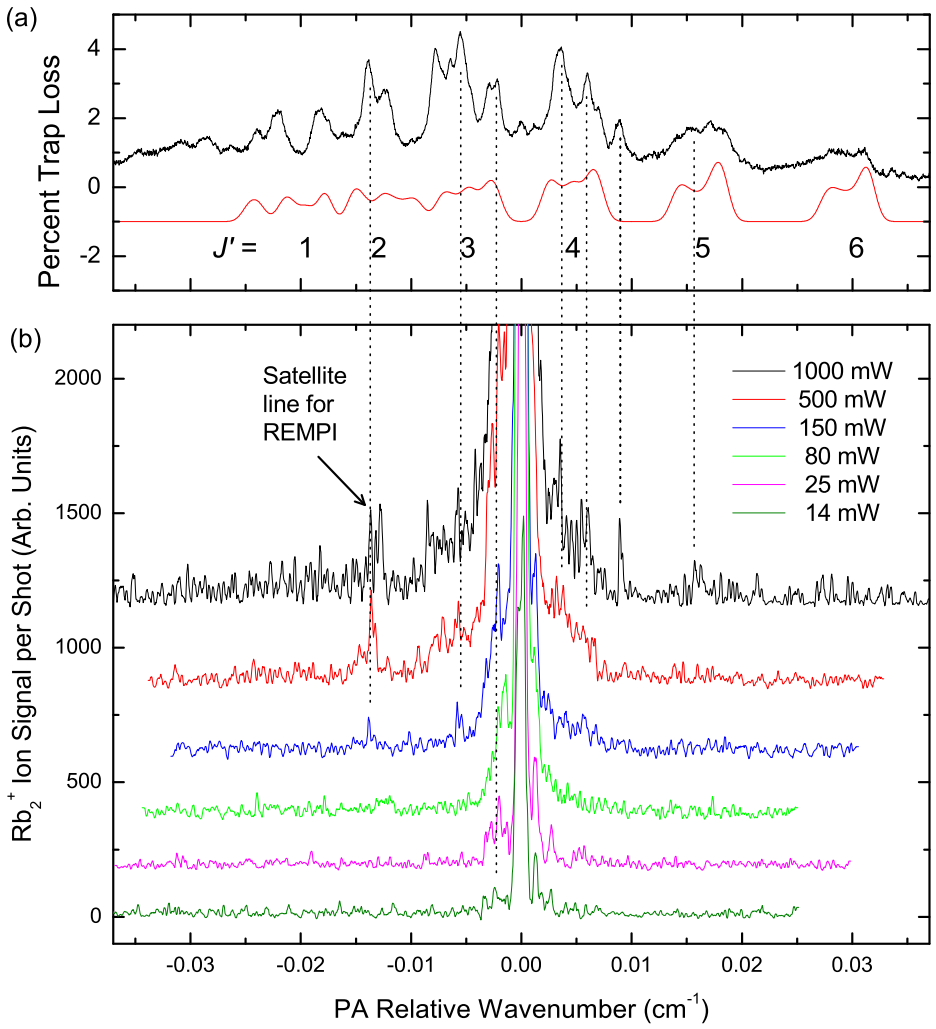

3.5 Hyperfine Structure and Coupling

To investigate the suspected hyperfine structure mentioned in Sec. 3.2, we undertook a series of high-resolution PA scans through the $J' = 5$ line. Each successive scan was done at a lower PA intensity, to better show features close to the central line. When aligned, as in Fig. 3.4(b), they show significant, consistent structure

Fig. 3.4: **(a)** Hyperfine structure in the PA spectrum of the $v' = 155$ level of the $2\,(1_g)$ state, averaged from six trap loss scans. The energy zero point (shown globally at figure bottom) is the position of the $v' = 111$, $J' = 5$ level of the $2\,(0_g^+)$ state. Below the data is a model fit using a hyperfine Hamiltonian from Ref. [68] and described in the text. The model is vertically offset from the experimental data, for clarity. **(b)** A series of scans at progressively lower PA intensities through the $v' = 111$, $J' = 5$ level of the $2\,(0_g^+)$ state. The scans are vertically offset and smoothed for clarity. To the left of the main peak is the satellite feature whose REMPI spectrum is shown in Fig. 3.2. Both panel (a) and panel (b) are on the same horizontal scale, and referenced to the position of the $2\,(0_g^+)$, $v' = 111$, $J' = 5$ level at 12798.17(3) cm^{-1}.

around the central rotational level. As indicated by dotted lines showing some of the strongest features, most of the satellite features correspond to trap loss of the $2\,(1_g)$ state shown in Fig. 3.4(a). This structure cannot be directly from decay products of the unperturbed $2\,(1_g)$ state, as the FCFs for decay of $v' = 155$ to the $a\,^3\Sigma_u^+$ state are non-vanishing ($> 1\%$) only for $v'' = 38$ and 39 ($v'' = 37$ has an FCF of $< 1 \times 10^{-4}$, and all other levels have FCFs $< 1 \times 10^{-8}$). These two levels have never been observed in REMPI in our apparatus, and are believed to be photodissociated quickly by the PA laser. In addition, the REMPI spectrum of the marked satellite feature (displayed in Fig. 3.2) clearly shows the level structure of deeply-bound $a\,^3\Sigma_u^+$ state molecules closely matching the spectrum of the strong central peak. Thus, as in the REMPI spectrum of the $J' = 5$ satellite feature in Fig. 3.2, this splitting appears to be rotational and hyperfine structure induced by coupling to the $v' = 155$ vibrational level of the $2\,(1_g)$ state. It is also worth noting that the signal-to-noise ratio (of PA spectroscopy with REMPI and ion detection) when using as little as 14 mW of PA power is still quite usable for spectroscopy, and is produced at a PA laser power far below the 500 mW to 1000

mW typically used in our experiment.

As discussed above, our trap loss scans of the $v' = 155$ level show significant rotational and hyperfine structure, though it is not well-resolved. We believe the linewidth is not a result of our scan speed, but is due to some combination of natural linewidth and broadening due to the high laser power needed to produce observable trap loss.

An averaged scan, compiled from six high-resolution scans using the code from Appendix D, is shown in Fig. 3.4(a). This spectrum is difficult to assign *a priori*, as the rotational and hyperfine level spacings overlap, particularly for low J levels. In order to gain insight into this structure, we model these data with a simulated spectrum using a Hamiltonian described in Ref. [68],

$$\begin{aligned}\mathcal{H} &= A_v \Omega i + \frac{\hbar^2 \vec{\ell}^2}{2\mu R^2} \\ &= A_v \left(i + \eta(i+3)^2\right) + \frac{\hbar^2}{2\mu R^2}\left(\vec{F} - \vec{J} - \vec{I}\right)^2 \ . \end{aligned} \tag{3.12}$$

This can be rewritten as

$$\begin{aligned}\mathcal{H} = A_v \left(i + \eta(i+3)^2\right) + B_v\big(&F(F+1) + 2 \\ &+ I(I+1) - 2\phi\Omega - F_+ I_- - F_- I_+ - 2\phi i + 2\Omega i\big)\end{aligned} \tag{3.13}$$

where A_v is the hyperfine coupling term, arising primarily from the $5\,^2S$ Fermi contact interaction, B_v is the rotational constant, i, ϕ, and Ω are the projections of $\vec{I}$, $\vec{F}$, and $\vec{J}$ on the internuclear axis, respectively, and η is a fitting constant for the term that is quadratic in i (this term is added to allow for variation in A_v with i). Using the parameters $A_v = 2.8 \times 10^{-6}$ cm^{-1}, $\eta = 8$, and $B_v = 0.00095$

cm^{-1}, the model qualitatively reproduces the observed spectrum, as is shown in Fig. 3.4(a). One minor issue with this fit is that it requires a rotational constant B_v that is smaller than the $B_v = 0.0012$ cm^{-1} calculated from our potentials. The calculated B_v values from other potentials have been relatively accurate, although they display a slight tendency to overestimate the B_v values compared to experiment [39,37]. The model also does not include weighting of the incoming partial waves, which are affected by the thermal population of the MOT as well as the $l = 4$ shape resonance. Note that we have tried to model neither the hyperfine structure of the $v' = 111$ level of the $2\,(0_g^+)$ state nor the coupling between the two hyperfine-split $J' = 5$ levels $\left(2\,(0_g^+) \sim 2\,(1_g)\right)$.

From the spectrum in Fig. 3.4(a), we measure the spacing between $v' = 111$, $J' = 5$ of the $2\,(0_g^+)$ state and $v' = 155$, $J' = 5$ of the $2\,(1_g)$ state to be $\Delta \approx 1.67 \times 10^{-2}$ cm^{-1}. We believe that levels other than $J' = 5$ of the $2\,(0_g^+)$ state do not contribute, as the other J levels are energetically much further away. If we know the unperturbed spacing of the levels and can measure a shift, we can estimate the strength of the coupling interaction via $\Delta = \sqrt{4|H_{12}|^2 + \Delta_0^2}$, where Δ_0 is the unperturbed spacing and $|H_{12}|$ is the interaction term of the Hamiltonian, as in Section 3.4.

By fitting the rotational progression of $v' = 111$, $J' = 5$, using a simple $E_J = B_v J(J+1)$ model both with and without the $J' = 5$ level, we find a shift of 7×10^{-4} cm^{-1}. This is within the 1.3×10^{-3} cm^{-1} FWHM linewidth, but can still help establish an estimate of the coupling strength. Assuming the shift is symmetric with the other coupling partner, we find $|H_{12}| \approx 3.4 \times 10^{-3}$ cm^{-1}, an extremely small value. The uncoupled wavefunctions of the $2\,(0_g^+)$ $v' = 111$ level and the $2\,(1_g)$ $v' = 155$ level are shown in Fig. 3.5 to illustrate their overlap. The

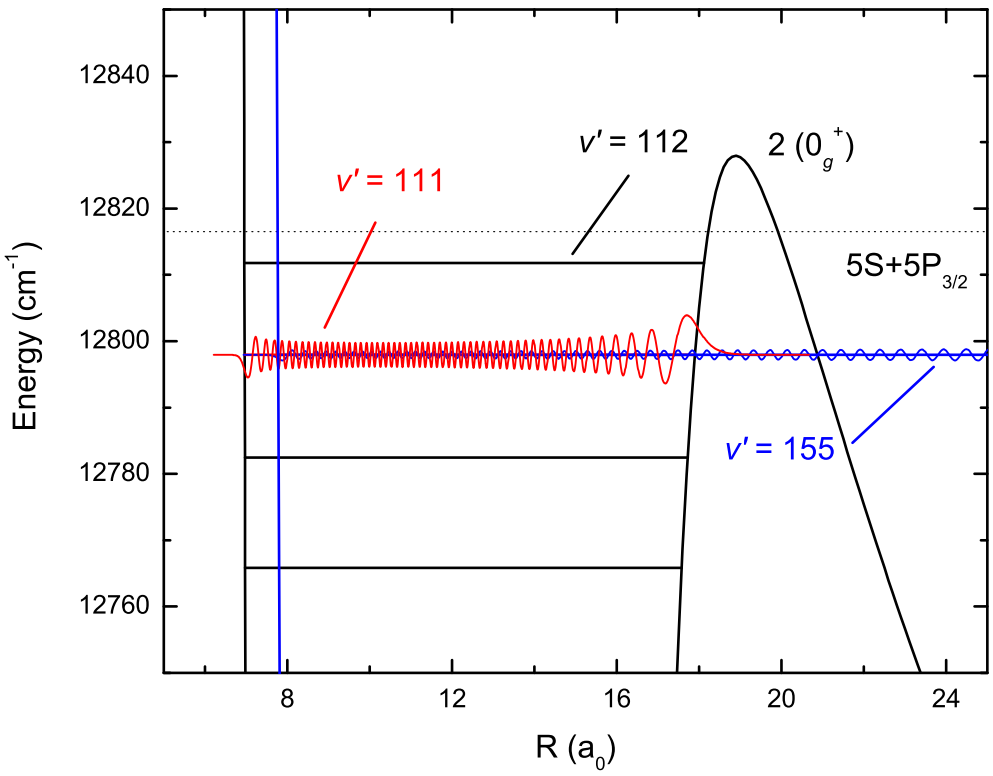

Fig. 3.5: A plot showing the overlap of the wavefunctions of the unperturbed $2\,(0_g^+)$ $v' = 111$ level (shown in red) and the $2\,(1_g)$ $v' = 155$ level (blue). The $2\,(1_g)$ $v' = 155$ wavefunction extends out to its outer turning point at ~ 53 a_0.

wavefunction of the $2\,(1_g)$ $v' = 155$ level extends to much longer range than the $2\,(0_g^+)$ $v' = 111$ wavefunction, with an outer turning point at ~ 53 a_0.

Since the two states that are involved in this coupling have $\Omega = 0$ and $\Omega = 1$, the coupling must be the result of an inhomogeneous perturbation. There are two primary causes of such perturbations—the non-Born-Oppenheimer S-uncoupling and the L-uncoupling operators [69]. The S-uncoupling operator has selection rules $\Delta S = 0$, $\Delta\Omega = \Delta\Sigma = \pm 1$, and $\Delta\Lambda = 0$. However, this operator only couples Ω components of the same electronic state multiplet. Additionally, our Hund's case (a) $2\,^1\Sigma_g^+$ and $1\,^1\Pi_g$ states have $\Lambda = 0$ and $\Lambda = 1$, respectively, rul-

ing out an S-uncoupling mediated perturbation. The L-uncoupling operator has selection rules $\Delta\Omega = \Delta\Lambda = \pm 1$ and $\Delta S = 0$. This operator, having the form $(1/2\mu R^2)\,(\mathbf{J}^+\mathbf{L}^- + \mathbf{J}^-\mathbf{L}^+)$, can couple different electronic states. The observed resonant coupling is thus likely the result of an L-uncoupling mediated perturbation.

3.6 Conclusion

We have shown that there is resonant coupling between a pair of $J' = 5$ levels in the $2\,^1\Sigma_g^+ \sim 2\,(0_g^+)$ and $1\,^1\Pi_g \sim 2\,(1_g)$ states. This coupling causes an order-of-magnitude increase in the production of $a\,^3\Sigma_u^+$ state molecules, compared with nearby vibrational levels of the $2\,^1\Sigma_g^+ \sim 2\,(0_g^+)$ state, and yields an approximate PA rate of 5.4×10^6 molecules per second. This coupling provides a strong pathway for creating deeply bound $a\,^3\Sigma_u^+$ state molecules. As it connects high-v levels of the $a\,^3\Sigma_u^+$ state (through the potential of the long-range component) with more deeply bound levels (through the potential of the short-range component), it can also provide an experimental pathway for molecular transfer between these levels.

Chapter 4

Short-Range Photoassociation

In recent work, our lab has performed a number of short-range photoassociation (PA) experiments. In Ref. [39] we perform photoassociation above the $5S + 5P_{3/2}$ asymptote of Rb_2, and in Refs. [37,36] we perform photoassociation above and below the $5S + 5P_{1/2}$ asymptote.

4.1 Traditional Photoassociation

When photoassociation is done in the traditional long-range regime, the $\Sigma_n \frac{C_n}{R^n}$ form of the potential is different in the ground and excited states . In the ground state, the long-range potential is due to London dispersion forces, and takes the form $U = -\frac{C_6}{R^6} - \frac{C_8}{R^8} - \frac{C_{10}}{R^{10}}$. These terms correspond to the dipole-dipole, dipole-quadrupole, and quadrupole-quadrupole plus dipole-octupole interactions. The excited state, in additional to C_6, C_8, and C_{10}, also contains a leading (positive or negative) $\frac{C_3}{R^3}$ term [70].

This difference in functional form means that increasing detuning from the excited atomic asymptote reduces photoassociation efficiency. In a 1997 paper [21], Pillet derives an expression (equation 55) for the photoassociation efficiency and finds that the efficiency is proportional to $\Delta^{-(4J'+7)/3}$, where Δ is the detuning below the atomic asymptote. This derivation assumes that PA can only occur

below the asymptote, and implies that it is only strong enough to be feasible near the atomic dissociation asymptote, both of which have been demonstrated to be untrue in our work (in Rb_2 [39,37]) and that of others (in LiCs [54], RbCs [71,72], and NaCs [61]).

This traditional view of photoassociation makes the assumption that the only viable place for PA is at long range. There are several reasons that this is done, including the number of atom pairs that exist at a given range in the MOT and the fact that the amplitude of the nuclear wavefunction is small at short range and much larger at long range. However, there is a significant maximum in the square of the wavefunction amplitude at the inner wall of the $a\,^3\Sigma_u^+$ potential in $^{85}Rb_2$, roughly at $9\,a_0$. As was discussed in Ref. [37], there is also a g-wave shape resonance in the triplet potential because of a centrifugal barrier near $\sim 80\,a_0$. The zero-energy wavefunction is similar in the $a\,^3\Sigma^+$ state of many other homo- and heteronuclear alkali dimers.

4.2 Photoassociation Model

As stated in Section 4.1, we now often operate under circumstances where traditional assumptions about photoassociation do not apply. We thus introduce a simple model to predict the efficiency of photoassociation in the short-range or blue-detuned regions that were formerly considered inaccessible. It turns out that the strategies this suggests can also be used to predict traditional photoassociation efficiency. Our model assumes that the inner turning point of the zero-energy free wavefunction, or incoming scattering state, creates a population of nearby atom pairs sufficient to form molecules at relatively short range. An example of short-range excitation to the $^{85}Rb_2\ 1\,^3\Pi_{g,\,\Omega=1}$ state is shown in Fig. 4.1

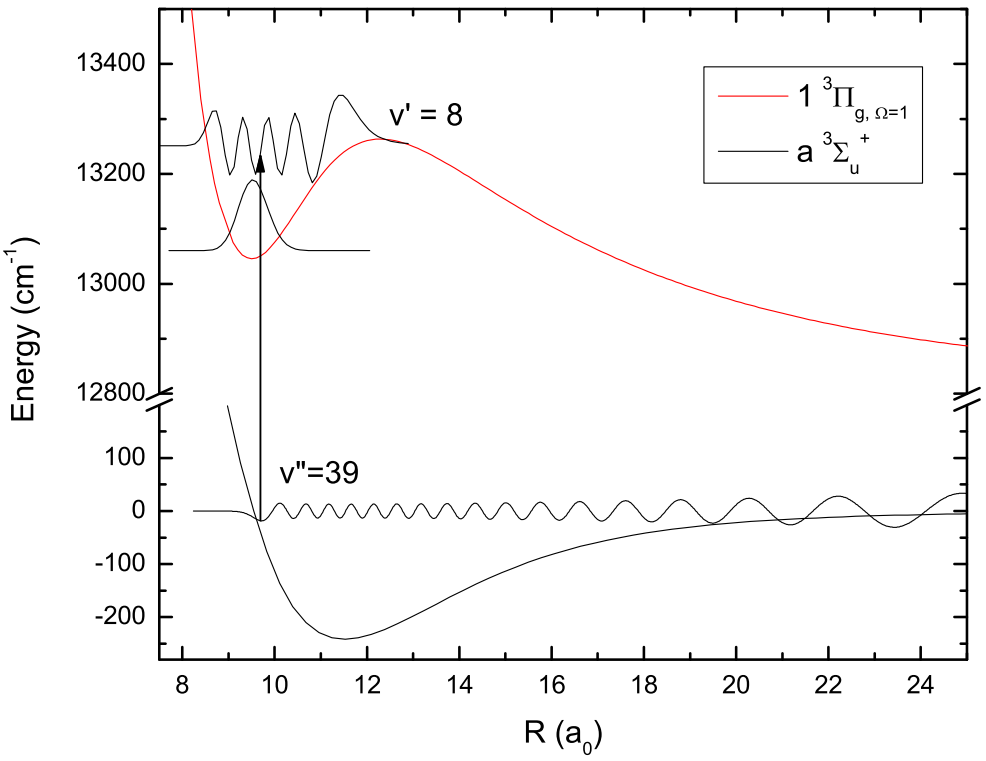

Fig. 4.1: Wavefunctions of the $a\,^3\Sigma_u^+$, $v'' = 39$ level and two levels of the $1\,^3\Pi_{g,\,\Omega=1}$ state, the $v' = 0$ and $v' = 8$ levels. The $v'' = 39$ wavefunction closely resembles a low-energy continuum wavefunction throughout the range of R shown here. A vertical transition is shown from the a state $v'' = 39$ to the $1\,^3\Pi_g$ $v' = 8$, illustrating their small but important overlap. The same arrow illustrates the much larger overlap between the a state with $v'' = 39$ and the $1\,^3\Pi_g$ state with $v' = 0$. It should be noted that the $v'' = 39$ wavefunction amplitude increases dramatically at longer range out to its maximum at ~ 62 a_0.

In a time-dependent view, this can be interpreted as meaning that atom pairs slow down slightly when they collide at short range, and until they fly apart again. This period of slow movement at short range means that there is always a non-negligible fraction of atoms available to interact at this internuclear distance.

Since the lowest triplet potential inner wall is at significantly longer range than the inner wall of the singlet state, colliding triplet pairs of atoms are able to access many states of interest that are inaccessible to colliding pairs of singlet character.

It is important to note that any PA transitions that are to be studied at short range must be accessible from the lowest triplet potential. In particular, this means that the transition must be allowed from the lowest triplet state in the appropriate Hund's case. For pairs of identical ground-state alkali atoms, this implies PA to a triplet *ungerade* state in case (a), or a 0_u^+, 0_u^-, or 1_u state in case (c). Although for heavy alkalis such as ^{85}Rb the singlet $\nleftrightarrow$ triplet selection rule is weakened (or equivalently, that case (a) quantum numbers are no longer perfectly "good", and that case (c) quantum numbers may be more appropriate), the $g \leftrightarrow u$ selection rule is still strong in a homonuclear system.

A simple way to use this model to calculate relative excitation probabilites from free triplet atoms to a given excited state is to calculate the FCF of the highest bound level of the lowest triplet state with all levels of the target excited state. It is slightly more accurate to calculate the square of the overlap integral from the true zero-energy (free) state, but many groups already use a bound $\rightarrow$ bound calculation program such as LEVEL 8.2 [32]. The highest bound vibrational level is nearly identical at short range to the zero-energy scattering state, due to the steepness of the repulsive wall and the similarity in their energies. At our temperature of $\sim 120\,\mu$K, the scattering state has a peak at 2.5 MHz, while the $v'' = 39$ level is bound by 0.007238 cm^{-1}, or 217 MHz, for a difference of less than ~ 220 MHz. I will show a comparison of such an FCF calculation to experimental data in Section 4.3.

As with any use of a Franck-Condon Factor, the R-dependence of the tran-

sition dipole moment may play an important role that is neglected by our approximation. The $2\,^1\Sigma_g^+ \sim 2\,(0_g^+)$ state studied in Refs. [37,36] is an excellent example. The case (c) transition dipole is constant and large at long range, but at short range (in the region of our experiment) drops rapidly toward zero. This caused a drop-off in our signal for shorter-range and more deeply-bound vibrational levels, and reflects a transition from the allowed transition in case (c) to a region where case (a) better represents the coupling and the transition is singlet $\leftrightarrow$ triplet forbidden.

The calculation of FCFs between the $v'' = 39$ level of the $a\,^3\Sigma_u^+$ state and the v' levels of the $1\,^3\Pi_{g,\,\Omega=1}$ state is based on the experimentally determined potential of the $a\,^3\Sigma_u^+$ state [29] and an *ab initio* potential calculated by Dulieu and Gerdes that reproduces the vibrational and rotational constants fairly accurately (see Table 1 of Ref. [39]). The electronic transition dipole moment is not expected to vary significantly in the region of overlap of ψ' and ψ''.

4.3 Comparison to Data

To test whether these FCFs can predict the relative efficiency of short-range PA to various levels, we looked at several lines that our group previously detected in Ref. [39]. The target state is the $\Omega = 1$ component of the $1\,^3\Pi_g$ manifold of $^{85}Rb_2$. This state is blue-detuned above the $5S + 5P_{3/2}$ asymptote.

Our experiment was carried out under conditions similar to the original work, and a detailed description can be found in Refs. [37,39]. The molecules were formed in a MOT of typically 8×10^7 atoms and a density of 1×10^{11} cm^{-3} at $\sim 120\,\mu$K. The excitation was performed with a fiber-coupled photoassociation laser (Coherent 899-29 Ti:Sapphire) delivering 650 mW to the experimental chamber.

After photoassociation, the molecules rapidly decay to deeply-bound levels of the $a\,^3\Sigma_u^+$ state and are detected via pulsed ionization. Ions are detected on a discrete-dynode multiplier (ETP model 14150) and spectra are acquired via a boxcar integrator on a gated time-of-flight signal.

To ensure accurate relative line height measurements, detection was done using photoionization with a pulsed 355 nm UV tripled Nd:YAG at 3.6 mJ/pulse. The photon energy corresponds to $\sim 28,169$ cm^{-1}. Based on the data we reported in Ref. [73], the bottom of the Rb_2^+ potential is no higher than 27,383.2 cm^{-1}. Accounting for the ~ 234.7 cm^{-1} binding energy of the $a\,^3\Sigma_u^+$, $v'' = 0$ level, up to 27,617.9 cm^{-1} could be necessary to ionize. Our UV photons are ~ 551 cm^{-1} above this, and thus all ionization should be single-photon and line strengths should be independent of any intermediate-state resonances. Measured line strengths should therefore reflect the true transition probabilities.

Each vibrational level was measured and the line height at $J' = 3$ recorded. As discussed in Section 4.2, FCFs were calculated for the same transitions by using the $a\,^3\Sigma_u^+$, $v'' = 39$ level as a proxy for the zero-energy scattering state. A comparison of these data and the FCF calculation is shown in Fig. 4.2. The experimental data are scaled to match the FCF calculations at $v' = 2$ to better show the quality of the comparison. It should be noted that lines with FCFs as low as 4.3×10^{-6} ($v' = 3$) are detected. However, $v' = 5$, with a FCF of 2.4×10^{-7}, is not detected.

In addition to the $1\,^3\Pi_g$ line data, we scanned the predicted location of quasi-bound vibrational levels of the $B\,^1\Pi_u$ state, which corresponds to the Hund's case (c) $3\,(1_u)$ state. Levels of this state were accurately measured by Amiot and Vergès using optical-optical double resonance and Fourier-transform spectroscopy

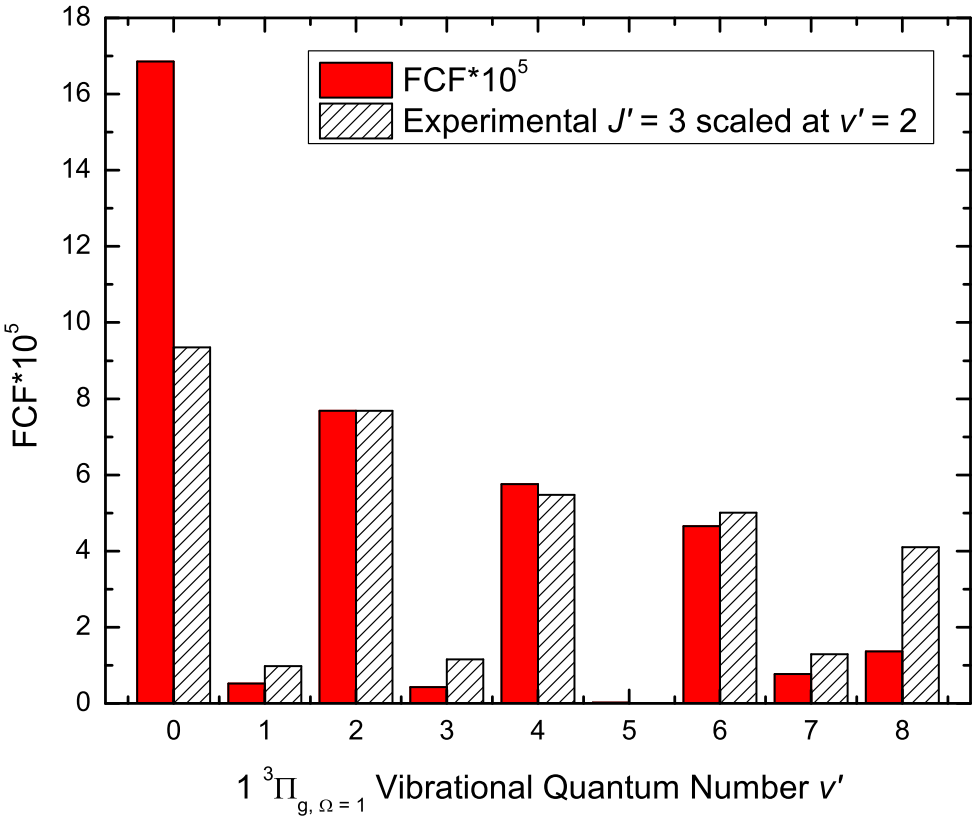

Fig. 4.2: Comparison of FCF calculations to experimental data. The lower level in the FCFs is the highest bound state of the lowest triplet potential, $a\,^3\Sigma_u^+$, $v'' = 39$, which closely approximates the zero-energy scattering state. The excited state potentials are from Ref. [39]. The experimental data are obtained using PA from a Ti:Sapphire laser and REMPI at 355 nm from a tripled Nd:YAG laser and are normalized to agree with theoretical FCFs at $v' = 2$.

in Ref. [74,75]. If our model is accurate, however, any photoassociation to this state must, by selection rules, originate from free atoms of *gerade* symmetry, and therefore must come from the $X\,^1\Sigma_g^+$ state. This state has a very short-range inner wall, and does not give enhanced FCFs for excitation to higher bound states. The

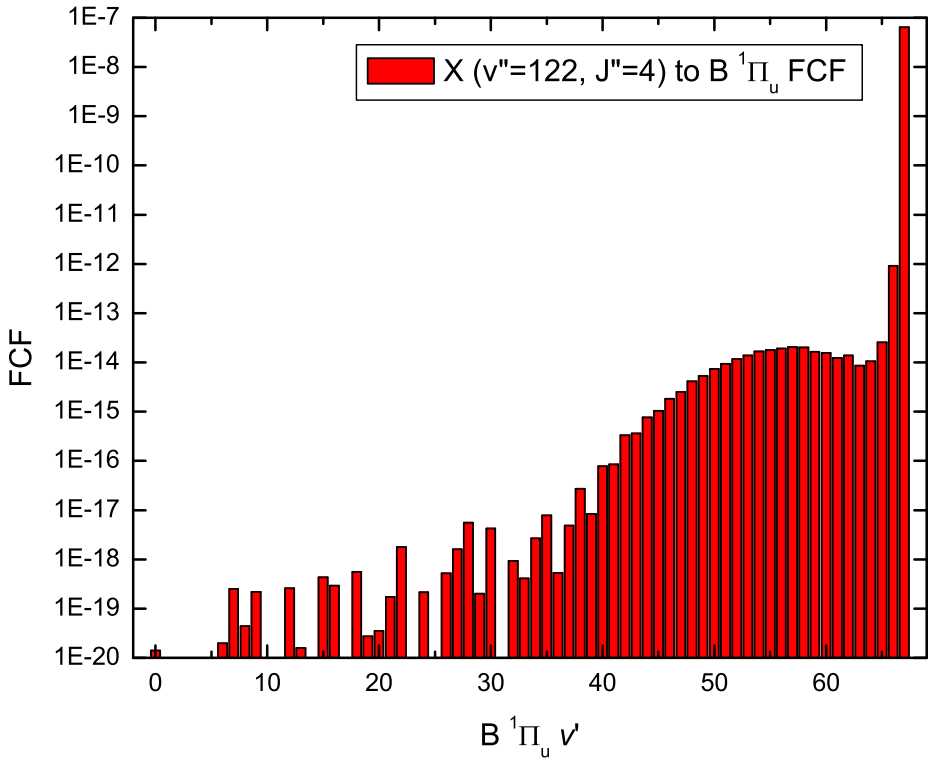

Fig. 4.3: FCFs for excitation to the $B\,^1\Pi_u$ state from the $X\,^1\Sigma_g^+$ state. Although the last two levels have dramatically increasing FCFs, it should be noted that, since they are quasibound, this transition strength is spread over a larger energy range. From Ref. [75], $v' = 66, J' = 60$ has a width of 0.134 cm^{-1}, and $v' = 67, J' = 41$ has a width of 0.561 cm^{-1}.

FCFs for transition to the $B\,^1\Pi_u$ state from the $X\,^1\Sigma_g^+$ state are shown in Fig. 4.3. Even the largest FCF to this state is $< 1 \times 10^{-7}$, and the vast majority of FCFs are $< 1 \times 10^{-13}$. These are well below the level of detectability. We will discuss our detection sensitivity below.

We have measured statistics of laser scan data in the vicinity of the B state $v' = 65$. Our scans have noise with a standard deviation of 0.18 ions per

shot over several scans. This is easily capable of 5σ detection of a single ion, and several stray ions are indeed observed within the correct boxcar gate during the scan. These are not repeatable, and thus cannot be spectroscopic features. Additionally, they show an exponential drop-off characteristic of our real-time boxcar shot averaging rate (typically a 10-shot rolling exponential average). Other than these, no lines are detected near the predicted $v' = 65$ energy.

In a similar scan, the $1\,^3\Pi_{g,\,\Omega=1}$, $v' = 8$ level is detected. Between lines, the scan background shows a standard deviation of 0.33 ions per shot, comparable to the average mentioned above. The peak line height is 9.18 ions above the baseline. Based on the FCF of 1.36×10^{-5} for this level, we are sensitive to FCFs as small as 1.3×10^{-6} with average noise levels.

4.4 Conclusion

We have presented a model of short-range photoassociation in an alkali dimer that is both conceptually and computationally simple. Any short-range excitation may be modeled by the FCF of a transition from the zero-energy continuum (or as a proxy, the highest bound vibrational level) of the lowest triplet state, so long as the transition is allowed in the appropriate Hund's case. Generally, the correct coupling description is case (a) or (c), with case (c) likely being more important in heavier alkalis with strong spin-orbit coupling.

We have presented experimental data in $^{85}Rb_2$ that is detected by single-photon ionization and should accurately reflect molecule production regardless of vibrational level. These data show quite reasonable agreement with the predictions of our FCF calculation.

Chapter 5

Long-Range Rydberg Molecules

5.1 Introduction

Long-range Rydberg molecules are a class of molecules formed by a novel bonding mechanism. This mechanism was first introduced by Du and Greene in Ref. [76] and extended by Greene *et al.* in Ref. [77]. It results in two types of long-range Rydberg states, including "trilobite" molecules (perturbed hydrogenic states), nicknamed for the resemblance of the electron wavefunction to trilobite fossils. These molecules are characterized by the s-wave scattering of a Rydberg electron on a nearby ground-state atom. There are two classes of these molecules: low-ℓ ($\ell \leq 2$) and high-ℓ. The high-ℓ molecules are the true trilobites, with deep potentials and a large permanent dipole moment on the order of a kilodebye. They are actually composed of multiple quasidegenerate high-ℓ states. There is a similar class of molecules, also with deep potentials and a large permanent dipole moment, termed "butterfly" molecules, that result from p-wave scattering of Rydberg electrons [78].

The low-ℓ states of both s-wave and p-wave scattering types have shallower potentials with a smoother shape. The interaction is proportional to the square of the electron wavefunction for s-wave scattering, and to the square of the gradient of the electron wavefunction for p-wave scattering [79]:

$$V(R) = a_s(R)|\psi_e(R)|^2 + 6\pi a_p^3(R)|\nabla\psi_e(R)|^2. \quad (5.1)$$

Several other groups are doing experiments with long-range Rydberg molecules, including true trilobite molecules. Of particular note are the groups of Shaffer and Pfau. The first confirmation of the existence of these states was from data taken in an Rb heat-pipe oven in 2006 [80]. The creation of ultracold long-range Rydberg molecules was achieved by a 2009 collaboration of Shaffer and Pfau, also in Rb [81]. The first permanent dipole moment in these states was measured in 2011 [82]. Larger dipole moments (up to 100 debye) were measured in Cs_2 in 2012 [83]. Finally, true high-ℓ trilobite molecules were formed in Cs by Shaffer *et al.* in 2015 [84]. New theoretical work has also been continued on these exotic molecular states [85].

Our own previous detection [40] of low-ℓ long-range Rydberg $^{85}Rb_2$ molecules was similar to the work of [80] in that it detected low-n Rydberg states, $n = 7$, 9 – 12. We scanned a region of over 100 cm^{-1} with a doubled pulsed dye laser at a resolution of ~ 1 cm^{-1} to obtain a spectrum.

In addition to the lower n that we study compared to Pfau and Shaffer, we also use a technique with other important differences. Pfau's work involves two-photon photoassociation of ^{87}Rb that is prepared in an Ioffe-Pritchard trap at a density of 1.5×10^{13} cm^{-3} and a temperature of $3.5\,\mu K$ [81]. Shaffer's experiment utilizes a far off-resonance trap (FORT) of Cs with a density of 5×10^{13} cm^{-3} and a temperature of $40\,\mu K$ [84]. The densities in both of these experiments are more than two orders of magnitude higher than our MOT (1×10^{11} cm^{-3}) and, in the Rb apparatus of Pfau, 1.5 orders of magnitude colder (our MOT is $100\,\mu K$). By exciting bound molecules to long-range Rydberg states, rather than free atoms,

we are able to produce them at densities and pressures that are technically simpler to achieve.

In this chapter, we study selected lines at higher resolution to identify structure and measure the autoionization rate of the long-range Rydberg molecules.

5.2 Experiment

The general design of our experiment is similar to our earlier work [73,40]. Details of much of the apparatus can be found in Chapter 2 of this dissertation. Specific details will be expanded below.

A schematic representation of our experimental procedure is shown in Fig. 5.1. After cooling atoms in a magneto-optical trap (MOT) to $\sim 100\,\mu$K we perform photoassociation to $v' \simeq 173$ of the $1\,(0_g^-)$ state [58] at $12,561.8\,\mathrm{cm}^{-1}$ (see Fig. 2.2). As we have full rotational resolution, we typically photoassociate to the $J' = 1$ line. The photoassociation laser is a fiber-coupled continuous-wave (CW) Coherent 899-29 Ti:Sapphire laser (medium-wave optics) that delivers 450 mW of optical power to the vacuum chamber. This state decays primarily to the $v'' = 35$ and 36 levels of the $a\,^3\Sigma_u^+$ state. These precursor molecules are then excited to the target $^3\Sigma_g^+$ state at the $5s + 7p$ asymptote via a doubled nanosecond pulsed amplifier.

The pulsed amplifier is shown in schematic form in Fig. 2.8. This amplifier was originally designed for other Rydberg work at UConn [50]. It is composed of three Bethune dye cells [51] that amplify a fiber-coupled Ti:Sapphire (899-29, modified short-wave optics). The Ti:Sapphire beam sets the frequency that the dye cells amplify, acting in place of a dye-cell oscillator such as our ND6000 dye laser uses. The Ti:Sapphire CW power must be sufficiently high (above ~ 100 mW) at

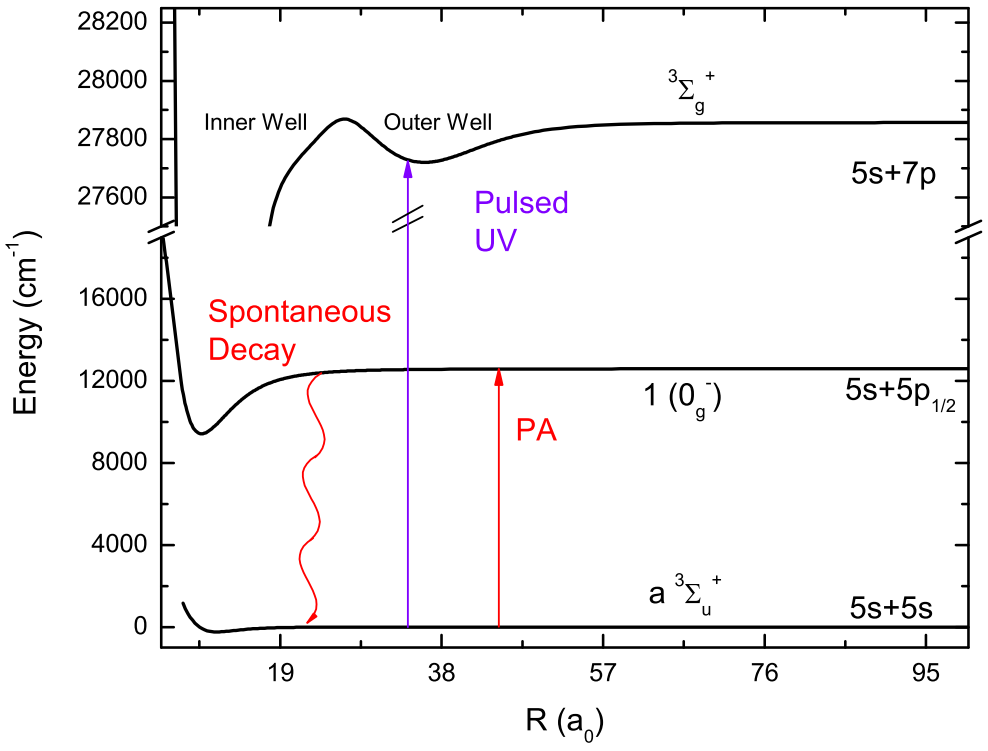

Fig. 5.1: The experimental scheme for long-range Rydberg molecule production. We photoassociate to $v' \simeq 173$ of the $1\,(0_g^-)$ state below the $5p_{1/2}$ asymptote. This level spontaneously decays to the upper vibrational levels of the $a\,^3\Sigma_u^+$ state, especially $v'' = 35$ and 36. After these precursor molecules are formed, they are excited to the long-range Rydberg $^3\Sigma_g^+$ state at the atomic $7p$ asymptote.

the first cell to saturate the amplifier. These cells are pumped by a Spectra-Physics Quanta-Ray (LAB-150) injection-seeded Nd:YAG laser. The Nd:YAG injection seed is an OEM option that both stabilizes the frequency and the power envelope of each pulse. Spectra-Physics specifies a reduction in the second-harmonic 532 nm linewidth from < 1.0 cm^{-1} unseeded to < 0.003 cm^{-1} with the injection seeder [86]. Injection seeding the Nd:YAG is vital to achieving stable, narrow

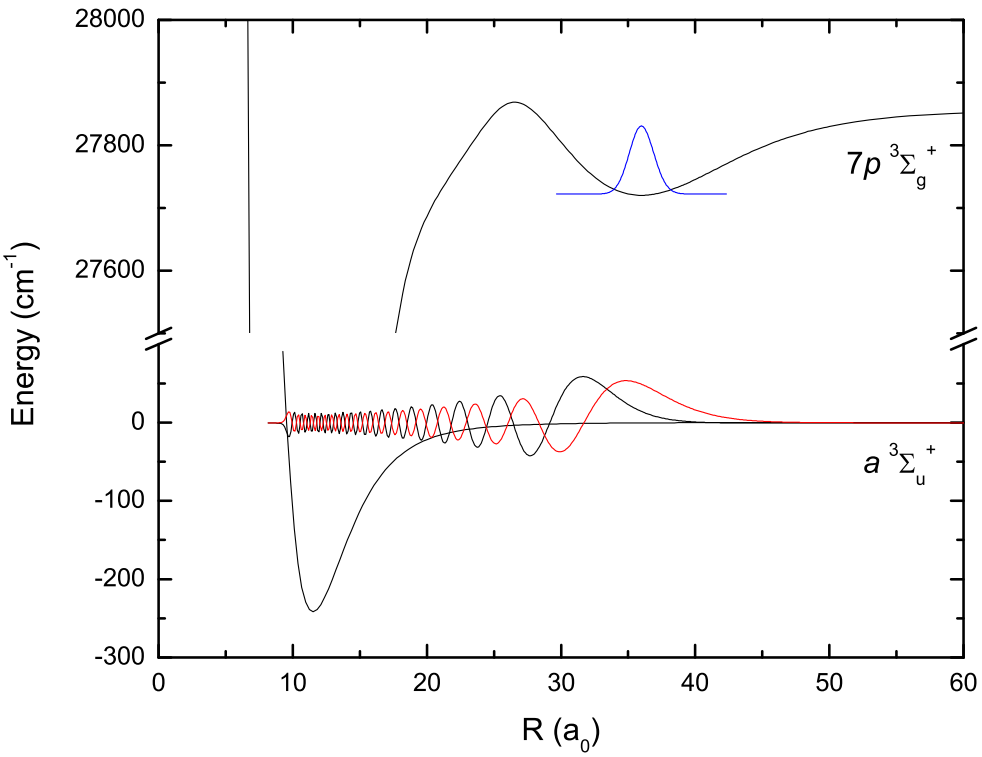

Fig. 5.2: Wavefunctions of the $a\,^3\Sigma_u^+$ state $v'' = 35$ (black) and $v'' = 36$ (red) and Rydberg $7p\ ^3\Sigma_g^+$ state outer well $v' = 0$.

pulse bandwidth. The pulse-amplified bandwidth of second-harmonic radiation at ~ 360 nm generated by a KDP crystal was measured by scanning through the atomic $7p_{1/2}$ line at low pulse energies. This resulted in a measured linewidth of ~ 150 MHz (see Fig. 2.9). Typical UV pulse energies are 0.4 mJ per pulse (see Fig. 2.10).

The high-lying vibrational levels we create in the $a\,^3\Sigma_u^+$ state are ideal for accessing the long-range Rydberg state that correlates to the atomic $7p$ asymptote. The outer turning points of these wavefunctions match the position of the $^3\Sigma_g^+$ outer well $v' = 0$ state very well, as shown in Fig. 5.2. The $v' = 35$ wavefunction,

shown in black, has an outer turning point maximum amplitude at ~ 30 a_0, and the $v' = 36$ wavefunction, in red, has a maximum amplitude in the final lobe at ~ 35 a_0. The potential shown in Fig. 5.2 and used to generate the displayed wavefunctions is from Ref. [73].

After excitation, the long-range Rydberg molecules autoionize into a Rb_2^+ ion and a free electron. The Rb_2^+ ions are collected by our ion optics and, after a free-flight region, are detected by a discrete dynode multiplier (ETP model 14150). The detected signals are mass-selected for dimer ions by time-of-flight mass spectrometry and integrated by a boxcar integrator (SRS SR250).

To reduce contamination of the molecular channel by atomic ions, the MOT lasers are turned off for $10\,\mu$s before and after each UV laser pulse. A special effort was made to ensure that the trap laser AOM shuts off as completely as possible during the UV pulses. An RF switch was added to the IntraAction 40MHz driver (Mini-Circuits ZX80-DR230-S+) between its oscillator and internal amplifier. This improved the isolation from 55 dB to 60 dB, with 30 mW of trap power at the fiber output. The residual power is only $\sim 3\times$ the measured power when the laser is fully blocked from the fiber input.

All spectra shown in this chapter were obtained using several forms of averaging. The inner-well states were acquired using 10-shot exponential averaging on the boxcar integrator. The final spectra are composed of multiple scans that were averaged using the Mathematica package in Appendix D. The outer-well states were recorded using single-shot sampling from the boxcar integrator; the resulting spectra were then filtered using Mathematica's low-pass Fourier filter. This type of post-processing filter does not distort the line shape of spectral features. Multiple scans were again averaged as above, with the addition of supplementary

linearization, also provided in Appendix D.

The reported frequencies for the spectra are laser frequency, not the absolute energy of the spectral features. There may also be rare errors on the order of 0.22 cm^{-1} due to the design of our 899-29 wavemeter.

5.3 Low-Resolution Data and Franck-Condon Factors

As seen in Fig. 5.2, the overlap for excitation to the bottom of the outer well of the long-range Rydberg state is quite good. As expected, this translates into large Franck-Condon factors (FCFs). The factor, FCF = $|\langle\psi_{v'}|\psi_{v''}\rangle|^2$, is typically a good approximation for the transition probability and is discussed in greater detail in Chapter 1.4. Despite the good approximation the FCF provides, adding the transition dipole moment to the calculation would be beneficial, but unfortunately the transition dipole moment from the $a\,^3\Sigma_u^+$ potential to the $7p\,^3\Sigma_g^+$ potential is currently unknown. The sum of the FCFs for $v'' = 35$ and $v'' = 36$ with $J'' = 0$ to all levels of the inner and outer wells was calculated using LEVEL 8.2 [32] and the potential shown in Fig. 5.2 and can be found in Tables B.4 and B.5 in Appendix B. This sum is shown in Fig. 5.3, on the same horizontal axis as our low-resolution data from [40].

It should be noted that, although we discuss the inner well and outer well of the $^3\Sigma_g^+$ state, they are actually a single system. What we have designated as an inner well or outer well level is nonetheless an eigenstate of the entire potential. Tunneling through the barrier, although small, does allow for some wavefunction amplitude to leak into the other well, especially near dissociation. The highest bound state of the system, $v' = 232$ (or $v' = 73$ of the outer well), has some amplitude in the inner well, but its amplitude in the outer well is ~ 422 times

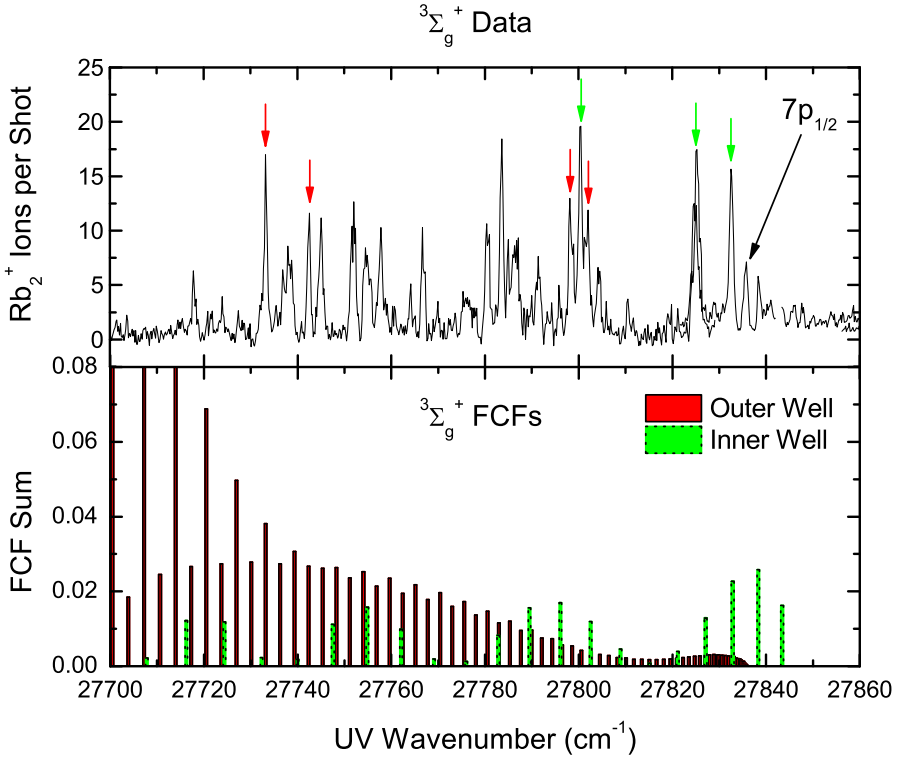

Fig. 5.3: The lower panel of this figure shows the sum of FCFs for transition to the long-range Rydberg $^3\Sigma_g^+$ potential from the $a\,^3\Sigma_u^+$ $v'' = 35$ and 36 levels. Transitions to the inner well are shown in green, while those to the outer well are shown in red. The upper panel shows our low-resolution data from Ref. [40]. Spectral regions that were studied at higher resolution are marked with red arrows for outer-well levels, shown in Figs. 5.12 and 5.13. The corresponding regions for inner-well levels are marked with green arrows, shown in Figs. 5.7, 5.8, and 5.11 (two weak outer-well levels are also shown in Fig. 5.11).

greater. The highest bound level of the inner well, $v' = 219$ ($v' = 158$ of the inner well) has $1,890$ times more amplitude in the inner well than in the outer well. The amplitude is measured as the peak to trough height of the first oscillation on either side of the potential barrier. These vibrational levels are shown in Fig. 5.4.

Fig. 5.3 also has several arrows indicating particular vibrational levels. At

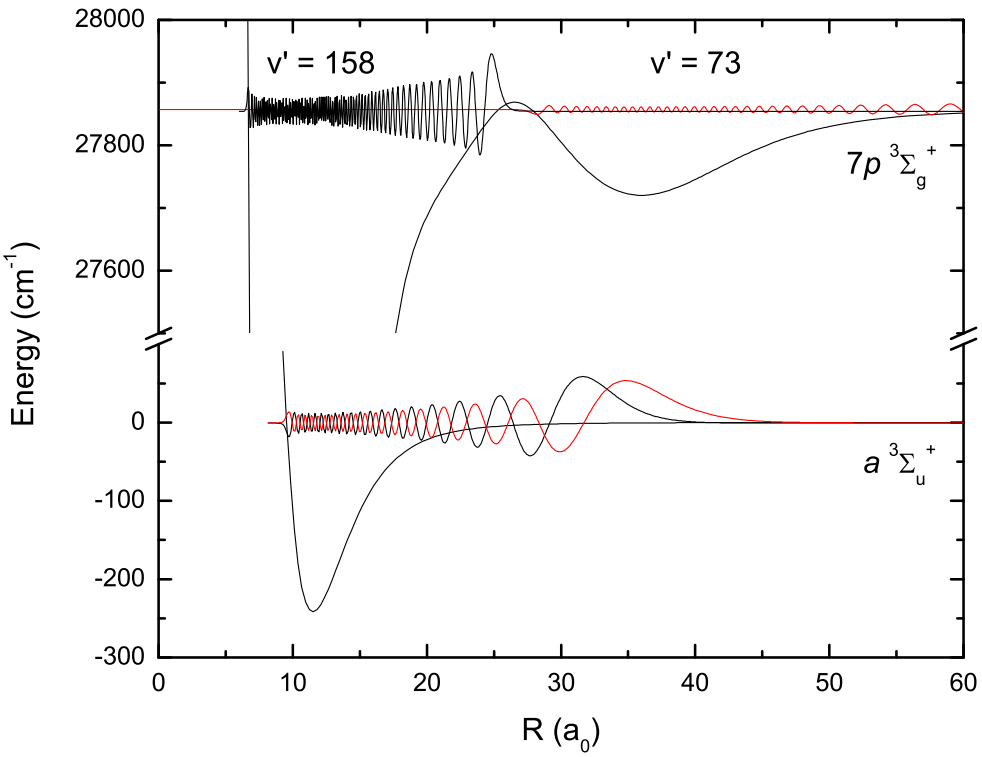

Fig. 5.4: Wavefunctions of the $a\,^3\Sigma_u^+$ state $v'' = 35$ (black) and $v'' = 36$ (red) and Rydberg $7p\,^3\Sigma_g^+$ state outer well $v' = 73$ and inner well $v' = 158$.

higher energies, $27,800$ cm^{-1} and above, the three green arrows indicate lines we have measured at high resolution and have assigned to the inner well. At lower energies, marked in red near $27,730$ cm^{-1}, are two more regions in which we have observed high-resolution spectra assigned to the outer well. Two additional outer-well states are observed at $\sim 27,800$ cm^{-1}, but are weak and poorly-resolved.

The $^3\Sigma_g^+$ potential that we used to calculate these FCFs, from Ref. [73], is not calculated in a spin-orbit coupled basis, and thus has inherent inaccuracies when compared to empirical data. The spin-orbit splitting between the $7p_{1/2}$ and $7p_{3/2}$ in ^{85}Rb is 35 cm^{-1}, so we should expect uncertainties of that scale.

The $a\,^3\Sigma_u^+$ potential used for these calculations is the semi-empirical potential of Ref. [29] and is considered to be highly accurate.

Although the spin-orbit splitting was not taken into account in the calculation, we can still identify to which asymptote certain states correspond. In Fig. 5 and Tab. 1 of Ref. [33], we see that, at the $5p$ asymptotes, all of the components of the $^3\Sigma_g^+$ state correspond to the $5p_{1/2}$ limit, and all components of the $^3\Pi_g$ state correspond to the $5p_{3/2}$ limit. Thus we know that the $^3\Sigma_g^+$ and $^3\Pi_g$ states of the $7p$ asymptote will similarly correlate to the $7p_{1/2}$ and $7p_{3/2}$ asymptotes, respectively.

There are several interesting features of the FCFs. The first is that the inner and outer wells each dominate in a different energy range, although the change in strength of the inner-well FCFs is less significant. The inner well has the highest excitation probability for the highest several vibrational levels of the Rydberg molecular state, near the atomic asymptote. The outer well has very low excitation probability near the atomic asymptote, but quite high excitation probability at the bottom of the well.

A second feature of note is the strong even-odd oscillation in outer-well FCFs at low energy. This effect is strongly dependent on the R value of the outer turning point, and can be seen in the difference between the FCFs from $v'' = 35$ and $v'' = 36$ in Fig. 5.5 and Fig. 5.6, respectively. Full tables of these FCFs are in Appendix B.

Fig. 5.5 shows some oscillations in the $v'' = 35$ FCFs at low v', and also shows a maximum FCF of 4.4% that is reached at $v' = 0$. Recalling the good wavefunction overlap with $v' = 0$ shown in Fig. 5.2, this is unsurprising.

In Fig. 5.6, we see much stronger even-odd oscillations at the bottom of the well, and weaker oscillations extending toward the atomic asymptote. We also

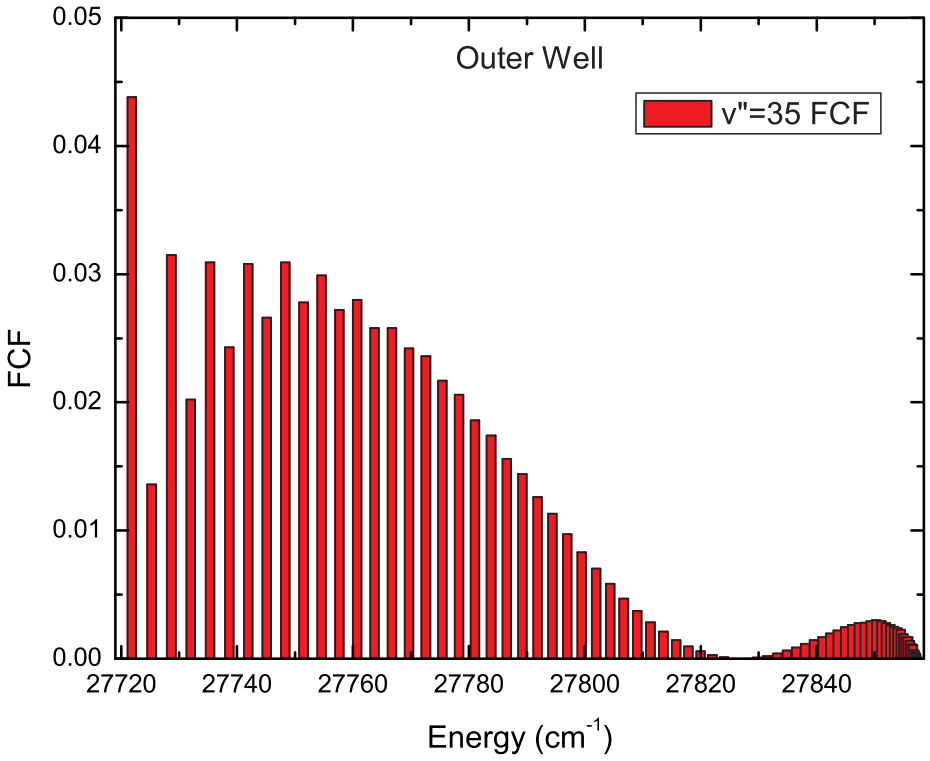

Fig. 5.5: The Franck-Condon Factors for transitions from the $a\,^3\Sigma_u^+$ $v'' = 35$ to the Rydberg molecular potential are shown. The maximum FCF is 4.4% for $v' = 0$.

see a dramatically larger FCF in the lowest several even levels, of up to 38.7% for $v' = 0$, which is the source of the vast majority of the FCF strength seen in Fig. 5.3. This is due to the extremely favorable overlap of the outer turning point of $v'' = 36$ with $v' = 0$ of the outer well.

What is the cause of the even-odd oscillation in the FCFs? It is important to note that the outer well is, like many potentials, fairly harmonic near the bottom. Thus its deeply-bound eigenstates are also fairly similar to the eigenstates of a

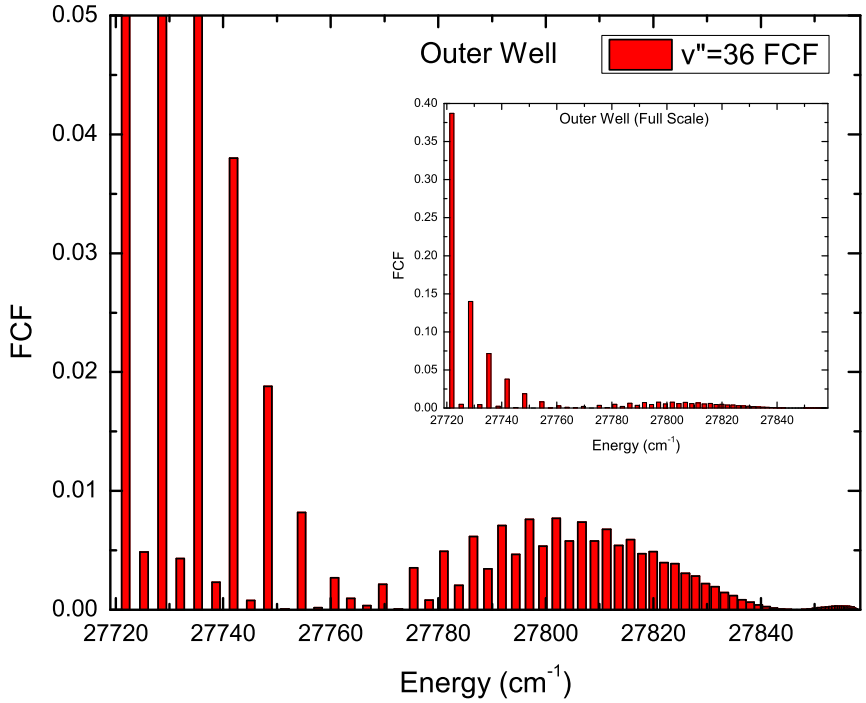

Fig. 5.6: The Franck-Condon Factors for transitions from the $a\,^3\Sigma_u^+$ $v'' = 36$ to the Rydberg molecular potential are shown. The scale of the main figure is the same as in Fig. 5.5, but the inset shows the full scale of the lower FCFs. Note the dramatic increase in probability at low even values of v' (to 38.7% for $v' = 0$) when compared with the FCFs in Fig. 5.5

harmonic oscillator. In an ideal harmonic oscillator, the $v' = 1$ wavefunction has one node, which will be located at the same R as the maximum in the wavefunction of the $v' = 0$. The location of this node means that a fairly-localized wavefunction (in a lower electronic potential) that has good overlap with the $v' = 0$ state must have poor overlap with $v' = 1$, and thus a small FCF.

Similarly, the $v' = 2$ wavefunction, which has two nodes, will have an extremum located at the same R as the maximum of $v' = 0$. (extremum rather

than maximum because the sign of the wavefunction may flip depending on the phase convention. Nonetheless, $|\psi|^2$ will have a maximum.) This lobe of the wavefunction will have a lower amplitude than in $v' = 0$, and the two flanking lobes will partially cancel the overlap, resulting in a weaker but still-strong FCF. This process continues up the roughly harmonic well, with the alternation in strength gradually losing contrast. Anharmonicity in the real potential, other lobes in the lower wavefunction, and imperfect alignment of the outer lobe all further reduce the alternation. Because the outermost maximum of the $a\,^3\Sigma_u^+$, $v'' = 36$ level is near R_e' of the $^3\Sigma_g^+$ outer well potential, but the maximum of the $v'' = 35$ level is well inside R_e' of the $^3\Sigma_g^+$ outer well, the contrast ratio between even and odd FCFs is much greater (79.8× *vs.* 3.2× for the $v' = 0$:1 ratio) in the $v'' = 36$ plot (Fig. 5.6) than in the $v'' = 35$ plot (Fig. 5.5).

5.4 High-Resolution Scans

In our previous work on these states [40], we relied on REMPI measurements from the thesis of Ye Huang [34] to identify the distribution of $a\,^3\Sigma_u^+$ state molecules, and believed that most of the molecules were in $v'' = 35$. With our pulse-amplified CW laser providing a linewidth of ~ 150 MHz, or 200× narrower than our previous work, we can detect the ground-state distribution more accurately than it has been measured in our apparatus before.

In Fig. 5.7, two sets of inner-well lines are shown (in Fig. 5.3, these are indicated by the two highest-energy green arrows). Each spectrum contains two prominent triplets of lines. According to calculations from LEVEL, the $a\,^3\Sigma_u^+$ state $v' = 35$ level is bound by 0.8065 cm^{-1}, and the $v' = 36$ level is bound by 0.4161 cm^{-1} (see Table B.2 in Appendix B for full listing of vibrational levels).

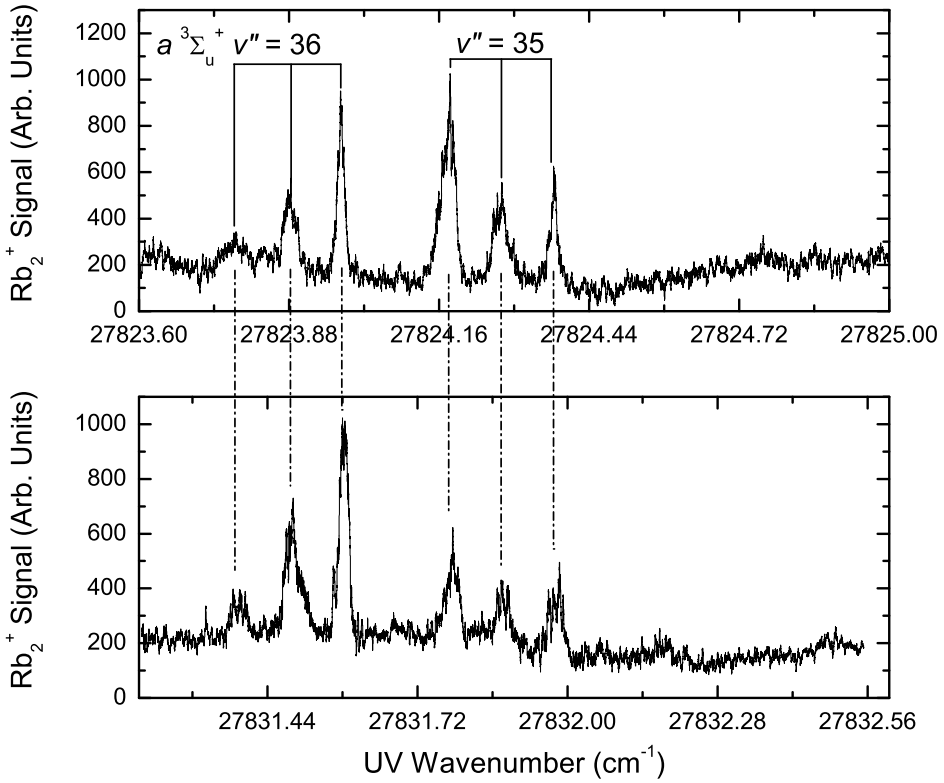

Fig. 5.7: Two inner-well spectra are shown, aligned to demonstrate their similarities. Both lines show the same vibrational and hyperfine structure from the $a\,^3\Sigma_u^+$ state. They also show roughly comparable relative intensities among the $v'' = 35$ and $v'' = 36$ lines.

The difference of ~ 0.39 cm^{-1} matches the spacing from the first line of one triplet to the first line of the next, and so on for the second and third components of the triplets. Instead of our $a\,^3\Sigma_u^+$ state population residing primarily in the $v'' = 35$ level as we previously thought, we appear to have a nearly equal balance of $v'' = 35$ and $v'' = 36$ molecules. Even this observation, though, is affected by the FCFs of each a-state vibrational level, and the apparent line strength will shift with v'. For example, Fig. 5.11 shows a very different ratio of $v'' = 35$ to 36 at an inner-well vibrational level that is ~ 25 cm^{-1} more deeply bound than the level shown in

the upper panel of Fig. 5.7.

Similarly, within each triplet the spacing between the first and second lines is the same as the spacing between the second and third. This spacing is consistent with the atomic ^{85}Rb ground-state hyperfine splitting between $F = 2$ and $F = 3$ of 0.1012 cm^{-1} [48]. The lowest-energy component (which must come from the highest-lying ground-state hyperfine level) must be the $|F = 3\rangle + |F = 3\rangle$ asymptote. The next highest corresponds to $|F = 2\rangle + |F = 3\rangle$, and the highest-energy component of the triplet corresponds to the $|F = 2\rangle + |F = 2\rangle$ atomic asymptote.

Traditionally, it is assumed that photoassociation acts only on the electron orbital degrees of freedom, not altering electronic or nuclear spin (See "Selection Rules" in Ref. [20]). Nuclear spin *must* flip, however, to explain the states we see. Our MOT selects primarily for the $F = 3$ state, although a small $F = 2$ population can be observed in spectroscopy as "hyperfine ghosts". Since this population is spectroscopically distinct, we know that we are selecting only for $F = 3$ atoms in our initial photoassociation step. As we start with an initial population consisting of only $|F = 3\rangle + |F = 3\rangle$ molecules and end with a qualitatively equal mix of all three asymptotes after a two-photon process, up to one nuclear spin change must accompany each electronic transition.

So far in this analysis, we have discussed only the asymptotic spacing of the molecular hyperfine levels. Since we are actually dealing with bound states, it follows that the molecular hyperfine potentials must be essentially parallel to each other as they come in to shorter distances. Indeed, this is reflected in the new potential curves and vibrational eigenstates calculated by Professor Tiemann [87].

Aside from the hyperfine distribution, we also must consider the rotational

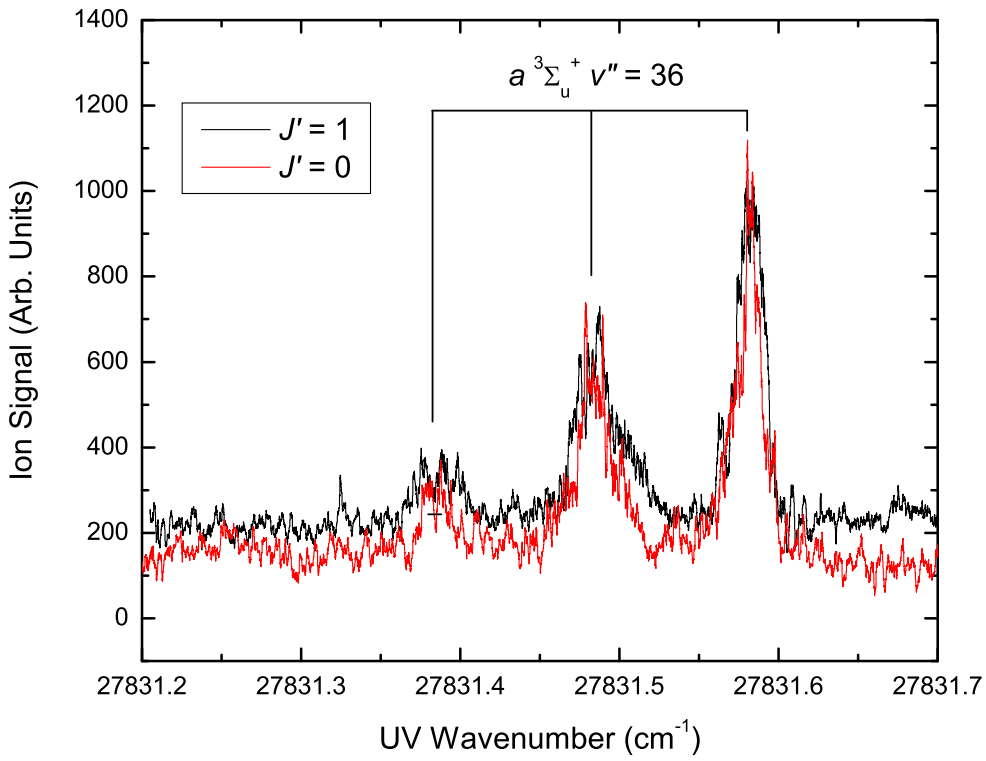

Fig. 5.8: Two scans of the same inner-well line are shown. In the first scan (black), the precursor $a\,^3\Sigma_u^+$ state molecules were formed by photoassociation to the $1\,(0_g^-)\,v' = 173$, $J' = 1$ level. The second scan (red) was identical except that the photoassociation was locked to the $J' = 0$ level.

distribution. In general, we photoassociate to the $J' = 1$ level of a state because it has the greatest formation rate, and this is true of the $1\,(0_g^-)$ $v' = 173$ level as well. From the selection rules given in Chapter 1.3 we see that $\Delta J = \pm 1$ and $\Delta J = 0$ if $\Omega \neq 0$, which is true for the $\Omega = 1$ component of the $a\,^3\Sigma_u^+$ state. Thus for $J' = 1$, we can have $J'' = 0$, 1, or 2. If instead we photoassociate to the $J' = 0$ line, we can have $J'' = 0$ or 1. This comparison between $J' = 1$ and $J' = 0$ photoassociation was performed experimentally, and the result can be seen

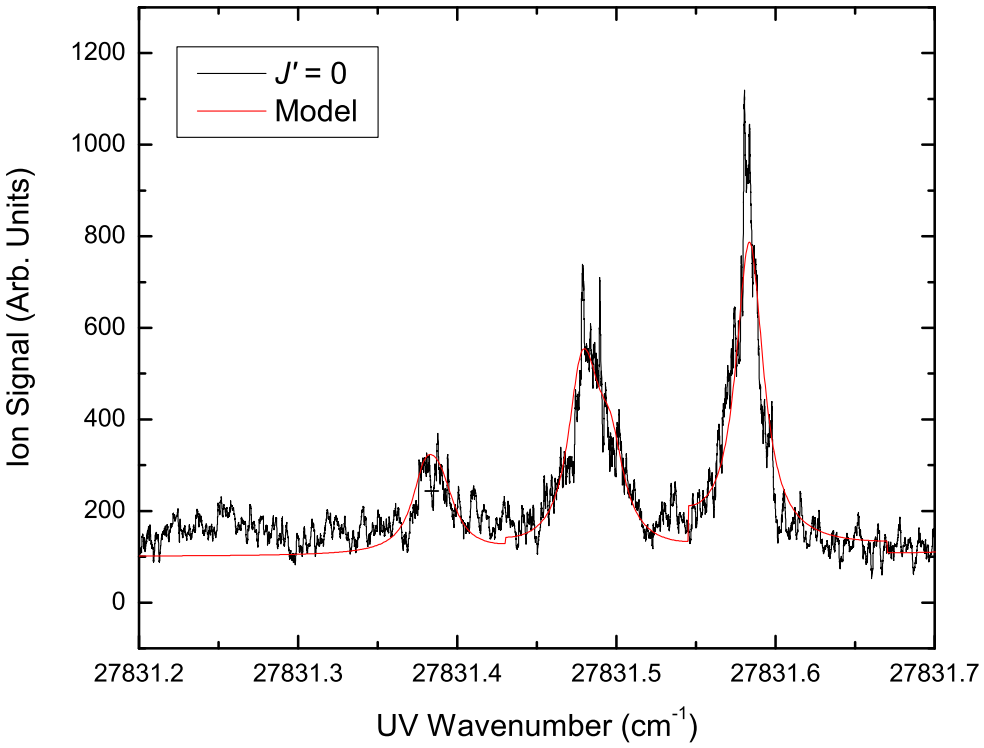

Fig. 5.9: The $J' = 0$ level from Fig. 5.8 is shown with a model fit based on semi-empirical data [87]. $N'' = 0$ and 1 are included. The model line heights are artificially scaled to match the data so that widths may more easily be compared.

in Fig. 5.8.

The data from Professor Tiemann [87] also includes rotational components, although in his case (e) basis set the appropriate quantum number is N, where $\mathbf{N} = \mathbf{J} - \mathbf{S} = \mathbf{L} + \ell$. Rotational quanta $N'' = 0$, 1, and 2 were included to match the case of $J' = 1$ photoassociation. In $J' = 0$ photoassociation (including $N'' = 0$ and 1), we can see a narrower distribution in both the data and the model, which is shown in Figs. 5.9 and 5.10. The Hamiltonian and computational method he uses for these calculations is described in Ref. [88], and his potentials

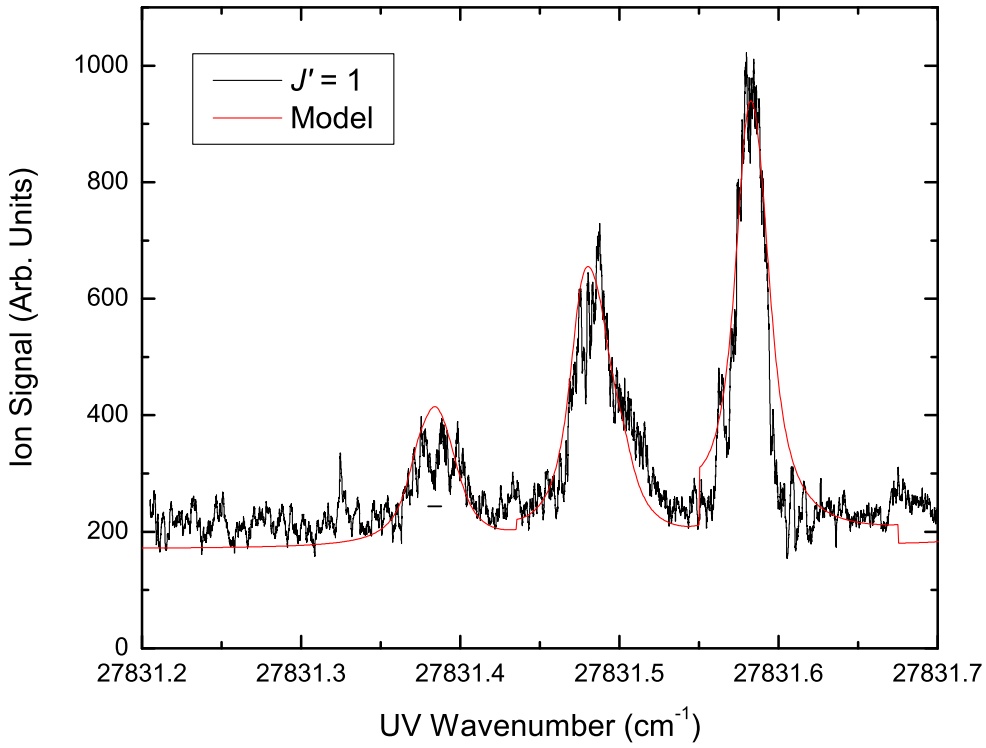

Fig. 5.10: The $J' = 1$ level from Fig. 5.8 is shown with a similar model fit. Here $N'' = 0$, 1, and 2 are included, along with the same height scaling.

and hyperfine functions are published in Ref. [29]. Our model assumes that the $a^3\Sigma_u^+$ state levels have a negligible linewidth due to their metastable nature. The laser linewidth is input as 150 MHz, and the excited state linewidth is varied to match the observed spectrum. All lines are modeled as having Lorentzian profiles.

The fit shown models the excited-state natural width as 450 MHz, with no substructure. As some substructure must be present due to multiple hyperfine and rotational levels, this represents an overestimate of the linewidth. The molecular hyperfine is expected to follow the atomic hyperfine splitting, much as we see in the ground state. The hyperfine A constant is given in Ref. [89] for the ^{85}Rb $7p_{1/2}$

state as 0.000590(3) cm^{-1}. There is no B constant for the $7p_{1/2}$. The standard form of the hyperfine shift is [90]:

$$\frac{E_{hf}}{h} = \frac{AC}{2} + B\left[\frac{\frac{3}{4}C(C+1) - I(I+1)J(J+1)}{2I(2I-1)J(2J-1)}\right], \tag{5.2}$$

where $C = F(F+1) - I(I+1) - J(J+1)$. With $B = 0$ this reduces to $\frac{E_{hf}}{h} = \frac{AC}{2}$. For our values of $J = 1/2$, $I = 5/2$, and $F = 2$, 3 we find an atomic splitting of $\Delta E_{hf}/h = 3A = 0.00177$ cm^{-1}, or 53.1 MHz. With this splitting, the three molecular hyperfine asymptotes will extend over $\sim$ 106 MHz, and the shorter-range potentials will vary from this in an unknown manner. Since we cannot fully account for the effect on the short-range potentials, we will continue to use 450 MHz as an upper bound on the excited-state linewidth.

Some fraction of the linewidth could also be due to radiative decay that competes with the autoionization, but we have no estimates of this contribution. Natural linewidth is related to lifetime by $\tau = \frac{1}{\omega}$ in rotational frequency units, which becomes $\tau = \frac{1}{2\pi f}$ in Hz. A 450 MHz linewidth corresponds to an autoionization lifetime of 3.5×10^{-10} s. As this is an upper bound to the linewidth, the autoionization lifetime must be a lower bound - the states could live longer.

An interesting region of the spectrum is marked by the lowest green arrow in Fig. 5.3. This region, expanded in Fig. 5.11, contains both inner-well and outer-well states (marked by red arrows to either side in the figure), encouraging a direct comparison. The inner well, as before, has both $v'' = 35$ and $v'' = 36$ components, but now there is a strong asymmetry between them. The $v'' = 35$ component remains strong, while the $v'' = 36$ component is quite weak. We believe this is due to different Franck-Condon overlaps with the precursor molecular wavefunctions. As we explore more deeply-bound inner-well states, we are also probing the shorter

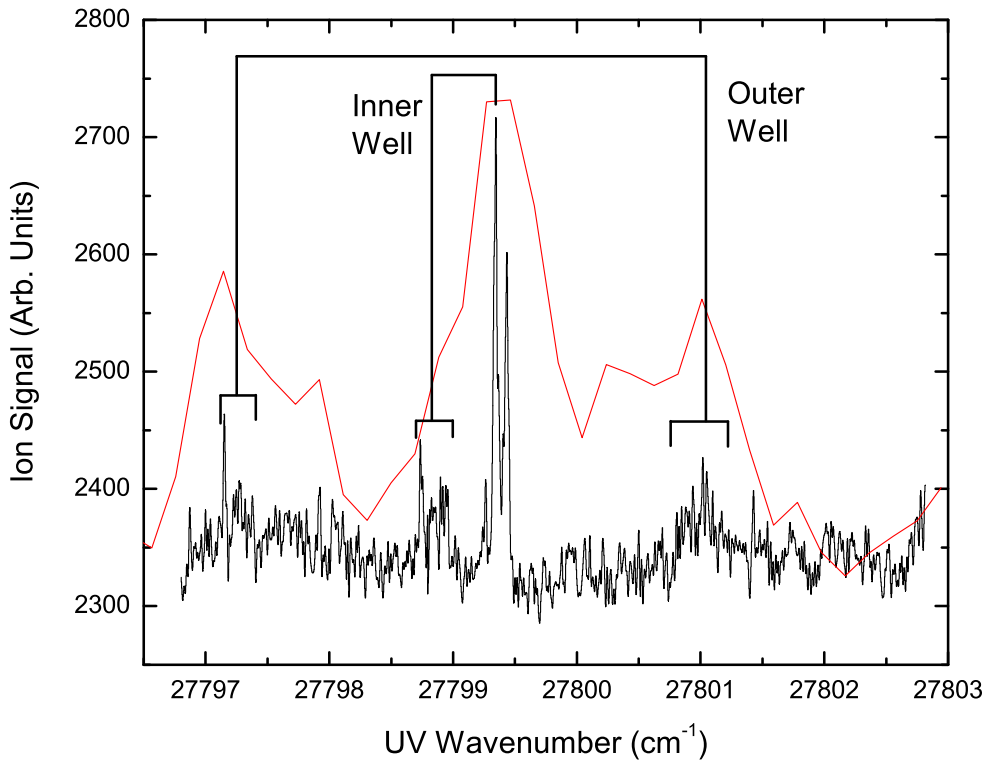

Fig. 5.11: A long scan was stitched together to show a single inner-well level with significantly-weaker outer-well levels to either side. The relative strength of these levels is qualitatively similar to the FCFs shown in Fig. 5.3. The low-resolution data from Ref [40] is seen in red. This data has been slightly shifted to match the current spectrum.

internuclear distances that favor excitation of $v'' = 35$.

To either side of the inner-well levels in Fig. 5.11, we see weak features. As can be seen in the figure, these features correspond to lines seen in our low-resolution spectra (in red). Although we cannot easily resolve the structure of these features, they are too closely-spaced to an inner-well level to be from the inner well themselves. The characteristic spacing of the inner-well energy levels in this region is ~ 5 cm^{-1}, while the spacing of the outer-well levels is ~ 2 cm^{-1}. As

each of these features is ~ 2 cm^{-1} away from the inner-well line, they can only be outer-well states. The weak nature of these lines encourages us to look at much lower energies, at the bottom of the outer well, where the Franck-Condon factors are higher by roughly a factor of 40.

In our scans of the low-lying outer-well states, Figs. 5.12 and 5.13, there is a spectral feature that does not match the ground-state hyperfine structure. This state is in nearly the same place in multiple spectra, ~ 0.04 cm^{-1} higher in energy than the lowest-energy line. In the two spectra of Fig. 5.8, there is also a very weak feature at this position. A similar feature is also present in the $v'' = 36$ component of the upper spectrum of Fig. 5.7 (the lower spectrum is the same as in Fig. 5.8).

At long range, the $X\,^1\Sigma_g^+$ state and the $a\,^3\Sigma_u^+$ state have the same van der Waals C_6, C_8, and C_{10} coefficients [20]. This gives them a very similar vibrational progression at high v'' (where the outer turning point is at long range), and leads to a significant degree of degeneracy between levels of opposite symmetry. Despite weak interaction between these states, with such small Δ_0 the states are almost completely coupled much as described in Chapter 3.4, e.g. in Refs. [28,29].

From the tables of energy levels in Appendix B, we see that the $X\,^1\Sigma_g^+$ state has levels $v'' = 118$ at -0.8351 cm^{-1} and $v'' = 119$ at -0.4294 cm^{-1}. These are, respectively, 0.0286 and 0.0133 cm^{-1} more deeply bound than the $a\,^3\Sigma_u^+$ state $v'' = 35$ and 36 levels. These spacings, however, are in the completely decoupled basis set of non-interacting potentials. In the actual potentials, the significant interactions between the triplet and singlet states are represented in the model we used to create the fits in Figs. 5.9 and 5.10.

However, these model fits do not show any extra line in the position ob-

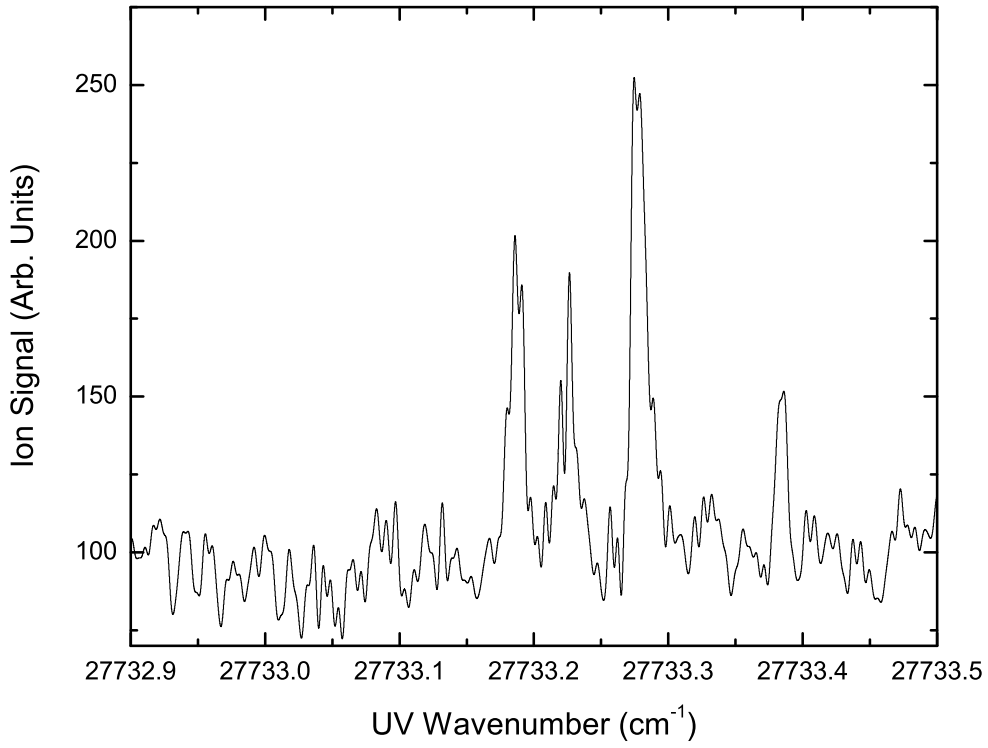

Fig. 5.12: A scan of the lowest-lying outer-well level we have detected. We believe it is $v' = 0$ of the outer well.

served. The $v'' = 34$ of the model does have a singlet-character line intermediate between two of the main groupings, but it is in between the wrong lines to match our data. Also, Franck-Condon factor calculations for $v'' = 34$ do not support strong transitions to the outer well. This is expected, due to the shorter internuclear separation of the outer lobe of the wavefunction.

One possible explanation for this extra line is that it comes from another potential curve in the same region. The most likely candidate for this is the $^3\Pi_g$ state, the potential for which was calculated at the same time as the $^3\Sigma_g^+$ and is given in Ref. [73]. This is unlikely due to the line's presence in multiple vibrational

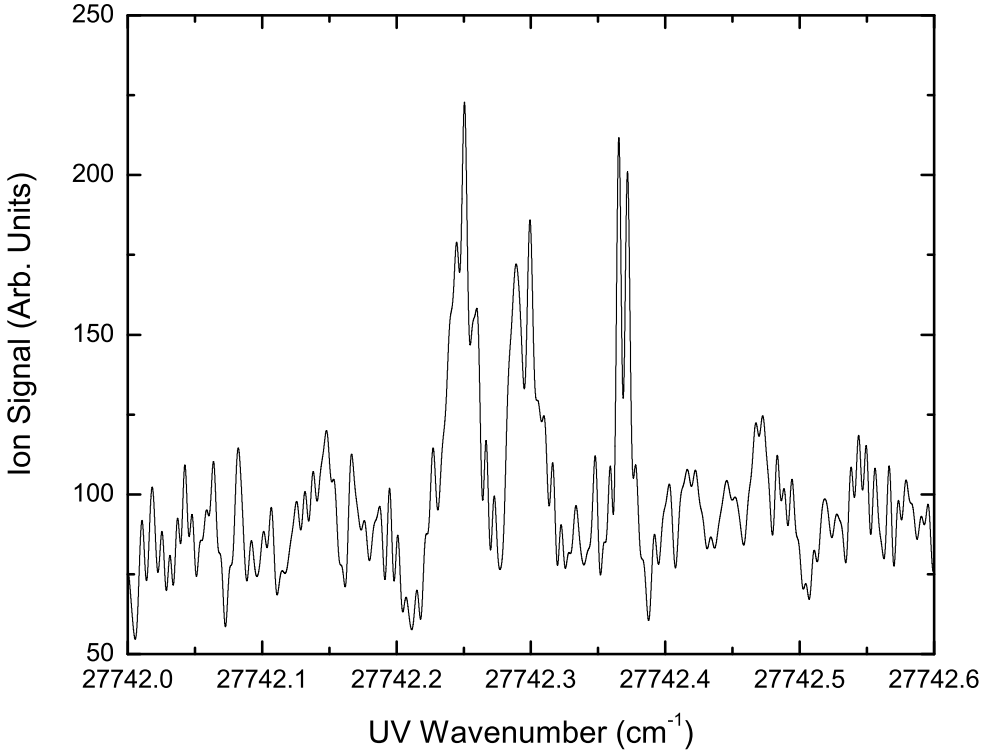

Fig. 5.13: A scan of a slightly higher level of the outer well. We believe it is $v' = 2$ based on predicted line spacings.

levels, but it cannot be ruled out.

5.5 Conclusion

We have acquired high-resolution spectra of the long-range Rydberg molecular state of $^{85}Rb_2$ at the $7p$ asymptote. This state has a short-range inner well and a pure long-range outer well, both of which have been observed. Much of the observed structure is coupled from the atomic ground-state asymptote, the hyperfine structure of which greatly complicates the spectrum. After modeling this

structure, we have placed an upper bound on the autoionization lifetime of the Rydberg molecule of 3.5×10^{-10} s. One spectral feature of the outer well continues to elude a definite assignment, on which investigations will continue.

Chapter 6

Conclusion and Outlook

We have shown the existence of a resonant coupling between the blue-detuned $v' = 111$ level of the $2\,(0_g^+)$ state and the $v' = 155$ level of the $2\,(1_g)$ state. Although the matrix element facilitating the coupling is small, the very close energy spacing creates a strong coupling. This coupling enables the formation of large numbers of metastable $a\,^3\Sigma_u^+$ state molecules in $v'' = 18$ – 24, which can be used for other experiments, such as spectroscopy.

We have also examined the mechanism of photoassociation to short-range and blue-detuned levels. These levels are largely excited through the increased vibrational wavefunction amplitude at the inner wall of the $a\,^3\Sigma_u^+$ state. State-independent ionization measurements show a high degree of agreement with our model of this process.

Finally, we have measured high-resolution spectra of low-n long-range Rydberg molecules. These states are autoionizing with a surprisingly long lifetime. We have not been able to directly measure the lifetime, as the natural linewidth is less than the lifetime of our excitation laser. We have placed limits on the lifetime by utilizing a model of molecular ground-state hyperfine structure from Tiemann.

The next experiment will be to extend this work to the $8p$ and higher levels (we have observed up to the $12p$ at low resolution, with the exception of the $8p$

asymptote). The $Rb^+ + Rb^-$ ion-pair curve should cross the long-range Rydberg potential correlating to this asymptote, creating a fascinating interaction. This curve crossing should create shifts in the adiabatic potentials, possibly creating extra long-range potential wells or inducing predissociation.

This work can also be extended to even higher np states. First the metastable $a\,^3\Sigma_u^+$ states must be trapped in an optical dipole trap. From there, they can be transferred to longer-range states, such as $v'' = 39$, that would be dissociated by the MOT and photoassociation beams if they were left on. This transition can be achieved through stimulated Raman adiabatic passage (STIRAP), a technique for efficient transfer of molecules between states [7]. By creating longer-range precursor molecules, we create larger Franck-Condon factors for transition to the higher np states.

Appendix A

Instructions and Operating Procedures

The following sets of "instructions" are meant to be helpful guides. They are not intended to be perfectly optimal, but are practical descriptions of conditions in P007a that have been useful to the author.

A.1 CO_2 Laser

To turn on the CO_2 laser:

1. Turn on CO_2 chiller unit. Ensure that temperature is set to 19 C.

2. On laser panel, turn on panel power and laser power switches. Ensure that laser shutter switch is in "CLOSED" position.

3. Turn laser key to first position. This warms the laser up, but does not allow the shutter to open. Fault light will initially turn on, but should turn off and ready light will turn on. If fault stays lit, turn key to"OFF" position, wait a few seconds, and try again.

4. When ready to use laser, turn key to second position. Shutter can now be opened by shutter switch on main panel. If using for a lattice, leave shutter open for 10-20 minutes before using to allow pointing to stabilize.

A.2 Double Pass AOM

To set up a frequency-jump double-pass AOM:

1. A polarizing beam-splitter (PBS) cube should be placed before the double-pass setup, and a quarter-wave plate after the AOM so that the returned beam can be spearated from the input.

2. Align the first pass through the AOM for maximum efficiency in the desired order. On the Rb_2 table, this is the -1 order. This alignment should be done at a frequency halfway between the two extremes where the AOM will be operating. For example, on the Rb_2 table the AOM jumps from 62 MHz to 90 MHz, so the alignment is done at 76 MHz.

3. Perform this step at the lower frequency step (62 MHz). Place a collimating lens at its own focal length beyond the AOM. The purpose of this lens is to make the beams at both frequency extremes be parallel so they will follow nearly the same path after the double pass.

   This lens should be mounted on a micrometer-driven translation stage and very carefully positioned in the transverse beam direction. Specifically, the stage should be placed so that the beam is in the same place as before the lens was installed, *and* it does not shift when the stage is translated. This is *very* important for later steps. The position of the lens along the beam axis is not important at this stage.

   An iris should be used to block all but the correct order, but should be loose enough to allow the beam from both frequency extremes to pass through. If both of these requirements aren't possible, ensure that both beams will

pass and ignore any extra orders present. This iris should be located just before the lens focus, which is where the retroreflecting mirror will be.

4. Install the retroreflecting mirror and optimize the efficiency in the correct (-1) order. This should once again be done at the middle frequency (76 MHz). The mirror must be placed at the focus of the lens. This placement ensures that the diffracted orders are well-separated and that the reflected beams are recollimated on the second pass.

   At the output of the double-pass, a second iris should block all but the correct order. This iris can be made quite tight around the desired order, as the beam pointing should not change here. This may have to be left somewhat loose until after the next step, however.

5. Send the beam to the slave laser, but remove the last mirror and allow the beam to propagate 3–4 meters. Blink the frequency between the two extremes (62 MHz to 90 MHz), and scan the lens' longitudinal position so as to minimize the shift in beam position. This process ensures that the beams at both frequencies are parallel after passing through the lens and will follow the same path after being double-passed.

   This is the most critical step of the alignment, and the beam pointing should change by less than 1/4 of a beam diameter, preferably less than 1/10 of a beam diameter. In any case, beam shift should be absolutely minimized so that injection alignment will be maintained after the frequency shift.

   After this step, AOM alignment should *not* be altered, as it will affect the lens alignment. Adjusting the retroreflecting mirror is still acceptable.

6. Finally, perform an injection alignment *at the center frequency*. This should

be done only with mirrors outside of the double-pass setup.

A.3 Faraday Isolator

To align the beam cubes and crystal (to set the correct wavelength) in Faraday isolators:

1. Remove the output PBS (polarizing beam splitter). Adjusting the input PBS, optimize its angle for maximum transmission in the forward direction for the laser it is being used with. If necessary, a half-wave plate can be used later to match polarizations precisely. Mark the position of the plate with a pencil so that it can be repositioned easily.

2. Removing the input PBS, move the rotator crystal to the other side of the isolator using a small, non-scratching object to push the edge of its holder. A pen cap works nicely. Re-attach the input PBS in its original position.

3. Using a polarizer on a rotation stage, find the beam's polarization angle. Tilt the polarizer by 45 degrees to mimic the output PBS. If you don't know the relative angle of the output PBS, you may accidentally choose the wrong direction. This can be corrected when you note that isolation is not achieved.

4. Insert the isolator in reverse direction (with the rotated external polarizer before it in the beam path) and measure the power transmission. Move the crystal inward, in small steps, so as to minimize the transmission. This will likely take several attempts, as the crystal can only be pushed in one direction.

5. Reattach the output PBS at approximately the right angle, but leave loose enough to rotate. Remove the external polarizer. Rotate the output PBS to minimize transmission. Typical extinction values are -25 to -30 dB. Mark the angular position of the PBS as a reference.

6. Tighten all screws and insert the isolator into the beam path in the forward direction. If you have not already done so, mark the forward direction on the casing.

A.4 Slave Diode Injection Lock

To injection-lock a slave laser:

1. Prepare an injection beam with the proper polarization to pass through the optical isolator in front of the slave. This beam should have a power of ~ 0.5 mW - 1 mW, but *absolutely not more than* 1 mW.

2. Ensure that the slave diode is not naturally lasing too close to the injection beam frequency ($\lesssim 1$ nm or 15 cm^{-1}). This near-match in frequency will make it difficult to determine if the injection lock is working, and may cause the cavity mode to fight the injected beam mode. Temperature tuning will shift the natural lasing frequency.

3. Coarsely align the injection beam to the optical isolator in front of the slave. This is most easily done by aligning it to overlap the beam path from the small amount of light that escapes the optical isolator at the wrong polarization when the slave laser is at full power.

4. With the injected beam blocked, turn the slave laser current down to the lasing threshold. This is the point at which a small increase in current will

give a large increase in light output. For the slave on the Rb_2 table, this is 80 microwatts at 32.1 mA of current. Monitor the output power after the Faraday isolator with a power meter while tuning the current to reach the lasing threshold.

5. Lock the master laser and unblock the injection beam. The power output should increase slightly. Walking two mirrors before the slave laser, optimize the slave laser power. When the alignment is optimized, the output power should have increased by a factor of 10. This gain factor could be as high as 20, but must be at least 5. The output power will generally be significantly lower if the master laser is unlocked.

6. The success of the lock at full power can be determined by sending a pickoff of the output beam onto a diffraction grating and monitoring the diffracted beam with a camera. The beam position will jump when lock is achieved. Typically there are many currents that will achieve lock, spaced $\sim$ 15 – 20 mA apart. To achieve a pure output beam, increase the current until the diffracted beam jumps, and then slightly reduce the current to eliminate as much of the unwanted mode as possible.

A.5 Locking Diode Lasers

To lock diode lasers:

1. Raise diode current to operating level (approx. 100 mA or 1 V as measured across the 10 ohm resistor through the panel). Turn on the photodiode and allow the laser to thermally stabilize for 15-20 min. Turn on the PZT controller.

2. Set an oscilloscope to measure 200 mV or 500 mV per division for the photodiode signal and 50 mV or 100 mV per division for the error signal. To lock well, the error signal should at least be large enough to fill half the vertical space on the scope at 50 mV per division. The time per division should be 5 ms.

3. Turn on the PZT scan. This allows the photodiode signal to show the shape of the absorption curve as the laser is scanned through.

4. Using a combination of the PZT and current controls, search for an absorption dip with the correct error signal for the laser. Note the level of the photodiode signal at the position you wish to lock to.

5. Offset the signal from the peak you will lock to. Turn off the scan. The photodiode and error signals will become (roughly) flat lines. Slowly scan the PZT so that the signal level reaches the position you noted above.

6. As you approach the desired position, observe the error signal. When it moves from the ground level, you have reached the peak. Engage the lock. If the laser did not lock correctly, repeat steps 5 and 6 again.

A.6 Making a MOT

To trap atoms in a MOT:

1. Turn on the cooling water for the magnetic field coils, and then turn on the coils themselves. For the Rb table, the voltage measured across the 0.1 ohm parallel resistors should be approximately 0.5 V (corresponding to 5 A) for the bottom coil, and 0.6 V (6 A) for the top coil. The top coil may need

to be tuned to match the bottom coil by centering the MOT on the Hitachi camera, viewed with the Matrox Intellicam program. For the KRb table, the current supply should read 12 V and just over 3 A

2. Turn on the appropriate getter's Variac. The Variac should not be higher than 20 V (AC), and the current should be set to approximately 3.3 A.

3. Ensure that all necessary AOMs are turned on. For the Rb table, ensure that the Control.vi program has been initialized.

4. For Rb, lock both the trap and repump lasers. For K, there is only one master laser to lock.

5. Turn on the (Rb) slave or (K) tapered amplifier. The TA will automotically match the injected frequency. The Rb slave laser must be current-tuned to match its injection seed. Do this by monitoring the position of the beam when reflected from a grating. It will shift positions when locked to the injection seed. For the Rb table, the slave laser current should be 119 mA.

6. The MOT should be visible on a monitor screen. If not, try relocking the lasers and ensure the slave laser is properly set.

A.7 Rubidium Experiment Shutdown

To turn off Rb_2 setup:

1. Turn off CO_2 laser, using reverse of its turn-on procedure.

2. Turn of slave laser current supply. As there is a slow turn-on circuit to prevent overloads, it is not necessary to turn the current down first. Trap

and repump master lasers are typically left on. If they are turned off, their current controllers must be turned down to zero.

3. Unlock both master lasers and turn off the PZT driver. Shut off the oscilloscope.

4. Turn down magnet coil voltage to 20 V, let thermally stabilize for 5 - 10 minutes, then shut off supply. Turn off magnet coil cooling water. This staged shutdown reduces thermal stress that can affect the short in the upper magnet coil, which can cause the MOT to fluctuate when running and ultimately require a coil replacement.

5. Leave getter current fixed, use switch to turn off the Variac.

6. Shut off both photodiodes on the upper table.

7. Shut off camera monitors and oscilloscopes.

8. Shut off electric grid and plate/ ETP high voltage supplies (2), along with the boxcar and SRS amplifier.

9. Shut off any external lasers, such as the ND6000 or Ti:Sapphire.

A.8 Titanium Sapphire Lasers

To Start Ti:Sapphire (Coherent 899-29):

0. Turn on warning light outside door.

1. Turn on cooling water to laser power supply, turn on chiller unit to cool sapphire crystal.

2. Place high-power meter in front of Ti:Sapph

3. Turn lock key on power supply and hit "on" button. After tube startup, raise current to 45 A for I-200 or 38 A for I-400.

4. Ensure that Ti:Sapph output is maximized (should be in vicinity of 1 W). Try to minimize adjustments, as this may misalign the wavemeter.

5. On analog control box, set Display to "External", Operating Mode to "Lock", Thin Etalon knob to detent at left, and Scan Control to "External".

6. Turn on computer. Go to folder "Laser1" (or other number as appropriate) and run program "as", which stands for "AutoScan".

7. Initialize laser (F1). Go to wavemeter utilities (F6) and run a continuous scan (F8). The "Difference" column should be less than 0.1 GHz between any two readings. If it is not, turn a wavemeter tilt knob a quarter turn and rescan. If that doesn't work, try a quarter turn in the opposite direction. If you cannot get the wavemeter aligned in this way, see the Autoscan manual and follow the alignment instructions there.

A.9 Important Numbers and Other Information for the Rb_2 Apparatus

These are some important numbers and other useful information for the Rb_2 apparatus.

1.
   - Good MOT density: up to $1 \times 10^{11}\,\mathrm{cm}^{-3}$, but more than $3 \times 10^{10}\,\mathrm{cm}^{-3}$
   - Good atom number: up to 1×10^{8}, but more than 1×10^{7}

2.
   - Trap beam power: 30 mW, more than 27 mW OK
   - Repump: 4 mW, more than 3 mW OK
   - Probe beam: between 80 μW and 120 μW - more causes saturation, less causes noise
   - Slave injection power: usually over 0.5 mW, more than 1 mW can shorten life of or kill slave diode

3.
   - Slave diode temp: 199.3 kΩ
   - Slave diode current: 128.9 mA
   - Trap laser temp: 3.430 kΩ
   - Trap laser current: 90 mA
   - Repump laser temp: 3.330 kΩ
   - Repump laser current: 106 mA

4. The home-built microcontroller for the trap and repump ECDL temperature controller can sometimes lock or show gibberish on the screen. Jen Carini reports similar errors in microcontrollers due to static buildup on the circuit card. To fix this, first try turning the box off and back on. If that does not work, turn the box off, remove the power cable, switch the power on for $\sim$ 15 seconds and back off, plug the power cable in, and restart the box. This seems to discharge the static buildup.

5. Getter current: 3.1 A: if fresh, as low as 2.5 A, when used, about 5.5 A

6.
   - Ti:S pump power: 10.50 W by Verdi, or 15-16 W by Argon ion
   - Ti:S output power: up to 2 W single-mode, 1.5 W more typical, over 1 W acceptable

7.
   - Autoscan data segments: 10 GHz
   - Scan time: up to 1200 s per 10 GHz segment, usually $\geq$ 500 s for data collection
   - Averages ("protocol"): 5 minimum, 50 typical; more than $\sim$ 200 averages between all channels slows scan time, allowing slower scans

8. Rb_2 Camera: switches outside for video, inside for stills

Thin Etalon (R17)	BRF (R24)
VET1 (R31)	VET2 (R38)
OAM2 (R45)	OAM1 (R52)

Table A.1: A list of the potentiometers in the Autoscan interface box. They are shown in their relative positions on the printed circuit board (PCB). The collection on potentiometers is along the left side of the PCB.

9. The Ti:S Autoscan internal sensor channels have limited dynamic range, and their sensitivity often needs to be adjusted by turning potentiometers in the Autoscan interface box. These potentiometers turn counter-clockwise (CCW) to increase the measured signal, and clockwise (CW) to reduce it. The layout of the potentiometers in the box is shown in Table A.1. More detail on setting proper signal levels can be found in Chapter 6 on pp. 9-12 of the Autoscan manual.

Appendix B

Energy Levels and Franck-Condon Factors

This Appendix contains tables of energy levels and some rotational constants from the $X\,^1\Sigma_g^+$ state, the $a\,^3\Sigma_u^+$ state, and the $1\,^3\Pi_{g,\,\Omega=1}$ state. Both the X state and a state potentials are from Ref. [29], and the $1\,^3\Pi_{g,\,\Omega=1}$ state is from Ref. [39]. The eigenstates were calculated using LEVEL 8.0 [31]. It also includes Franck-Condon factors from the $a\,^3\Sigma_u^+$ state to the inner and outer wells of the $7p\ ^3\Sigma_g^+$ state, with the upper state potential from Ref. [73]. These FCFs were calculated using LEVEL 8.2 [32], as version 8.0 had difficulty with the double-well structure of the potential.

B.1 Energy Levels and Rotational Constants

Table B.1: The energy levels and rotational constants of the $X\,^1\Sigma_g^+$ state.

v'	***J'***	**E**	**Bv**	**-Dv**
0	0	-3964.7445	0.022375369	-1.3510534E-08
1	0	-3907.2364	0.022319032	-1.3595723E-08
2	0	-3850.0101	0.022262131	-1.3681588E-08
3	0	-3793.0671	0.022204649	-1.3768120E-08

Continued on next page...

v'	*J'*	**E**	**Bv**	**-Dv**
4	0	-3736.4085	0.022146573	-1.3855321E-08
5	0	-3680.0357	0.022087887	-1.3943200E-08
6	0	-3623.9501	0.022028575	-1.4031770E-08
7	0	-3568.1529	0.021968624	-1.4121054E-08
8	0	-3512.6457	0.021908016	-1.4211081E-08
9	0	-3457.4298	0.021846736	-1.4301869E-08
10	0	-3402.5069	0.021784768	-1.4393499E-08
11	0	-3347.8785	0.021722096	-1.4485918E-08
12	0	-3293.5462	0.021658702	-1.4579244E-08
13	0	-3239.5118	0.021594574	-1.4673734E-08
14	0	-3185.7769	0.021529686	-1.4768480E-08
15	0	-3132.3432	0.021464028	-1.4865612E-08
16	0	-3079.2128	0.021397583	-1.4962160E-08
17	0	-3026.3875	0.021330322	-1.5061416E-08
18	0	-2973.8693	0.02126224	-1.5160697E-08
19	0	-2921.6601	0.02119331	-1.5262416E-08
20	0	-2869.7621	0.021123513	-1.5364122E-08
21	0	-2818.1775	0.021052832	-1.5468633E-08
22	0	-2766.9085	0.020981239	-1.5573787E-08
23	0	-2715.9573	0.020908729	-1.5681003E-08
24	0	-2665.3264	0.02083526	-1.5789835E-08
25	0	-2615.0183	0.020760826	-1.5899830E-08
26	0	-2565.0353	0.020685394	-1.6012924E-08
27	0	-2515.3802	0.020608946	-1.6126971E-08
28	0	-2466.0555	0.020531464	-1.6244038E-08
29	0	-2417.064	0.02045291	-1.6362868E-08
30	0	-2368.4086	0.020373273	-1.6483547E-08
31	0	-2320.0921	0.020292514	-1.6607730E-08

Continued on next page...

v'	*J'*	**E**	**Bv**	**-Dv**
32	0	-2272.1176	0.020210612	-1.6733602E-08
33	0	-2224.488	0.020127547	-1.6863305E-08
34	0	-2177.2067	0.020043281	-1.6995884E-08
35	0	-2130.2768	0.019957796	-1.7130869E-08
36	0	-2083.7017	0.019871054	-1.7270036E-08
37	0	-2037.4848	0.019783024	-1.7411475E-08
38	0	-1991.6297	0.01969368	-1.7557143E-08
39	0	-1946.1399	0.01960298	-1.7707146E-08
40	0	-1901.0192	0.019510901	-1.7860581E-08
41	0	-1856.2714	0.019417409	-1.8019719E-08
42	0	-1811.9006	0.019322461	-1.8182636E-08
43	0	-1767.9106	0.019226033	-1.8350380E-08
44	0	-1724.3057	0.019128073	-1.8523690E-08
45	0	-1681.0902	0.019028547	-1.8701045E-08
46	0	-1638.2683	0.018927416	-1.8885157E-08
47	0	-1595.8446	0.018824629	-1.9074822E-08
48	0	-1553.8237	0.018720156	-1.9270882E-08
49	0	-1512.2103	0.018613941	-1.9474923E-08
50	0	-1471.0092	0.018505946	-1.9685080E-08
51	0	-1430.2255	0.018396124	-1.9904013E-08
52	0	-1389.8642	0.018284417	-2.0130403E-08
53	0	-1349.9306	0.018170784	-2.0364794E-08
54	0	-1310.43	0.018055159	-2.0608855E-08
55	0	-1271.3681	0.01793749	-2.0860796E-08
56	0	-1232.7503	0.01781772	-2.1123860E-08
57	0	-1194.5825	0.017695779	-2.1396624E-08
58	0	-1156.8706	0.017571616	-2.1680841E-08
59	0	-1119.6208	0.017445153	-2.1977644E-08

Continued on next page...

v'	*J'*	**E**	**Bv**	**-Dv**
60	0	-1082.8392	0.017316333	-2.2286159E-08
61	0	-1046.5322	0.017185079	-2.2609676E-08
62	0	-1010.7064	0.017051318	-2.2946032E-08
63	0	-975.3684	0.016914977	-2.3298733E-08
64	0	-940.5253	0.016775967	-2.3666577E-08
65	0	-906.1839	0.016634214	-2.4051646E-08
66	0	-872.3515	0.016489618	-2.4454712E-08
67	0	-839.0355	0.016342097	-2.4876113E-08
68	0	-806.2433	0.016191544	-2.5318831E-08
69	0	-773.9828	0.016037867	-2.5781989E-08
70	0	-742.2617	0.015880956	-2.6269688E-08
71	0	-711.0882	0.015720704	-2.6780495E-08
72	0	-680.4705	0.015556994	-2.7319486E-08
73	0	-650.4169	0.015389709	-2.7885381E-08
74	0	-620.9362	0.015218723	-2.8483350E-08
75	0	-592.0369	0.015043907	-2.9112133E-08
76	0	-563.7281	0.014865123	-2.9777434E-08
77	0	-536.0189	0.014682229	-3.0478658E-08
78	0	-508.9184	0.014495073	-3.1221720E-08
79	0	-482.4361	0.014303503	-3.2006406E-08
80	0	-456.5816	0.014107349	-3.2838727E-08
81	0	-431.3645	0.013906446	-3.3720155E-08
82	0	-406.7946	0.013700606	-3.4656153E-08
83	0	-382.882	0.013489649	-3.5650599E-08
84	0	-359.6364	0.013273371	-3.6707421E-08
85	0	-337.0682	0.013051573	-3.7833942E-08
86	0	-315.1873	0.012824038	-3.9033562E-08
87	0	-294.0038	0.012590541	-4.0315363E-08

Continued on next page...

v'	*J'*	**E**	**Bv**	**-Dv**
88	0	-273.528	0.012350856	-4.1685180E-08
89	0	-253.7697	0.012104738	-4.3150724E-08
90	0	-234.739	0.011851941	-4.4722773E-08
91	0	-216.4454	0.011592213	-4.6409380E-08
92	0	-198.8984	0.011325291	-4.8222419E-08
93	0	-182.1071	0.011050916	-5.0175206E-08
94	0	-166.0801	0.010768827	-5.2279779E-08
95	0	-150.8253	0.010478768	-5.4551526E-08
96	0	-136.3498	0.010180497	-5.7008151E-08
97	0	-122.66	0.00987379	-5.9667296E-08
98	0	-109.7607	0.009558453	-6.2548795E-08
99	0	-97.6556	0.009234332	-6.5675995E-08
100	0	-86.3464	0.00890133	-6.9074667E-08
101	0	-75.8327	0.008559419	-7.2773133E-08
102	0	-66.1117	0.008208658	-7.6803614E-08
103	0	-57.1777	0.007849217	-8.1202694E-08
104	0	-49.0215	0.007481409	-8.6009931E-08
105	0	-41.6301	0.007105734	-9.1266024E-08
106	0	-34.9863	0.006722928	-9.7013031E-08
107	0	-29.0676	0.006334088	-1.0321189E-07
108	0	-23.8449	0.005943058	-1.0806798E-07
109	0	-19.2644	0.005573585	-1.0276303E-07
110	0	-15.215	0.005240193	-1.1674016E-07
111	0	-11.7566	0.004728007	-1.9616683E-07
112	0	-9.0455	0.004328429	-1.0151755E-07
113	0	-6.7381	0.003893645	-1.8208502E-07
114	0	-4.8917	0.00355548	-2.0854307E-07
115	0	-3.4328	0.003168073	-1.7761597E-07

Continued on next page...

v'	*J'*	**E**	**Bv**	**-Dv**
116	0	-2.2957	0.002763506	-1.9501524E-07
117	0	-1.4429	0.002371935	-2.4792394E-07
118	0	-0.8351	0.00198916	-3.1633869E-07
119	0	-0.4294	0.001607659	-4.0774390E-07
120	0	-0.1835	0.001223749	-5.5521894E-07
121	0	-0.0562	0.000835442	-8.5490916E-07
122	0	-0.0078	0.000439644	-1.7844496E-06

Table B.2: The energy levels and rotational constants of the $a\,^3\Sigma_u^+$ state.

v'	*J'*	**E**	**Bv**	**-Dv**
0	0	-234.7328	0.010614577	-2.6636798E-08
1	0	-221.467	0.010458946	-2.7407541E-08
2	0	-208.5776	0.010301568	-2.8256593E-08
3	0	-196.0664	0.010142217	-2.9179637E-08
4	0	-183.9348	0.009980571	-3.0189773E-08
5	0	-172.1847	0.009816339	-3.1289530E-08
6	0	-160.8177	0.009649277	-3.2481570E-08
7	0	-149.8356	0.009479106	-3.3776310E-08
8	0	-139.2401	0.009305544	-3.5180944E-08
9	0	-129.033	0.009128306	-3.6707495E-08
10	0	-119.216	0.008947054	-3.8367716E-08
11	0	-109.7909	0.008761526	-4.0167492E-08
12	0	-100.7593	0.008571369	-4.2146817E-08
13	0	-92.1231	0.008376232	-4.4290536E-08

Continued on next page...

v'	***J'***	**E**	**Bv**	**-Dv**
14	0	-83.8838	0.008175811	-4.6643002E-08
15	0	-76.0429	0.007969598	-4.9225435E-08
16	0	-68.6019	0.007757325	-5.2075126E-08
17	0	-61.5619	0.007538529	-5.5245519E-08
18	0	-54.9241	0.007312813	-5.8744232E-08
19	0	-48.6893	0.007079652	-6.2631046E-08
20	0	-42.8577	0.006838575	-6.6973037E-08
21	0	-37.4291	0.006589088	-7.1861319E-08
22	0	-32.4029	0.006330709	-7.7385331E-08
23	0	-27.7774	0.00606294	-8.3647807E-08
24	0	-23.5501	0.005785228	-9.0799490E-08
25	0	-19.7174	0.005497039	-9.9016156E-08
26	0	-16.2743	0.005197992	-1.0845244E-07
27	0	-13.2136	0.004887827	-1.1951406E-07
28	0	-10.5267	0.004565516	-1.3278008E-07
29	0	-8.2028	0.004231808	-1.4769493E-07
30	0	-6.2265	0.003887097	-1.6612009E-07
31	0	-4.58	0.003531871	-1.8805220E-07
32	0	-3.2416	0.003166637	-2.1516881E-07
33	0	-2.1862	0.002792692	-2.4970131E-07
34	0	-1.3851	0.002411377	-2.9508024E-07
35	0	-0.80647527	2.0240401E-03	-3.5786698E-07
36	0	-0.41606314	1.6319448E-03	-4.5154545E-07
37	0	-0.17765279	1.2360458E-03	-6.0790181E-07
38	0	-0.05395207	8.3670033E-04	-9.2367295E-07
39	0	-0.00723808	4.3251356E-04	-1.9028534E-06

Table B.3: The energy levels of the $1^3\Pi_{g,\,\Omega=1}$ state.

v'	**E(v') (cm^{-1})**
0	13060.3277
1	13088.764
2	13116.2008
3	13142.5345
4	13167.6379
5	13191.3585
6	13213.4878
7	13233.6905
8	13251.3289

B.2 Franck-Condon Factors

Table B.4: Franck-Condon Factors from the $a\,^3\Sigma_u^+$ state to the inner well of the $7p\,^3\Sigma_g^+$ state. Here, v' is the vibrational quantum number for the full potential, and v' (inner) is the numbering for the inner well alone.

v'	**v' (inner)**	**E(v') (cm^{-1})**	**FCF v" = 35**	**FCF v" = 36**
0	0	23650.1503	–	–
1	1	23690.77	0.0018	0.00116
2	2	23731.29	0.00124	7.90E-04
3	3	23771.62	7.84E-05	4.67E-05
4	4	23811.77	3.80E-04	2.52E-04
5	5	23851.8	9.47E-04	6.09E-04

Continued on next page...

v'	**v' (inner)**	**E(v') (cm^{-1})**	**FCF v" = 35**	**FCF v" = 36**
6	6	23891.69	3.46E-04	2.15E-04
7	7	23931.44	3.99E-05	2.90E-05
8	8	23971.04	6.19E-04	4.04E-04
9	9	24010.51	5.73E-04	3.62E-04
10	10	24049.87	3.00E-05	1.63E-05
11	11	24089.11	2.59E-04	1.74E-04
12	12	24128.24	6.35E-04	4.09E-04
13	13	24167.26	2.63E-04	1.61E-04
14	14	24206.18	1.36E-05	1.13E-05
15	15	24244.98	4.16E-04	2.75E-04
16	16	24283.67	5.26E-04	3.34E-04
17	17	24322.26	1.07E-04	6.26E-05
18	18	24360.74	7.27E-05	5.25E-05
19	19	24399.11	4.63E-04	3.04E-04
20	20	24437.37	4.36E-04	2.74E-04
21	21	24475.52	5.70E-05	3.15E-05
22	22	24513.55	9.96E-05	7.10E-05
23	23	24551.45	4.54E-04	2.97E-04
24	24	24589.24	4.05E-04	2.53E-04
25	25	24626.89	5.68E-05	3.10E-05
26	26	24664.41	8.19E-05	5.96E-05
27	27	24701.8	4.16E-04	2.74E-04
28	28	24739.04	4.22E-04	2.65E-04
29	29	24776.15	9.34E-05	5.28E-05
30	30	24813.11	3.83E-05	3.01E-05
31	31	24849.92	3.48E-04	2.32E-04
32	32	24886.59	4.59E-04	2.91E-04
33	33	24923.1	1.76E-04	1.03E-04

Continued on next page...

v'	**v' (inner)**	**E(v') (cm^{-1})**	**FCF v" = 35**	**FCF v" = 36**
34	34	24959.47	2.23E-06	3.18E-06
35	35	24995.68	2.38E-04	1.63E-04
36	36	25031.75	4.71E-04	3.04E-04
37	37	25067.66	3.05E-04	1.86E-04
38	38	25103.42	2.42E-05	1.11E-05
39	39	25139.02	9.81E-05	7.24E-05
40	40	25174.48	4.02E-04	2.67E-04
41	41	25209.79	4.40E-04	2.76E-04
42	42	25244.95	1.54E-04	8.81E-05
43	43	25279.96	2.77E-06	4.07E-06
44	44	25314.82	2.24E-04	1.56E-04
45	45	25349.52	4.72E-04	3.06E-04
46	46	25384.07	3.66E-04	2.24E-04
47	47	25418.47	7.18E-05	3.73E-05
48	48	25452.71	3.26E-05	2.81E-05
49	49	25486.81	3.07E-04	2.10E-04
50	50	25520.76	4.92E-04	3.16E-04
51	51	25554.55	3.22E-04	1.94E-04
52	52	25588.2	4.40E-05	2.07E-05
53	53	25621.69	5.28E-05	4.34E-05
54	54	25655.03	3.37E-04	2.30E-04
55	55	25688.22	5.05E-04	3.23E-04
56	56	25721.25	3.29E-04	1.97E-04
57	57	25754.14	5.05E-05	2.37E-05
58	58	25786.87	4.28E-05	3.71E-05
59	59	25819.44	3.18E-04	2.20E-04
60	60	25851.87	5.19E-04	3.35E-04
61	61	25884.14	3.89E-04	2.34E-04

Continued on next page...

v'	**v' (inner)**	**E(v') (cm^{-1})**	**FCF v" = 35**	**FCF v" = 36**
62	62	25916.25	9.56E-05	4.86E-05
63	63	25948.21	1.25E-05	1.43E-05
64	64	25980.01	2.46E-04	1.76E-04
65	65	26011.66	5.11E-04	3.36E-04
66	66	26043.14	4.85E-04	2.99E-04
67	67	26074.47	2.03E-04	1.12E-04
68	68	26105.65	3.22E-06	1.52E-07
69	69	26136.66	1.27E-04	9.92E-05
70	70	26167.51	4.33E-04	2.95E-04
71	71	26198.2	5.70E-04	3.62E-04
72	72	26228.72	3.81E-04	2.24E-04
73	73	26259.08	8.32E-05	3.89E-05
74	74	26289.28	1.69E-05	1.97E-05
75	75	26319.31	2.62E-04	1.92E-04
76	76	26349.17	5.52E-04	3.67E-04
77	77	26378.86	5.71E-04	3.54E-04
78	78	26408.38	2.98E-04	1.67E-04
79	79	26437.73	3.07E-05	1.02E-05
80	80	26466.91	6.20E-05	5.68E-05
81	81	26495.91	3.67E-04	2.62E-04
82	82	26524.74	6.29E-04	4.12E-04
83	83	26553.39	5.75E-04	3.50E-04
84	84	26581.86	2.61E-04	1.40E-04
85	85	26610.14	1.39E-05	2.43E-06
86	86	26638.24	9.77E-05	8.56E-05
87	87	26666.15	4.38E-04	3.11E-04
88	88	26693.88	6.96E-04	4.53E-04
89	89	26721.41	6.10E-04	3.66E-04

Continued on next page...

v'	v' (inner)	E(v') (cm^{-1})	FCF v" = 35	FCF v" = 36
90	90	26748.75	2.65E-04	1.38E-04
91	91	26775.9	1.10E-05	1.10E-06
92	92	26802.84	1.15E-04	1.02E-04
93	93	26829.57	4.90E-04	3.50E-04
94	94	26856.1	7.71E-04	5.02E-04
95	95	26882.42	6.78E-04	4.05E-04
96	96	26908.53	2.99E-04	1.53E-04
97	97	26934.42	1.38E-05	1.27E-06
98	98	26960.09	1.24E-04	1.13E-04
99	99	26985.54	5.44E-04	3.92E-04
100	100	27010.75	8.69E-04	5.67E-04
101	101	27035.73	7.73E-04	4.59E-04
102	102	27060.47	3.43E-04	1.72E-04
103	103	27084.97	1.56E-05	1.05E-06
104	104	27109.22	1.47E-04	1.37E-04
105	105	27133.22	6.39E-04	4.63E-04
106	106	27156.96	0.00101	6.57E-04
107	107	27180.44	8.77E-04	5.13E-04
108	108	27203.64	3.60E-04	1.72E-04
109	109	27226.57	6.47E-06	2.48E-07
110	110	27249.21	2.32E-04	2.09E-04
111	111	27271.56	8.53E-04	6.10E-04
112	112	27293.61	0.00123	7.80E-04
113	113	27315.34	9.28E-04	5.19E-04
114	114	27336.75	2.64E-04	1.06E-04
115	115	27357.83	1.42E-05	3.67E-05
116	116	27378.57	5.55E-04	4.52E-04
117	117	27398.95	0.00134	9.09E-04

Continued on next page...

v'	**v' (inner)**	**E(v') (cm^{-1})**	**FCF v" = 35**	**FCF v" = 36**
118	118	27418.96	0.00143	8.51E-04
119	119	27438.59	6.66E-04	3.15E-04
120	120	27457.8	1.19E-05	9.95E-07
121	121	27476.57	4.79E-04	4.30E-04
122	122	27494.89	0.00163	0.00113
123	123	27512.72	0.00186	0.0011
124	124	27530.04	7.12E-04	3.04E-04
125	125	27546.82	1.92E-05	6.89E-05
126	126	27563.03	0.00133	0.00105
127	127	27578.65	0.00269	0.00169
128	128	27593.66	0.00145	6.73E-04
129	129	27608.05	3.14E-06	5.96E-05
130	130	27621.82	0.00205	0.00161
131	131	27634.95	0.00376	0.00223
132	132	27647.49	0.00108	3.61E-04
133	133	27659.45	6.01E-04	7.51E-04
134	134	27670.83	0.00467	0.00319
135	135	27681.68	0.00371	0.00175
136	136	27692.06	1.19E-05	7.09E-05
137	137	27701.95	0.00377	0.00313
138	138	27711.41	0.00686	0.00389
139	139	27720.49	0.00189	4.63E-04
143	140	27729.21	8.21E-04	0.00136
146	141	27737.64	0.00703	0.00518
150	142	27745.8	0.00789	0.00393
153	143	27753.71	0.00196	3.05E-04
157	144	27761.42	4.81E-04	0.00132
160	145	27768.92	0.00595	0.00522

Continued on next page...

v'	v' (inner)	E(v') (cm^{-1})	FCF v" = 35	FCF v" = 36
164	146	27776.26	0.00992	0.00588
167	147	27783.45	0.0072	0.00268
171	148	27790.5	0.00181	9.52E-05
175	149	27797.42	1.30E-04	0.00117
178	150	27804.22	0.00372	0.00456
182	151	27810.9	0.00888	0.00676
186	152	27817.49	0.0111	0.0059
190	153	27823.96	0.00895	0.00297
195	154	27830.3	0.00417	4.10E-04
200	155	27836.52	4.47E-04	3.67E-04
205	156	27842.6	8.03E-04	0.00319
211	157	27848.53	0.00577	0.00717
219	158	27854.28	0.0131	0.00961

Table B.5: Franck-Condon Factors from the $a\,^3\Sigma_u^+$ state to the outer well of the $7p\,^3\Sigma_g^+$ state. Here, v' is the vibrational quantum number for the full potential, and v' (outer) is the numbering for the outer well alone.

v'	v' (outer)	E(v') (cm^{-1})	FCF v" = 35	FCF v" = 36
140	0	27721.84	0.0438	0.387
141	1	27725.27	0.0136	0.00485
142	2	27728.65	0.0315	0.14
144	3	27732.03	0.0202	0.00432
145	4	27735.35	0.0309	0.0716
147	5	27738.66	0.0243	0.0023
148	6	27741.9	0.0308	0.038

Continued on next page...

v'	**v' (outer)**	**E(v') (cm^{-1})**	**FCF v" = 35**	**FCF v" = 36**
149	7	27745.13	0.0266	7.78E-04
151	8	27748.32	0.0309	0.0188
152	9	27751.48	0.0278	5.23E-05
154	10	27754.59	0.0299	0.00819
155	11	27757.67	0.0272	1.63E-04
156	12	27760.72	0.028	0.00269
158	13	27763.73	0.0258	9.42E-04
159	14	27766.73	0.0258	3.59E-04
161	15	27769.67	0.0242	0.00215
162	16	27772.57	0.0236	4.51E-05
163	17	27775.44	0.0217	0.00354
165	18	27778.28	0.0206	8.06E-04
166	19	27781.07	0.0186	0.00492
168	20	27783.83	0.0174	0.00206
169	21	27786.54	0.0156	0.00615
170	22	27789.21	0.0144	0.00345
172	23	27791.83	0.0126	0.00709
173	24	27794.42	0.0113	0.00465
174	25	27796.98	0.00971	0.0076
176	26	27799.48	0.00831	0.00534
177	27	27801.94	0.00703	0.00769
179	28	27804.36	0.00583	0.00577
180	29	27806.72	0.00469	0.00738
181	30	27809.04	0.00374	0.00579
183	31	27811.32	0.00284	0.00677
184	32	27813.56	0.00211	0.0054
185	33	27815.75	0.00146	0.0059
187	34	27817.88	9.60E-04	0.00471

Continued on next page...

v'	v' (outer)	E(v') (cm^{-1})	FCF v" = 35	FCF v" = 36
188	35	27819.96	5.67E-04	0.00488
189	36	27821.99	2.90E-04	0.00395
191	37	27824.01	1.03E-04	0.00387
192	38	27825.96	1.27E-05	0.00307
193	39	27827.85	7.87E-06	0.00282
194	40	27829.69	7.82E-05	0.0022
196	41	27831.47	2.15E-04	0.00195
197	42	27833.22	4.05E-04	0.00145
198	43	27834.89	6.28E-04	0.00118
199	44	27836.49	8.74E-04	8.32E-04
201	45	27838.03	0.00115	6.36E-04
202	46	27839.55	0.00145	4.12E-04
203	47	27840.99	0.00168	2.60E-04
204	48	27842.35	0.00197	1.39E-04
206	49	27843.67	0.00221	6.48E-05
207	50	27844.94	0.00246	1.68E-05
208	51	27846.15	0.00264	3.79E-07
209	52	27847.29	0.00279	7.79E-06
210	53	27848.34	0.00281	3.11E-05
212	54	27849.34	0.00292	6.98E-05
213	55	27850.28	0.00301	1.18E-04
214	56	27851.17	0.00291	1.64E-04
215	57	27851.97	0.00277	2.03E-04
216	58	27852.69	0.00263	2.38E-04
217	59	27853.35	0.00249	2.66E-04
218	60	27853.94	0.00236	2.89E-04
220	61	27854.49	0.00227	3.18E-04
221	62	27854.97	0.00192	2.95E-04

Continued on next page...

v'	**v' (outer)**	**E(v') (cm^{-1})**	**FCF v" = 35**	**FCF v" = 36**
222	63	27855.37	0.00171	2.84E-04
223	64	27855.75	0.00167	2.97E-04
224	65	27856.08	0.00138	2.60E-04
225	66	27856.35	0.00114	2.26E-04
226	67	27856.59	0.00107	2.20E-04
227	68	27856.76	6.56E-04	1.40E-04
228	69	27856.89	6.03E-04	1.31E-04
229	70	27857	4.57E-04	1.01E-04
230	71	27857.09	3.69E-04	8.30E-05
231	72	27857.15	2.82E-04	6.41E-05
232	73	27857.2	1.94E-04	4.44E-05

Appendix C

Simion Geometry File

This appendix contains the geometry file that models the Rb_2 MOT chamber. It includes the main body of the chamber, the time-of-flight arm and an opposite arm, the field plate and grid, the detector face, three dielectric support rods, and the mu metal shield. It also contains an electrode to simulate charge build-up on a vacuum chamber window.

C.1 Rb MOT 2.0 GEM File

```
;Rb-MOT
;original by Michaela Tscherneck 2002
;modified by Kilian Singer 7.3.2003
; and by Ed Eyler, 4/9/2003
; and by Ryan Carollo, 12/19/2011
;
;unlike noted in foreword read Chapter 2 of Handbook and Appendix J
;
;for those who are too lazy:
;
;important seting to prevent endless diskscanning:
;[main menu]
;       [adjust]
;               [other adjust]
;                       [scan on]->[scan off]
;load geometry file:
;[main menu]
;       [remove all PA from RAM]
;if you use geometry files
;       [new]
;               [use geometry file]
;                       select dir and press scan if directory shoud update
```

```
;                     load file by pressing left&right mouse button
;in case of errors:
;       [modify]
;              [geomf]
;                     [compile] to get error line and message
;
;if you don't want to use geometry files type in your dimensions
;       [new] and type in dimensions and symmetry
;       [modify]
;              [non electrode]->[electrode]
;              [bx] (eg.)
;              draw electrode to paint if [electrode] was selected or to
    delete [non electrode]
;              [replace]
;              ...
;              [keep]
;       [view] to view
;              [wb view tab]
;                     rightclick on number right to [Edg] to increase
    accuracy, left click decrease
;                     zoom with left mouse button area then press right mouse
    button to zoom
;                     unzoom right mouse button
;                                          click bar right to 3dmover to
    avoid view snapping
;                     drag area with left mouse butten then press [+Z3D] to
    intersect
;                     [-Z3d] to go back
;save fast adjust potential array
;       all potentials Voltages like 1,2,3,4,...,n
;       will be interpreted as variables
;       1.0001 is treated as static value
;       if you don't save it as fast adjust you won't be able to use this
    feature later on!!
;       therefore:
;[main menu]
;       [save]
;              type *.pa# as name (# to indicate that fast adjust pa shoud be
    used)
;              dont click into filename area place your mouse there
;       [refine]
;              [refine fast adjust array]
;attention if this is the firt time you use fast adjust on this geometry then
;       [fast]
;              set your potentials
;              [fast adjust potentials]
;now you can also use fast adjust in [view] in the [pa] tab!
;       [view]
;              [normal] tab
```

```
;                     [save iob] for all later sessions you can start here by
    clicking on [load iob] or
;[main menue] select empty pa
;       [view]
;               [pe view] to see potential array (caution in [wb view] tab [xy]
    [zy] [xz] must be selected)
;               [pas] tab [Fadj] to adjust potentials
;to define plane of potential
;               [wb view] and make intersections
;                       choose one of [xy] [zy] [xz]
;               switch back to [pe view]
;
;ion simulation:
;               [normal]-tab
;                       [def]
;                               [N=ions] type number of ions
;                               [first x]... [delta x]... fill in
;                       [group] if wanted
;                       [dots] & speed slider if wanted
;                       [fly em]
;                       [save iob] for all later sessions you can start here by
    clicking on [load iob] or



PA_Define(438,286,85,planar,none,electrostatic,100)

;MOT Chamber
Locate(142,142,42,1,0,0,0){
        Electrode(0.0001){
                Fill{
                        Within{Cylinder(0,0,40,78,78,80)}
                        Notin{Cylinder(0,0,38,76,76,76)}

                        ;opening for ETP arm
                        Locate(0,0,0,1,90,0,0){
                                Notin{Cylinder(0,0,140,23.7,23.7,276)}
                        }

                        ;opening for second arm
                        Locate(0,0,0,1,0,0,270){
                                Notin{Cylinder(0,0,140,23.7,23.7,276)}
                        }
                }

                ;MOT chamber arm for ETP
                Fill{
                        Locate(0,0,0,1,90,0,0){
                                Within{Cylinder(0,0,140,25.4,25.4,280)}
                                Notin{Cylinder(0,0,140,23.7,23.7,278)}
```

```
                }
                Notin{Cylinder(0,0,38,76,76,76)}
        }

        ;ETP detector flange
        Fill{
                Locate(140,0,0,1,90,0,0){
                        Within{Cylinder(0,0,152,25.4,25.4,152)}
                        Notin{Cylinder(0,0,150,23.7,23.7,152)}
                }
                Notin{Cylinder(0,0,38,76,76,76)}
        }

        ;second window arm
        Fill{
                Locate(0,0,0,1,0,0,270){
                        Within{Cylinder(0,0,140,25.4,25.4,280)}
                        Notin{Cylinder(0,0,140,23.7,23.7,280)}
                }
                Notin{Cylinder(0,0,38,76,76,76)}
        }
}

;ETP Detector
Electrode(1){
        Fill{
                Locate(182,0,0,1,90,0,0){
                        Within{Box3D(-3.5,-6,0,3.5,6,1.5)}
                }
        }
}

;Bare plate
Electrode(2) {
        Fill{
                Locate(-37,0,0,1,270,0,0) {
                        within{Cylinder(0,0,0,21,21,1.5)}
                }
        }
}

;Ring electrode for mesh grid
Electrode(3) {
        Fill{
                Locate(45,0,0,1,90,0,0) {
                        within{Cylinder(0,0,0,21,21,1.5)}
                        notin{Cylinder(0,0,0,11.5,11.5,1.5)}
                }
        }
}
```

```
;Mesh grid
Electrode(3) {
       Fill{
              Locate(45,0,0,1,90,0,0) {
                     within{Cylinder(0,0,0,11.5,11.5,0.1)}
              }
       }
}

;rod 1
Electrode(4){
       Fill{
              Locate(45,0,0,1,90,0,0){
                     Within{Cylinder(15.4,0,137,2.5,2.5,135)}
              }
       }
}

;rod 2
Electrode(5){
       Fill{
              Locate(45,0,0,1,90,0,0){
                     Within{Cylinder(-7.7,13.3,137,2.5,2.5,135)}
              }
       }
}

;rod 3
Electrode(6){
       Fill{
              Locate(45,0,0,1,90,0,0){
                     Within{Cylinder(-7.7,-13.3,137,2.5,2.5,135)}
              }
       }
}

;Mu-metal shielding tube
Electrode(7){
       Fill{
              Locate(182,0,0,1,90,0,0){
                     Within{Cylinder(0,0,80,23,23,140)}
                     Notin{Cylinder(0,0,80,21,21,140)}
              }
       }
}

;charged window
Electrode(8){
       Fill{
```

```
                        Locate(0,0,0,1,0,0,270){
                                Within{Cylinder(0,0,141,25,25,1)}
                        }
                }
        }
}
```

Appendix D

Automatic Spectra Alignment and Averaging

This appendix contains the code for a Mathematica program that automatically aligns and applies a linear stretch to multiple spectra to optimize alignment for averaging, as well as a command to average the different spectra together. If multiple cores are available, this code can run in parallel. A separate command attempts to improve the linearization of Autoscan data using a simultaneously-recorded VET trace. Section D.1 is the main program, and Section D.2 is a sample notebook to show the use of some of the functions. The main functions were written by Ryan Carollo, with the excellent file-reading and display utilities added by David Rahmlow.

D.1 Mathematica Data Analysis 0.1.3

```
(* ::Package:: *)

(**************************************************************************)
(* This file was generated automatically by the Mathematica front end. *)
(* It contains Initialization cells from a Notebook file, which  *)
(* typically will have the same name as this file except ending in *)
(* ".nb" instead of ".m".                                         *)
(*                                                                *)
(* This file is intended to be loaded into the Mathematica kernel using *)
(* the package loading commands Get or Needs. Doing so is equivalent *)
(* to using the Evaluate Initialization Cells menu command in the front *)
(* end.                                                           *)
(*                                                                *)
(* DO NOT EDIT THIS FILE. This entire file is regenerated         *)
```

```
(* automatically each time the parent Notebook file is saved in the *)
(* Mathematica front end. Any changes you make to this file will be *)
(* overwritten.                                                     *)
(*******************************************************************)



SingleValue[ds_,OptionsPattern[{Spacing->10^-5}]]:=Mean/@Split[Sort[ds
    ,(#1[[1]]<#2[[1]])&],(Abs[#1[[1]]-#2[[1]]]<OptionValue[Spacing]/2)&]
SingleValue::usage=
"SingleValue[ds] takes scans that overlap and averages together the overlapping
     points, making the function single-valued. This is particularly useful for
     Autoscan overlapping segments.";
Smooth[ds_,pts_]:={MovingAverage[ds[[All,1]],pts],MovingAverage[ds[[All,2]],pts
    ]}\[Transpose]
Smooth::usage=
"Smooth[ds,pts] is a moving average of pts over the data set ds.";
Decimate[ds_,pts_]:=Mean/@Partition[ds,pts]
Decimate::usage=
"Decimate[ds,pts] takes a list of points, ds, and averages pts together to
    reduce the size of the list";


QPlot[ds_,OptionsPattern[{PlotRange->All}]]:=ListPlot[ds,Joined->True,Frame->
    True,PlotRange->OptionValue[PlotRange],FrameLabel->{"Laser energy (\!\(\*
    SuperscriptBox[\(cm\), \(-1\)]\))","Signal (arb.)"},Axes->None]
QPlot::usage=
"QPlot[ds] is Listplot with some common options and graph labels enabled.";


ImportSCN[f_]:=Block[{
str=OpenRead[f,BinaryFormat->True],
sz=FileByteCount[f],
data,
scannum,
scanstart,interval,timeperseg,scandistance,date,time,
channels,
numchannels},{
BinaryReadList[str,"Integer8",26]; (* undocumented header "memory allocation
    information" *)
data=BinaryReadList[str,"Integer16",(sz-26-156)/2]; (* main data block *)
date=FromCharacterCode[Split[BinaryReadList[str,"UnsignedInteger8",10],(#2>10)
    &][[1]]]; (* string, date *)
time=FromCharacterCode[Split[BinaryReadList[str,"UnsignedInteger8",10],(#2>10)
    &][[1]]]; (* string, time *)
scannum=BinaryRead[str,"Integer16"]; (* scan ID number *)
{scanstart,interval,timeperseg,scandistance}=BinaryReadList[str,"Real64",4];
channels=BinaryReadList[str,"Integer16",38][[3;;14]];
numchannels=Length[Select[channels,(#>0)&]];
Close[str];
```

```
MapIndexed[{((#2[[2]]-1)interval+1000scanstart-201IntegerPart[(#2[[2]]-1)
    /10201])/29979.2458,#1}&,Partition[data,Length[data]/numchannels],{2}],
{ID->scannum,File->f,StartGHz->scanstart,DataIntervalMHz->interval,TimePer10GHz
    ->timeperseg,ScanDistance->scandistance,Channels->channels[[1;;numchannels
    ]],Date->date,Time->time,Labels->({"Thin Etalon","BRF","VET1","VET2","OAM1
    ","OAM2","Laser Power","Data 1","Data 2","Data 3","User defined"}[[#]]&/
    @channels[[1;;numchannels]])}
}]


ImportPACSV[f_,OptionsPattern[{TraplossCutoff->0.7}]]:=Block[{ds=Select[Rest[
    Import[f,"CSV"][[All,{2,4,3}]]],(#[[2]]>0)&],meantl},
meantl=OptionValue[TraplossCutoff]Mean[ds[[All,3]]];
ds=Select[ds,(#[[3]]>meantl)&];
{SingleValue[ds[[All,{1,2}]]],SingleValue[ds[[All,{1,3}]]]}]


Resample[ds1_,ds2_,OptionsPattern[{Resolution->10^-5,Shift->0,Slope->1}]]:=
    Block[{
min=Max[Min[ds1[[All,1]]],Min[ds2[[All,1]]]+OptionValue[Shift]],
max=Min[Max[ds1[[All,1]]],Max[ds2[[All,1]]]+OptionValue[Shift],(Max[ds2[[All
    ,1]]]-min)/OptionValue[Slope]+min+OptionValue[Shift]],
ipol1=Interpolation[SetPrecision[ds1,MachinePrecision]],
ipol2=Interpolation[SetPrecision[ds2,MachinePrecision]],
ref,set,refint,setint,normalization
},
ref=Table[{x,(*ipol1[x]**)ipol2[x-OptionValue[Shift]]},{x,min,max,OptionValue[
    Resolution]}];
set=Table[{x,(*ipol1[x]**)ipol2[OptionValue[Slope](x-min)-OptionValue[Shift]+
    min]},{x,min,max,OptionValue[Resolution]}];
refint=Total[ref[[All,2]]]*OptionValue[Resolution]*(max-min);
setint=Total[set[[All,2]]]*OptionValue[Resolution]*(max-min);
normalization=refint/setint;
{Table[{x,ipol1[x]},{x,min,max,OptionValue[Resolution]}],Table[{x,normalization
    *ipol2[OptionValue[Slope](x-min)-OptionValue[Shift]+min]},{x,min,max,
    OptionValue[Resolution]}](*,normalization*)
}]
Resample::usage="Resample[ds1,ds2,opts] resamples the two datasets on to the
    same range of X values. Options include:\[IndentingNewLine]Resolution\[Rule
    ]\!\(\*SuperscriptBox[\(10\), \(-5\)]\) for the spacing of points,\[
    IndentingNewLine]Shift\[Rule]0 for the shift of the second spectrum,
Slope\[Rule]1 to adjust the horizontal scaling of the second spectrum.
The integral of the second spectrum is normalized to remain constant after
    scaling. Returns an array of two data sets corresponding the the input data
    .";


AlignSpectra[refds_,moreds_,OptionsPattern[{Resolution->10^-5}]]:=Block[{
\[Alpha]=ParallelMap[FindMax\[Alpha][refds,#,Resolution->10OptionValue[
    Resolution]]&,moreds],
```

```
shift,min,max,ipol,refipol
},
shift=ParallelMap[MaxShift[refds,#[[1]],OptionValue[Resolution],#[[2]]]&,{
    moreds,\[Alpha]}\[Transpose]];
min=Max[MapThread[(#1+#2)&,{Min[#[[All,1]]]&/@moreds,shift}],Min[refds[[All
    ,1]]]];
max=Min[MapThread[((#1-min)/#2+#3+min)&,{Max[#[[All,1]]]&/@moreds,\[Alpha],
    shift}],Max[refds[[All,1]]]];
Print[\[Alpha],shift//N,NumberForm[min,10],", "NumberForm[max,10]];
ipol=Interpolation[SetPrecision[#,MachinePrecision]]&/@moreds;
refipol=Interpolation[SetPrecision[refds,MachinePrecision]];
Prepend[MapThread[Table[{x,#1[#2(x-min)-#3+min]},{x,min,max,OptionValue[
    Resolution]}]&,{ipol,\[Alpha],shift}],
Table[{x,refipol[x]},{x,min,max,OptionValue[Resolution]}]]
]


MergeDatasets[ds_]:=MapThread[{#1,Mean[#2]}&,{ds[[1,All,1]],(ds[[All,All,2]])\[
    Transpose]}]
MergeDatasets::usage=
"MergeDatasets[ds] averages together the y-values of multiple plots. It assumes
     that they all have the same x-values.";


Correlate[ds1_,ds2_,OptionsPattern[{Resolution->10^-5,Slope->1}]]:=Block[{t=
    Resample[ds1,ds2,Resolution->OptionValue[Resolution],Slope->OptionValue[
    Slope]],c,res=OptionValue[Resolution]},
c={res Range[1-Length[t[[1]]],Length[t[[1]]]-1],ListCorrelate[t[[1,All,2]],t
    [[2,All,2]],{-1,1},0]}\[Transpose];
{c,Sort[c,(#1[[2]]>#2[[2]])&][[1]]}
]
Correlate::usage=
"Correlate[ds1,ds2,options] will find the correlation function of two data sets
    , resampling them internally. Options are:
       Resolution\[Rule]\!\(\*SuperscriptBox[\(10\), \(-5\)]\) to pass to
           Resample
       Slope\[Rule]1.
It returns an array with two elements. The first is the correlation function.
    The second is a list of the shift (in wavenumbers) that gives the maximum
    of the corrlation function and that maximum.";


MaxCorrelation[ds1_,ds2_,r_,s_]:=(Correlate[ds1,ds2,Resolution-> r,Slope->s
    ][[2,2]])
MaxShift[ds1_,ds2_,r_,s_]:=-1*(Correlate[ds1,ds2,Resolution-> r,Slope->s
    ][[2,1]])
MaxCorrelation::usage=
"MaxCorrelation[ds1,ds2,resolution,slope] returns the maximum of the
    correlation function, calculated by Correlate.";
MaxShift::usage=
```

```
"MaxShift[ds1,ds2,resolution,slope] returns the shift of the second data set
    which gives the maximum of the correlation function, calculated by
    Correlate. Since Correlate simply shifts the register, the shift in x is
    the negative of this result, hence the -1 multiplier in the function";


FindMax\[Alpha][rempi1_,rempi2_,OptionsPattern[Resolution-> 10^-4]]:=Block[{
res = OptionValue[Resolution],
\[Epsilon]0 = .01,
\[Epsilon] = .01,
\[Alpha] = 1,
\[Alpha]1 = 1,
\[Alpha]2 = 1,
\[Alpha]3 = 1,
\[Alpha]4 = 1,
Final\[Alpha],
max1,FirstTry,FindMax,\[Xi],max2,max3,max4,AccuracyBounds,TwoThree,ThreeOne},
max1 = MaxCorrelation[rempi1,rempi2,res,\[Alpha]];
max3 = max1;
\[Phi] = (1+Sqrt[5])/2;
AccuracyBounds = 1*10^-4;
FirstTry=True;
FindMax = False;
\[Xi] = True;

While[\[Xi],(*outside loop defines boundary *)
       \[Alpha] = 1+\[Epsilon];
       max2 = MaxCorrelation[rempi1,rempi2,res,\[Alpha]];
       \[Alpha]2 = \[Alpha];

   Which[max2>=max3, (*normal behavior: max3 is middle point b/w 1 and 2 *)
         \[Epsilon]=\[Epsilon] + \[Epsilon]0;
       FirstTry=False,
  FirstTry, (*switch direction if first doesn't improve max *)
       \[Epsilon]0 = -\[Epsilon]0;
       \[Epsilon] = \[Epsilon]0;
       max3 = max2;
       \[Alpha]3 = \[Alpha]2;
       max2 = max1;
       \[Alpha]2 = \[Alpha]1;
       FirstTry = False,

   True, (*when the search bounds have been found, start Golden Section search
       *)
       \[Alpha]2 = \[Alpha];
       FindMax = True
   ];
     If[FindMax, (*Find the third starting point *)
       \[Alpha]3 = (\[Phi](\[Alpha]2 - \[Alpha]1))/(1+\[Phi]) + \[Alpha]1;
       max3 = MaxCorrelation[rempi1,rempi2,res,\[Alpha]3]
```

```
   ];

      While[FindMax, (*Golden Section search method *)
       TwoThree = False;
       ThreeOne = False;
       Which[Abs[\[Alpha]2 - \[Alpha]3]> Abs[\[Alpha]3 - \[Alpha]1], (*select
           the larger region *)
              TwoThree = True;
              \[Alpha]4 = (\[Phi](\[Alpha]2 - \[Alpha]3))/(1+\[Phi]) + \[Alpha
                  ]3,
        True,
              ThreeOne = True;
              \[Alpha]4 =( \[Phi](\[Alpha]3 - \[Alpha]1))/(1+\[Phi]) + \[Alpha
                  ]1
      ];
      max4 = MaxCorrelation[rempi1,rempi2,res,\[Alpha]4];

       Which[TwoThree,
              Which[max4>max3,
                     \[Alpha]1 = \[Alpha]3;
                     max1 = max3;
                     \[Alpha]3 = \[Alpha]4;
                     max3 = max4,
            max3>max4,
                     \[Alpha]2 = \[Alpha]4;
                     max2 = max4
                     ],
       ThreeOne,
              Which[max4>max3,
                     \[Alpha]2 = \[Alpha]3;
                     max2 = max3;
                     \[Alpha]3 = \[Alpha]4;
                     max3 = max4,
            max3>max4,
                     \[Alpha]1 = \[Alpha]4;
                     max1 = max4
                     ]
              ];
       If[Abs[(\[Alpha]2 - \[Alpha]1)/\[Alpha]1] < AccuracyBounds,(*sets
           accuracy bound on linear scaling *)
              Final\[Alpha] = \[Piecewise]{
 {\[Alpha]3, max3>max4},
 {\[Alpha]4, True}
};
              FindMax = False;
              \[Xi] = False
       ];
     ];
       max1 = max3;
       \[Alpha]1 = \[Alpha]3;
```

```
       max3 = max2;
       \[Alpha]3 = \[Alpha]2;
];Final\[Alpha]]
FindMax\[Alpha]::usage=
"FindMax\[Alpha][ds1,ds2,options] will return the linear scale factor (applied
    from the beginning of the data set) which maximizes the correlation
    function. The available options are:
       Resolution\[Rule]\!\(\*SuperscriptBox[\(10\), \(-4\)]\): the resolution
            over which the input data sets are resampled. Finer resolutions
           take significantly more processing time. \!\(\*SuperscriptBox[\(10\)
           , \(-4\)]\) is reasonable for PA spectra. \!\(\*SuperscriptBox
           [\(10\), \(-1\)]\) or \!\(\*SuperscriptBox[\(10\), \(\(-2\)\(\\\ \)
           \)]\)makes more sense for REMPI spectra.
       AccuracyBound\[Rule]\!\(\*SuperscriptBox[\(10\), \(-4\)]\): Separation
           between outer bounds of the search function, in wavenumbers. The
           actual distance between the output and the true optimum will be less
            than this value.
The return is a single number.";


LinearizeVET[data_,OptionsPattern[{Filter->0.01,VETOrder-> 7.7206 10^4,GHz->
    4.996641 10^5}]]:= Block[
{filterres=OptionValue[Filter],
FSR= OptionValue[GHz]/OptionValue[VETOrder] 1/30,
n=2,
MaxArray=Array[#&,1],
MinArray=Array[#&,1],
skip=0.05,
firstrun=True,
vet,svet,ssvet,
Freq,PTArray,datapts,f,g,h,j,fInverse,RefInverse,newVET
},
vet=data;
svet=SingleValue[{#1[[All,1]],#1[[All,2]]-Min[#1[[All,2]]]}\[Transpose]&[vet]];
ssvet={svet[[All,1]],LowpassFilter[svet[[All,2]],filterres,1000,HammingWindow
    ]}\[Transpose];

While[n<Length[ssvet],
(*If[ssvet\[LeftDoubleBracket]n,2\[RightDoubleBracket]==ssvet\[
    LeftDoubleBracket]n-1,2\[RightDoubleBracket],ssvet\[LeftDoubleBracket]n,2\[
    RightDoubleBracket]+1*10^-0];*)
If[firstrun,If[ssvet[[n,2]]>50,If[ssvet[[n,2]]>ssvet[[n-1,2]],If[ssvet[[n,2]]>
    ssvet[[n+1,2]],MaxArray=Append[MaxArray,n]]]];
If[ssvet[[n,2]]<50,If[ssvet[[n,2]]<ssvet[[n-1,2]],If[ssvet[[n,2]]<ssvet[[n
    +1,2]],MinArray=Append[MinArray,n]]]];
firstrun=False;,
If[ssvet[[n,1]]>ssvet[[MaxArray[[Length[MaxArray]]],1]]+skip,If[ssvet[[n
    ,2]]>50,If[ssvet[[n,2]]>ssvet[[n-1,2]],If[ssvet[[n,2]]>ssvet[[n+1,2]],
    MaxArray=Append[MaxArray,n]]]]];
```

```
If[ssvet[[n,1]]>ssvet[[MinArray[[Length[MinArray]]],1]]+skip,If[ssvet[[n
    ,2]]<50,If[ssvet[[n,2]]<ssvet[[n-1,2]],If[ssvet[[n,2]]<ssvet[[n+1,2]],
    MinArray=Append[MinArray,n]]]]];
];
n=n+1
];
MaxArray=Drop[MaxArray,1];
MinArray=Drop[MinArray,1];

Freq=Sort[Flatten[Append[MaxArray,MinArray]]];
PTArray=Array[ssvet[[Freq[[#]]]]&,Length[Freq]];

datapts=Array[{#-1,PTArray[[#,1]]}&,Length[PTArray]];
Block[{x},f[x_]=Fit[datapts,{1,x,x^2,x^3},x]];
g[x_]:=FSR/2 x + f[0];
h[x_]=ConditionalExpression[f[x],-2<x<(Length[datapts]+2)];
fInverse=InverseFunction[h];
RefInverse[x_]:=Re[fInverse[x]];
j[x_]:=RefInverse[vet[[x,1]]];
newVET=Array[{g[j[#]],vet[[#,2]]}&,Length[vet]]
]
LinearizeVET::usage=
"LinearizeVET[vetdata,options] takes a set of VET data from a Coherent 899-29
    laser and attempts to correct the scan linearization using the peaks and
    troughs of the data set. Options are:
       Filter\[Rule]0.01 to LowPassFilter the VET data
       GHz\[Rule] 4.996641 \!\(\*SuperscriptBox[\(10\), \(5\)]\) and
       VETOrder\[Rule] 7.7206 \!\(\*SuperscriptBox[\(10\), \(4\)]\) are V1 and
            N1, respectively, from the CAL.AS AutoScan calibration file. They
           represent the frequency and VET order of the factory test when the
           FSR was measured. The default parameters give the FSR of VET1 on
           Laser3 in room P007A.
The return element is the original VET data on the linearized axis. The 'x'
    values of the scan can be applied directly to the recorded data from the
    same scan.";


LinearizeData[data_,OptionsPattern[{Filter->0.01,VETOrder-> 7.7206 10^4,GHz->
    4.996641 10^5}]]:=
Block[{scan=data[[3]],
vet=data[[2]],
newvet,newscan
},
newvet=LinearizeVET[vet,Filter->0.01,VETOrder-> 7.7206 10^4,GHz-> 4.996641
    10^5];
newscan={#1[[All,1]],#2[[All,2]]}\[Transpose]&[newvet,scan]
]
LinearizeData::usage=
"LinearizeData[data,options] uses VET data, via LinearizeVET, to linearize a
    data scan from a Coherent 899-29 laser. The data given to LinearizeData
```

```
    should have four scans: background, VET, molecules, and MOT, in that order.
     The options are the same as for LinearizeVET, as they are just pass-
    throughs.";
```

D.2 Sample Alignment Code

```
<< "C:\\Users\\Ultracold Molecules\\Documents\\Carollo\\Mathematica \
Data Analysis 0.1.3\\SpectrumAnalysis.m"

ref = ImportPACSV[
    "C:\\Users\\Ultracold Molecules\\Documents\\Carollo\\Mathematica \
Data Analysis 0.1.3\\scan36.csv"][[:1:]]:;
moreds = {ImportPACSV[
     "C:\\Users\\Ultracold Molecules\\Documents\\Carollo\\Mathematica \
Data Analysis 0.1.3\\scan37.csv"][[:1:]]:,
   ImportPACSV[
     "C:\\Users\\Ultracold Molecules\\Documents\\Carollo\\Mathematica \
Data Analysis 0.1.3\\scan38.csv"][[:1:]]:,
   ImportPACSV[
     "C:\\Users\\Ultracold Molecules\\Documents\\Carollo\\Mathematica \
Data Analysis 0.1.3\\scan39.csv"][[:1:]]:};

QPlot[Prepend[moreds, ref]]


AbsoluteTiming[ads = AlignSpectra[ref, moreds]][[:1:]]:

{1.008,1.00348,1.00652}{-0.00079,-0.00221,-0.00112}12566.79977, 12567.12942

15.7000220

QPlot[ads:[[:1:]]:]
QPlot[MergeDatasets[ads]]
```

Appendix E

MATLAB Code

This appendix contains MATLAB files used in extracting MOT parameters from absorption imaging data. All of them are various parts of the ImageAtoms3a program, except for Appendix E.10, which uses width parameters output by ImageAtoms3a to calculate the MOT temperature. Appendix E.1 is the main program which calls all the others as subroutines.

E.1 ImageAtoms3a.m

```
function varargout = ImageAtoms3a(varargin)
% IMAGEATOMS3A M-file for ImageAtoms3a.fig
%      IMAGEATOMS3A, by itself, creates a new IMAGEATOMS3A or raises the
    existing
%      singleton*.
%
%      H = IMAGEATOMS3A returns the handle to a new IMAGEATOMS3A or the handle
    to
%      the existing singleton*.
%
%      IMAGEATOMS3A('CALLBACK',hObject,eventData,handles,...) calls the local
%      function named CALLBACK in IMAGEATOMS3A.M with the given input
    arguments.
%
%      IMAGEATOMS3A('Property','Value',...) creates a new IMAGEATOMS3A or
    raises the
%      existing singleton*. Starting from the left, property value pairs are
%      applied to the GUI before ImageAtoms3a_OpeningFcn gets called. An
%      unrecognized property name or invalid value makes property application
%      stop. All inputs are passed to ImageAtoms3a_OpeningFcn via varargin.
%
%      *See GUI Options on GUIDE's Tools menu. Choose "GUI allows only one
```

```
%     instance to run (singleton)".
%
% See also: GUIDE, GUIDATA, GUIHANDLES

% Developed by Dajun Wang @ UConn Physics
% by Dajun v1.0 11-Oct-2005 21:55:53
%Last modified 26-Nov-2005 23:15:53

%modified by Ryan Carollo to change definition of width to a standard
%deviation on 27-Jan-2009

%partly rewritten by Ryan Carollo on 18-Nov-2009 to utilize new -3 versions
%which include new fitting algorithms and a two gaussian fit method

% Begin initialization code - DO NOT EDIT
gui_Singleton = 1;
gui_State = struct('gui_Name',    mfilename, ...
                   'gui_Singleton', gui_Singleton, ...
                   'gui_OpeningFcn', @ImageAtoms3a_OpeningFcn, ...
                   'gui_OutputFcn', @ImageAtoms3a_OutputFcn, ...
                   'gui_LayoutFcn', [] , ...
                   'gui_Callback', []);
if nargin && ischar(varargin{1})
    gui_State.gui_Callback = str2func(varargin{1});
end

if nargout
    [varargout{1:nargout}] = gui_mainfcn(gui_State, varargin{:});
else
    gui_mainfcn(gui_State, varargin{:});
end
% End initialization code - DO NOT EDIT
end


% --- Executes just before ImageAtoms3a is made visible.
function ImageAtoms3a_OpeningFcn(hObject, eventdata, handles, varargin)
% This function has no output args, see OutputFcn.
% hObject   handle to figure
% eventdata reserved - to be defined in a future version of MATLAB
% handles   structure with handles and user data (see GUIDATA)
% varargin  command line arguments to ImageAtoms3a (see VARARGIN)

% Choose default command line output for ImageAtoms3a
handles.output = hObject;

% Update handles structure
guidata(hObject, handles);

% UIWAIT makes ImageAtoms3a wait for user response (see UIRESUME)
```

```
% uiwait(handles.figure1);
end %opening function


% --- Outputs from this function are returned to the command line.
function varargout = ImageAtoms3a_OutputFcn(hObject, eventdata, handles)
% varargout cell array for returning output args (see VARARGOUT);
% hObject   handle to figure
% eventdata reserved - to be defined in a future version of MATLAB
% handles   structure with handles and user data (see GUIDATA)

% Get default command line output from handles structure
varargout{1} = handles.output;
end %output


function Directory_edit_Callback(hObject, eventdata, handles)
% hObject   handle to Directory_edit (see GCBO)
% eventdata reserved - to be defined in a future version of MATLAB
% handles   structure with handles and user data (see GUIDATA)

% Hints: get(hObject,'String') returns contents of Directory_edit as text
%       str2double(get(hObject,'String')) returns contents of Directory_edit
    as a double

image_directory = get(hObject,'string'); %get name of image file folder
imagetype='\*atom.tif';
%image_directory = strcat(image_directory,imagetype); %select atom images, not
    probe or dark images
image_list = dir(strcat(image_directory,imagetype));            %get list of
    images

image_list = [image_list; dir(strcat(image_directory,'\*atom.png'))]; %adds a
    list
%of .png files to the .tif file list

dblist = {image_list.name}';
if ~isempty(dblist)
    set(handles.file_listbox,'string',dblist);
end

end %directory callback


% --- Executes during object creation, after setting all properties.
function Directory_edit_CreateFcn(hObject, eventdata, handles)
% hObject   handle to Directory_edit (see GCBO)
% eventdata reserved - to be defined in a future version of MATLAB
% handles   empty - handles not created until after all CreateFcns called
```

```
% Hint: edit controls usually have a white background on Windows.
%       See ISPC and COMPUTER.
if ispc && isequal(get(hObject,'BackgroundColor'),
    get(0,'defaultUicontrolBackgroundColor'))
    set(hObject,'BackgroundColor','white');
end

end %directory creation


% --- Executes on selection change in file_listbox.
function file_listbox_Callback(hObject, eventdata, handles)
% hObject   handle to file_listbox (see GCBO)
% eventdata reserved - to be defined in a future version of MATLAB
% handles   structure with handles and user data (see GUIDATA)

% Hints: contents = cellstr(get(hObject,'String')) returns file_listbox
%contents as cell array contents{get(hObject,'Value')} returns selected
%item from file_listbox

%% read in image and convert it to double class
[img1,img2,img3] = getimagefile(handles);

iatom = im2double(img1);
iprobe = im2double(img2);
idark = im2double(img3);
iabs = imdivide(iatom-idark,iprobe-idark);

%% inverse the absorption images for better visulization effect
iabs=1-iabs;

subplot(2,3,1), imshow(iatom),axis on,colormap(jet(256)), title('atom');
subplot(2,3,2), imshow(iprobe),axis on,colormap(jet(256)), title('probe');
subplot(2,3,4), imshow(idark),axis on,colormap(jet(256)), title('dark');
subplot(2,3,5), imshow(iabs),axis on,colormap(jet(256)), title('absorption');
end %file list callback


% --- Executes during object creation, after setting all properties.
function file_listbox_CreateFcn(hObject, eventdata, handles)
% hObject   handle to file_listbox (see GCBO)
% eventdata reserved - to be defined in a future version of MATLAB
% handles   empty - handles not created until after all CreateFcns called

% Hint: listbox controls usually have a white background on Windows.
%       See ISPC and COMPUTER.
if ispc && isequal(get(hObject,'BackgroundColor'),
    get(0,'defaultUicontrolBackgroundColor'))
    set(hObject,'BackgroundColor','white');
end
```

```
end %file list creation


% --- Executes on button press in Gauss1D_button.
function Gauss1D_button_Callback(hObject, eventdata, handles)
% hObject   handle to Gauss1D_button (see GCBO)
% eventdata reserved - to be defined in a future version of MATLAB
% handles   structure with handles and user data (see GUIDATA)

%% read in images from the listbox
[img1,img2,img3] = getimagefile(handles);

fit_two = get(handles.FitTwo_check, 'Value'); %gives status of FitTwo checkbox

%% smooth the image to remove high level noises and calculate optical
%% density corresponding to each pixel
[iOD,iabs] = smoothOD2(img1,img2,img3);
subplot(2,3,1);imshow(1-iabs); axis on; title('smoothed'); colormap(jet(256));

pitch = 7.4*10^(-6); %pixel pitch
magnification = 1.72; %physical size of image is greater than object size
                      %by this factor
opticalM = magnification/(100*pitch); %pixels per cm

if(fit_two)
%% two directional 1D Gauss fit
[f1Dx, f1Dy] = Gaussian1D_3a(iOD,1e-10);
%%fD=[center, width, peakOD, offset]

string1='CO2 y center =';
string2=num2str(f1Dy(5));
string3='MOT x half width (mm) =';
string4=num2str(f1Dx(2)/opticalM*10);
string5 ='MOT y half width (mm) =';
string6=num2str(f1Dy(2)/opticalM*10);
string7='CO2 y half width (mm) =';
string8=num2str(f1Dy(6)/opticalM*10);

%fittype('a+ b*exp(-(x-x0).^2./(2*s1.^2)) + c*exp(-(x-x02).^2./(2*s2.^2))'
%'coefficients',{'x0','s1','b','a','x02','s2','c'}

%% calculate atom number and peak density. The peak optical density is the
%% average of x and y direction.
%peakOD = (f1Dx(7)./f1Dy(6)+f1Dy(7)./f1Dx(6))./(2.*sqrt(2.*pi)); %this extracts
           %the peak value from the integrated value that was actually fit
               along
           %each dimension, then averages them

%We are no longer fitting the CO2 x-width - it fits poorly - so the MOT
%width is being used as a stand-in for the 1D number and density estimates
```

```
CO2_OD = f1Dy(7)./(f1Dx(2).*sqrt(2.*pi)); %this extracts the peak value from
                                    %the integrated value along the y-axis
MOT_OD = (f1Dx(3)./f1Dy(2)+f1Dy(3)./f1Dx(2))./(2.*sqrt(2.*pi)); %the average
                                        %MOT density from x and y fits
[MOT_atom_number,MOT_atom_peakdensity] = atomDensity2(f1Dx(2), f1Dy(2),
    MOT_OD);
[CO2_atom_number,CO2_atom_peakdensity] = atomDensity2(f1Dx(2), f1Dy(6),
    CO2_OD);

string9 = 'MOT atom number =';
string10 = num2str(MOT_atom_number,'%10.4e');
string11 = 'MOT peak density =';
string12 = num2str(MOT_atom_peakdensity,'%10.4e');
string13 = 'CO2 atom number =';
string14 = num2str(CO2_atom_number,'%10.4e');
string15 = 'CO2 peak density =';
string16 = num2str(CO2_atom_peakdensity,'%10.4e');

MOTfitparameters = strvcat(string1,string2,string3,string4,string5,string6,...
    string7,string8,string9,string10,string11,string12,string13,string14,...
    string15,string16);
plotGaussian_3a(f1Dx,f1Dy,iOD);
set(handles.ParameterDisplay,'string',MOTfitparameters);
else
%% two directional 1D Gauss fit
[f1Dx, f1Dy] = Gaussian1D_3(iOD,1e-10);
%%fD=[center, width, peakOD, offset]

string1='x center =';
string2=num2str(f1Dx(1));
string3='y center =';
string4=num2str(f1Dy(1));
string5='x half width (mm) =';
string6=num2str(f1Dx(2)/opticalM*10);
string7 ='y half width (mm) =';
string8=num2str(f1Dy(2)/opticalM*10);
string9='x peak optical density =';
string10=num2str(f1Dx(3)./(f1Dy(2)*sqrt(2*pi)));
string11='y peak optical density =';
string12=num2str(f1Dy(3)./(f1Dx(2)*sqrt(2*pi)));

%% calculate atom number and peak density. The peak optical density is the
%% average of x and y direction.
peakOD = (f1Dx(3)./f1Dy(2)+f1Dy(3)./f1Dx(2))/(2*sqrt(2*pi)); %this extracts
                  %the peak value from the integrated value that was actually
                  %fit along each dimension, then averages them
[atom_number,atom_peakdensity] = atomDensity2(f1Dx(2), f1Dy(2), peakOD);

string13 = 'atom number =';
```

```
string14 = num2str(atom_number,'%10.4e');
string15 = 'peak density =';
string16 = num2str(atom_peakdensity,'%10.4e');

MOTfitparameters = strvcat(string1,string2,string3,string4,string5,string6,...
    string7,string8,string9,string10,string11,string12,string13,string14,...
    string15,string16);

plotGaussian_3(f1Dx,f1Dy,iOD);
set(handles.ParameterDisplay,'string',MOTfitparameters);
end
beep;

end %Gauss1D


% --- Executes on button press in Gauss2D_button.
function Gauss2D_button_Callback(hObject, eventdata, handles)
% hObject   handle to Gauss2D_button (see GCBO)
% eventdata reserved - to be defined in a future version of MATLAB
% handles   structure with handles and user data (see GUIDATA)

%% read in image
[img1,img2,img3] = getimagefile(handles);

fit_two = get(handles.FitTwo_check, 'Value'); %gives value of FitTwo checkbox

%% smooth the image to remove high level noises
%iOD = smoothOD(img);

[iOD,iabs] = smoothOD2(img1,img2,img3);
subplot(2,3,1);imshow(1-iabs); axis on; title('smoothed'); colormap(jet(256));

pitch = 7.4*10^(-6); %pixel pitch
magnification = 1.72; %physical size of image is greater than object size
                      %by this factor
opticalM = magnification/(100*pitch); %pixels per cm

%% 2D Gauss fit
if(fit_two)

[f1Dx,f1Dy,f2D] = Gaussian2D_3a(iOD,1e-10);
%%fD=[center, width, peakOD, offset]
string1 = 'MOT x half width (mm) =';
string2 = num2str(f2D(3)/opticalM*10);
string3 = 'MOT y half width (mm) =';
string4 = num2str(f2D(4)/opticalM*10);
string5 = 'CO2 x half width (mm) =';
string6 = num2str(f2D(10)/opticalM*10);
string7 = 'CO2 y half width (mm) =';
```

```
string8 = num2str(f2D(11)/opticalM*10);


%% calculate MOT atom number and peak density
MOT_OD = f2D(5);
[MOT_atom_number,MOT_atom_peakdensity] = atomDensity2(f2D(3), f2D(4), MOT_OD);
string9 = 'MOT atom number =';
string10 = num2str(MOT_atom_number,'%10.4e');
string11 = 'MOT peak density =';
string12 = num2str(MOT_atom_peakdensity,'%10.4e');


%% calculate CO2 atom number and peak density
CO2_OD = f2D(12);
[CO2_atom_number,CO2_atom_peakdensity] = atomDensity2(f2D(10), f2D(11),
    CO2_OD);
string13 = 'CO2 atom number =';
string14 = num2str(CO2_atom_number,'%10.4e');
string15 = 'CO2 peak density =';
string16 = num2str(CO2_atom_peakdensity,'%10.4e');
MOTfitparameters = strvcat(string1,string2,string3,string4,string5,string6,...
    string7,string8,string9,string10,string11,string12,string13,string14,...
    string15,string16);

set(handles.ParameterDisplay,'string',MOTfitparameters);

plotresidual = get(handles.residual_check, 'Value');
if (plotresidual)
   plotGaussian_3a(f1Dx,f1Dy,iOD,f2D,plotresidual);
else
  plotGaussian_3a(f1Dx,f1Dy,iOD,f2D);
end

else
[f1Dx,f1Dy,f2D] = Gaussian2D_3(iOD,1e-10);
%%fD=[center, width, peakOD, offset]
string1 = 'x center =';
string2 = num2str(f2D(1));
string3 = 'y center =';
string4 = num2str(f2D(2));
string5 = 'x half width (mm) =';
string6 = num2str(f2D(3)/opticalM*10);
string7 = 'y half width (mm) =';
string8 = num2str(f2D(4)/opticalM*10);
string9 = 'peak optical density =';
peakOD=f2D(5);
%peakOD=f2D(5)+0.5*f2D(6)+0.5*f2D(7);
string10 = num2str(peakOD);

%% calculate atom number and peak density
```

```
[atom_number,atom_peakdensity] = atomDensity2(f2D(3), f2D(4), peakOD);
string11 = 'atom number =';
string12 = num2str(atom_number,'%10.4e');
string13 = 'peak density =';
string14 = num2str(atom_peakdensity,'%10.4e');
MOTfitparameters = strvcat(string1,string2,string3,string4,string5,string6,...
    string7,string8,string9,string10,string11,string12,string13,string14);

set(handles.ParameterDisplay,'string',MOTfitparameters);

plotresidual = get(handles.residual_check, 'Value');
if (plotresidual)
   plotGaussian_3(f1Dx,f1Dy,iOD,f2D,plotresidual);
else
  plotGaussian_3(f1Dx,f1Dy,iOD,f2D);
end

end

beep;

end %Gauss2D


% --- Executes on button press in LoadImages_button.
function LoadImages_button_Callback(hObject, eventdata, handles)
% hObject   handle to LoadImages_button (see GCBO)
% eventdata reserved - to be defined in a future version of MATLAB
% handles   structure with handles and user data (see GUIDATA)

[pathstr,name,ext,versn] = fileparts(get(handles.Directory_edit,'string'));
if isempty(pathstr),
    image_directory = uigetdir('--','Select an Image database');
else
    image_directory = uigetdir([pathstr '\' name],'Select an Image database');
end

if image_directory,
    set(handles.Directory_edit,'string',image_directory);
    imagetype='\*atom.tif';
    %image_directory = strcat(image_directory,imagetype);
    image_list = dir(strcat(image_directory,imagetype));

    image_list = [image_list; dir(strcat(image_directory,'\*atom.png'))];

    dblist = {image_list.name}';
    set(handles.file_listbox,'string',dblist);
    set(handles.Gauss1D_button,'Enable','on');
    set(handles.Gauss2D_button,'Enable','on');
end
```

```
end %LoadImages


% --- Executes on button press in Quit_button.
function Quit_button_Callback(hObject, eventdata, handles)
% hObject   handle to Quit_button (see GCBO)
% eventdata reserved - to be defined in a future version of MATLAB
% handles   structure with handles and user data (see GUIDATA)
close(gcbf);
end %quit


% --- Executes on button press in residual_check.
function residual_check_Callback(hObject, eventdata, handles)
% hObject   handle to residual_check (see GCBO)
% eventdata reserved - to be defined in a future version of MATLAB
% handles   structure with handles and user data (see GUIDATA)

% Hint: get(hObject,'Value') returns toggle state of residual_check
end %residual callback


% --- Executes on button press in narrow_check.
function narrow_check_Callback(hObject, eventdata, handles)
% hObject   handle to narrow_check (see GCBO)
% eventdata reserved - to be defined in a future version of MATLAB
% handles   structure with handles and user data (see GUIDATA)

% Hint: get(hObject,'Value') returns toggle state of narrow_check
end %narrow callback


% --- Executes on button press in FitTwo_check.
function FitTwo_check_Callback(hObject, eventdata, handles)
% hObject   handle to FitTwo_check (see GCBO)
% eventdata reserved - to be defined in a future version of MATLAB
% handles   structure with handles and user data (see GUIDATA)

% Hint: get(hObject,'Value') returns toggle state of FitTwo_check
end %FitTwo callback


% --- Executes on button press in clip_check.
function clip_check_Callback(hObject, eventdata, handles)
% hObject   handle to clip_check (see GCBO)
% eventdata reserved - to be defined in a future version of MATLAB
% handles   structure with handles and user data (see GUIDATA)

% Hint: get(hObject,'Value') returns toggle state of clip_check
```

```
end %clip callback


function clip_edit_Callback(hObject, eventdata, handles)
% hObject   handle to clip_edit (see GCBO)
% eventdata reserved - to be defined in a future version of MATLAB
% handles   structure with handles and user data (see GUIDATA)

% Hints: get(hObject,'String') returns contents of clip_edit as text
%       str2double(get(hObject,'String')) returns contents of clip_edit as
%       a double
end


% --- Executes during object creation, after setting all properties.
function clip_edit_CreateFcn(hObject, eventdata, handles)
% hObject   handle to clip_edit (see GCBO)
% eventdata reserved - to be defined in a future version of MATLAB
% handles   empty - handles not created until after all CreateFcns called

% Hint: edit controls usually have a white background on Windows.
%      See ISPC and COMPUTER.
if ispc && isequal(get(hObject,'BackgroundColor'),
    get(0,'defaultUicontrolBackgroundColor'))
    set(hObject,'BackgroundColor','white');
end

end

function [image1, image2, image3] = getimagefile(handles)

contents = get(handles.file_listbox,'String');
file1 = contents{get(handles.file_listbox,'Value')};
image_directory = get(handles.Directory_edit,'string');
image1 = imread([image_directory '\' file1]);

%file1 is the name of the image with atoms. The other two image names are
%generated follow the same rule. So we can get them.

filenumber = file1(:,1:3);
%file2 = strcat(filenumber,'probe.tif');
file2 = strrep(file1, 'atom', 'probe');
image2 = imread([image_directory '\' file2]);

%file3 = strcat(filenumber,'dark.tif');
file3 = strrep(file1, 'atom', 'dark');
image3 = imread([image_directory '\' file3]);

narrow = get(handles.narrow_check,'Value'); %gives narrower image to fit CO2
    trap
```

```
clip = get(handles.clip_check,'Value'); %check to clip bad data off top of
    image

[sizey sizex] = size(image1);
pixel_number = get(handles.clip_edit,'string'); %get the number of pixels to
    clip
n = str2double(pixel_number);

if(narrow)
    image1 = image1(200:270,:);
    image2 = image2(200:270,:);
    image3 = image3(200:270,:);
elseif(clip)
    image1 = image1(n:sizey,:);
    image2 = image2(n:sizey,:);
    image3 = image3(n:sizey,:);
end

end
```

E.2 Gaussian1D_3.m

```
function [f1Dx,f1Dy] = Gaussian1D_3(m,tol)
%%%%%%%%%%%%%%%%%%%%%%%%%%%%%%%%%%%%%%%%%%%%%%%%%%%%%%%%%%%%%%%%
%% a function to fit a thermal atomic cloud to two directional 1-D Gauss
%% m  : Image
%% tol: fitting tolerance
%% this is the core of the whole imageAtoms program. Based on program from
%% http://jilawww.colorado.edu/bec/BEC_for_everyone/
%% Last modified by Dajun Wang @10/11/2005

%modified by Ryan Carollo to change width defninition to a standard
%deviation on 27-Jan-2009

%rewritten by Ryan Carollo to use methods form the Curve Fitting Toolbox
%that are much more straightforward and user-friendly on 18-Nov-2009

%the vertical offset has been clamped to zero
%%%%%%%%%%%%%%%%%%%%%%%%%%%%%%%%%%%%%%%%%%%%%%%%%%%%%%%%%%%%%%%%

[sizey sizex] = size(m);
[cx,cy,sx,sy,xprofile,yprofile] = centerofmass(m);
%pOD = max(max(m)); %'peak optical depth' - This returns the largest-valued
    pixel from the image
                %   to be used later as an initial guess for fitting
pOD = (max(xprofile)+max(yprofile))/2; %peak optical depth of collapsed image


%mx = m(round(cy),:)'; %chooses the slice along x through the y center of mass
xprofile = xprofile';
```

```
x1D = (1:sizex)';


%my = m(:,round(cx)); %chooses the slice along y through the x center of mass
yprofile = yprofile';
y1D = (1:sizey)';


%%%%%%%%%%%%%%%%%%%%%%%%%%%%%%%%%%%%%%%%%%%%%%%%%%%%%%%%%%%%%%%%%%%%%%%%%%%%
% PURPOSE: find center of mass of distribution
function [cx,cy,sx,sy,vx,vy] = centerofmass(m)

[sizey sizex] = size(m);
vx = sum(m);          %adds all y-values for each x-value, giving summed x
    cross section, averaged by number of pixels
vy = sum(m');         %same as above, but giving y cross section

vx = vx.*(vx>0);      %apparently removes any negative-value pixels
vy = vy.*(vy>0);

x = 1:sizex;        %vectors counting the pixels along each image axis
y = 1:sizey;

cx = sum(vx.*x)/sum(vx); %finds x and y centers of 'mass'
cy = sum(vy.*y)/sum(vy);

sx = sqrt(sum(vx.*(abs(x-cx).^2))/sum(vx)); %standard deviation in x and y
sy = sqrt(sum(vy.*(abs(y-cy).^2))/sum(vy));
end
%%%%%%%%%%%%%%%%%%%%%%%%%%%%%%%%%%%%%%%%%%%%%%%%%%%%%%%%%%%%%%%%%%%%%%%%%%%%

ox = fitoptions('Method','NonlinearLeastSquares',...
                  'Algorithm','Trust-Region',...
                  'StartPoint',[cx,sx,pOD,0],...      %initial guesses for
                     fitted x coefficients
                  'Lower',[-Inf,0,0,0],...            %prevent negative values
                  'Upper',[Inf,Inf,Inf,Inf],...
                  'TolFun',tol,...
                  'MaxFunEvals',1000,'MaxIter',1000);

oy = fitoptions('Method','NonlinearLeastSquares',...
                  'Algorithm','Trust-Region',...
                  'StartPoint',[cy,sy,pOD,0],...      %initial guesses for
                     fitted y coefficients
                  'Lower',[-Inf,0,0,0],...            %prevent negative values
                  'Upper',[Inf,Inf,Inf,Inf],...
                  'TolFun',tol,...
                  'MaxFunEvals',1000,'MaxIter',1000);

%model = a + b*exp(-(x-x0).^2./(2*s^2)); %the gaussian function used for
```

```
    fitting

gaussx = fittype('a + b*exp(-(x-x0).^2./(2*s^2))',... %the gaussian function
    used for fitting
               'coefficients',{'x0','s','b','a'},...
               'independent','x',...
               'dependent','gaussx',...
               'options',ox);

gaussy = fittype('a + b*exp(-(x-x0).^2./(2*s^2))',... %the gaussian function
    used for fitting
               'coefficients',{'x0','s','b','a'},...
               'independent','x',...
               'dependent','gaussy',...
               'options',oy);


fitx = fit(x1D,xprofile,gaussx); %fit the data to the gaussian model
fity = fit(y1D,yprofile,gaussy);

f1Dx = coeffvalues(fitx); %extract the coefficients form the fit data
f1Dy = coeffvalues(fity);

%%%%%%%%%%%%%%%%%%%%%%%%%%%%%%%%%%%%%%%%%%%%%%%%%%%%%%%%%%%
end
```

E.3 Gaussian1D_3a

```
function [f1Dx,f1Dy] = Gaussian1D_3a(m,tol)
%%%%%%%%%%%%%%%%%%%%%%%%%%%%%%%%%%%%%%%%%%%%%%%%%%%%%%%%%%%
%% a function to fit a thermal atomic cloud to two directional 1-D Gauss
%% m  : Image
%% tol: fitting tolerance
%% this is the core of the whole imageAtoms program. Based on program from
%% http://jilawww.colorado.edu/bec/BEC_for_everyone/
%% Last modified by Dajun Wang @10/11/2005

%modified by Ryan Carollo to change width defninition to a standard
%deviation on 27-Jan-2009

%rewritten by Ryan Carollo to use methods form the Curve Fitting Toolbox
%that are much more straightforward and user-friendly on 18-Nov-2009

%the vertical offset has been clamped to zero
%%%%%%%%%%%%%%%%%%%%%%%%%%%%%%%%%%%%%%%%%%%%%%%%%%%%%%%%%%%

[sizey sizex] = size(m);
[cx,cy,sx,sy,xprofile,yprofile] = centerofmass(m);
%pOD = max(max(m)); %'peak optical depth' - This returns the largest-valued
    pixel from the image
```

```
                  %  to be used later as an initial guess for fitting
pODx = max(xprofile); %peak optical depth of collapsed image
pODy = max(yprofile);

%pODmx = 2.*pODx./3;  %use this as a guess for the MOT
pODmy = 2.*pODy./3;

%sx2 = 1.2.*sx;       %initial guesses for the CO2 trap gaussian
sy2 = sy/15;          %sy is gaussian width, cy is center
%cx2 = cx;
cy2 = 0.85*cy;        %can be varied to help algorithm find
                      %the dipole trap


%mx = m(round(cy),:)'; %chooses the slice along x through the y center of mass
xprofile = xprofile';
x1D = (1:sizex)';


%my = m(:,round(cx))'; %chooses the slice along y through the x center of mass
yprofile = yprofile';
y1D = (1:sizey)';


%%%%%%%%%%%%%%%%%%%%%%%%%%%%%%%%%%%%%%%%%%%%%%%%%%%%%%%%%%%%%%%%%%%%%%%%%%%%
% PURPOSE: find center of mass of distribution
function [cx,cy,sx,sy,vx,vy] = centerofmass(m)

[sizey sizex] = size(m);
vx = sum(m);          %adds all y-values for each x-value, giving summed x
    cross section
vy = sum(m');         %same as above, but giving y cross section

vx = vx.*(vx>0);      %apparently removes any negative-value pixels
vy = vy.*(vy>0);

x = 1:sizex;        %vectors counting the pixels along each image axis
y = 1:sizey;

cx = sum(vx.*x)/sum(vx); %finds x and y centers of 'mass'
cy = sum(vy.*y)/sum(vy);

sx = sqrt(sum(vx.*(abs(x-cx).^2))/sum(vx)); %standard deviation in x and y
sy = sqrt(sum(vy.*(abs(y-cy).^2))/sum(vy));
end
%%%%%%%%%%%%%%%%%%%%%%%%%%%%%%%%%%%%%%%%%%%%%%%%%%%%%%%%%%%%%%%%%%%%%%%%%%%%

%ox = fitoptions('Method','NonlinearLeastSquares',...
%                  'Algorithm','Trust-Region',...
%                  'StartPoint',[cx,sx,pODmx,0,cx2,sx2,pODx],...     %initial
```

```
    guesses for fitted x coefficients
%                   'Lower',[-Inf,0,0,0,-Inf,0,0],...              %prevent
    negative values
%                   'Upper',[Inf,sizex,1000,Inf,Inf,sizex,1.5*pODx],... %try to
    keep routine from wandering off
%                   'TolFun',tol,...
%                   'MaxFunEvals',5000,'MaxIter',5000);

%the x-direction fit is done to only one gaussian, as the CO2 trap is not
%sufficiently different in size from the MOT to be fit effectively

ox = fitoptions('Method','NonlinearLeastSquares',...
                  'Algorithm','Trust-Region',...
                  'StartPoint',[cx,sx,pODx,0],...      %initial guesses for
                     fitted x coefficients
                  'Lower',[-Inf,0,0,0],...            %prevent negative values
                  'Upper',[Inf,Inf,Inf,Inf],...
                  'TolFun',tol,...
                  'MaxFunEvals',5000,'MaxIter',5000);

oy = fitoptions('Method','NonlinearLeastSquares',...
                  'Algorithm','Trust-Region',...
                  'StartPoint',[cy,sy,pODmy,0,cy2,sy2,pODy],...     %initial
                     guesses for fitted y coefficients
                  'Lower',[-Inf,0,0,0,0,1,0.1*pODy],...             %prevent
                     negative values
                  'Upper',[Inf,sizey,1000,Inf,Inf,30,1.5*pODy],...  %try to
                     keep routine from wandering off
                  'TolFun',tol,...
                  'MaxFunEvals',5000,'MaxIter',5000);

%gaussx = fittype('a + b*exp(-(x-x0).^2./(2*s1.^2)) +
    c*exp(-(x-x02).^2./(2*s2.^2))',... %the 2-gaussian function used for
    fitting
%               'coefficients',{'x0','s1','b','a','x02','s2','c'},...
%               'independent','x',...
%               'dependent','gaussx',...
%               'options',ox);

gaussx = fittype('a + b*exp(-(x-x0).^2./(2*s^2))',... %the gaussian function
    used for fitting
              'coefficients',{'x0','s','b','a'},...
              'independent','x',...
              'dependent','gaussx',...
              'options',ox);

gaussy = fittype('a+ b*exp(-(x-x0).^2./(2*s1.^2)) +
    c*exp(-(x-x02).^2./(2*s2.^2))',... %the 2-gaussian function used for
    fitting
              'coefficients',{'x0','s1','b','a','x02','s2','c'},...
```

```
            'independent','x',...
            'dependent','gaussy',...
            'options',oy);


fitx = fit(x1D,xprofile,gaussx); %fit the data to the gaussian model
fity = fit(y1D,yprofile,gaussy);

f1Dx = coeffvalues(fitx); %extract the coefficients form the fit data
f1Dy = coeffvalues(fity);

%%%%%%%%%%%%%%%%%%%%%%%%%%%%%%%%%%%%%%%%%%%%%%%%%%%%%%%%%%%%
end
```

E.4 Gaussian2D_3

```
function [f1Dx,f1Dy,f2D] = Gaussian2D_3(m,tol)
%%%%%%%%%%%%%%%%%%%%%%%%%%%%%%%%%%%%%%%%%%%%%%%%%%%%%%%%%%%%
%% a function to fit a thermal atomic cloud to 2-D Gauss
%% m  : Image
%% tol: fitting tolerance
%% this is the subroutine will be used to fit bining optical density
%% in order to improve the processing speed. Based on program from
%% http://jilawww.colorado.edu/bec/BEC_for_everyone/
%% Last modified by Dajun Wang @10/11/2005

%modified by Ryan Carollo to change width definition to a standard
%deviation on 27-Jan-2009

%rewritten by Ryan Carollo to use methods form the Curve Fitting Toolbox
%that are much more straightforward and user-friendly on 18-Nov-2009

%the vertical offset has been clamped to zero
%%%%%%%%%%%%%%%%%%%%%%%%%%%%%%%%%%%%%%%%%%%%%%%%%%%%%%%%%%%%

[f1Dx, f1Dy] = Gaussian1D_3(m,tol); %call the external version rather than
    rewriting here

    function [x1D, y1D, z1D] = imagevector(image)
        %The point of this function is to create three vectors representing
        %x and y points, along with the corresponing pixel values
        % (z values) from the image, in the format that Matlab wants for a
        %surface fit.
        [sizey sizex] = size(image);
        x = 1:sizex;
        y = (1:sizey)';
        horiz = ones(1,sizex);
        vert = ones(sizey,1);
        xdat = vert*x;
        ydat = y*horiz;
```

```
        x1D = xdat(:);
        y1D = ydat(:);
        z1D = image(:);

    end %imagevector

[sizey sizex] = size(m);

x0 = f1Dx(1); %these will be initial parameters for the 2D fit
sx = f1Dx(2);
bx = f1Dx(3);
ax = f1Dx(4);

y0 = f1Dy(1);
sy = f1Dy(2);
by = f1Dy(3);
ay = f1Dy(4);

a = (ax./(sizey-1) + ay./(sizex-1))/2; %'a' has been integrated over the image,
     so divide by the length of each dimension, then average
b = (bx./sy + by./sx)./(2*sqrt(2*pi)); % 'b' can be extracted from the
    integrated data that was fit, then averaged between the two fits

o = fitoptions('Method','NonlinearLeastSquares',...
                  'Algorithm','Trust-Region',...
                  'StartPoint',[x0,y0,sx,sy,b,a,0],...    %initial guesses for
                      fitted x coefficients
                  'Lower',[0,0,0,0,0,0,-Inf],...          %prevent negative
                      values
                  'Upper',[Inf,Inf,Inf,Inf,Inf,Inf,Inf],...
                  'TolFun',tol,...
                  'MaxFunEvals',1000,'MaxIter',1000);

%rotated_gaussian = a+b*exp(-((x-x0)*cos(t)+(y-y0)*sin(t))^2/(2*s1^2)-((y-y0)*
    cos(t)-(x-x0)*sin(t))^2/(2*s2^2));
    %this model fits a 2D gaussian whose axes have been rotated (by a
    %rotation matrix) by an angle 't'

gauss2 = fittype('a+b*exp(-((x-x0)*cos(t)+(y-y0)*sin(t))^2/(2*s1^2)-((y-y0)*cos
    (t)-(x-x0)*sin(t))^2/(2*s2^2))',...
              'coefficients',{'x0','y0','s1','s2','b','a','t'},...
              'independent',{'x','y'},...
              'dependent','gaussx',...
              'options',o);

[x1D, y1D, z1D] = imagevector(m);

fit2D = fit([x1D,y1D],z1D,gauss2); %fit the data to our 2D gaussian

f2D = coeffvalues(fit2D); %extract the coefficients from the fit data
```

```
end
```

E.5 Gaussian2D_3a

```
function [f1Dx,f1Dy,f2D] = Gaussian2D_3a(m,tol)
%%%%%%%%%%%%%%%%%%%%%%%%%%%%%%%%%%%%%%%%%%%%%%%%%%%%%%%%%%%%%%%%%%%%
%% a function to fit a thermal atomic cloud to 2-D Gauss
%% m  : Image
%% tol: fitting tolerance
%% this is the subroutine will be used to fit bining optical density
%% in order to improve the processing speed. Based on program from
%% http://jilawww.colorado.edu/bec/BEC_for_everyone/
%% Last modified by Dajun Wang @10/11/2005

%modified by Ryan Carollo to change width definition to a standard
%deviation on 27-Jan-2009

%rewritten by Ryan Carollo to use methods form the Curve Fitting Toolbox
%that are much more straightforward and user-friendly on 18-Nov-2009

%this variant on Gaussian2D will fit two gaussians, so as to fit both the
%MOT and the CO2trap simultaneously

%the vertical offset has been clamped to zero
%%%%%%%%%%%%%%%%%%%%%%%%%%%%%%%%%%%%%%%%%%%%%%%%%%%%%%%%%%%%%%%%%%%%

[f1Dx, f1Dy] = Gaussian1D_3a(m,tol); %call the external version rather than
    rewriting here

    function [x1D, y1D, z1D] = imagevector(image)
        %The point of this function is to create three vectors representing
        %x and y points, along with the corresponing pixel values
        %(z values) from the image, in the format that Matlab wants for a
        %surface fit.
        [sizey sizex] = size(image);
        x = 1:sizex;
        y = (1:sizey)';
        horiz = ones(1,sizex);
        vert = ones(sizey,1);
        xdat = vert*x;
        ydat = y*horiz;
        x1D = xdat(:);
        y1D = ydat(:);
        z1D = image(:);

    end %imagevector

[sizey sizex] = size(m);
```

```
x0 = f1Dx(1); %these will be initial parameters for the 2D fit
sx1 = f1Dx(2);
bx = f1Dx(3);
ax = f1Dx(4);
%x02 = f1Dx(5);
%sx2 = f1Dx(6);
%cx = f1Dx(7);
x02 = x0;
sx2 = sx1;



y0 = f1Dy(1);
sy1 = f1Dy(2);
by = f1Dy(3);
ay = f1Dy(4);
y02 = f1Dy(5);
sy2 = f1Dy(6);
cy = f1Dy(7);

a = (ax./(sizey-1) + ay./(sizex-1))/2; %'a' has been integrated over the image
    , so divide by the length of each dimension, then average
b = (bx./sy1 + by./sx1)./(2*sqrt(2*pi)); %'b' can be extracted from the
    integrated data that was fit, then averaged between the two fits
%c = (cx./sy2 + cy./sx2)./(2*sqrt(2*pi)); %average the two 'c' values together
    as with 'b' above
c = cy./(sx2.*sqrt(2*pi));              %extract the value 'c' as with 'b'
    above, but only from the y value

o = fitoptions('Method','NonlinearLeastSquares',...
                  'Algorithm','Trust-Region',...
                  'StartPoint',[x0,y0,sx1,sy1,b,a,0,x02,y02,sx2,sy2,c,0],... %
                      initial guesses for fitted x coefficients
                  'Lower',[-Inf,-Inf,0,0,0,0,-Inf,-Inf,-Inf,0,0,0,-Inf],... %
                      prevent negative values in width and scaling
                  'Upper',[Inf,Inf,sizex,sizey,2*b,Inf,Inf,Inf,Inf,sizex,50,2*c
                      ,Inf],... %keep the fit from wandering off
                  'TolFun',tol,...
                  'MaxFunEvals',1000,'MaxIter',1000);

%rotated_gaussian = a+b*exp(-((x-x0)*cos(t)+(y-y0)*sin(t))^2/(2*s1^2)-((y-y0)*
    cos(t)-(x-x0)*sin(t))^2/(2*s2^2))...
%                  +c*exp(-((x-x02)*cos(t)+(y-y02)*sin(t))^2/(2*s3^2)-((y-y02)*
    cos(t)-(x-x02)*sin(t))^2/(2*s4^2));
    %this model fits a 2D gaussian whose axes have been rotated (by a
    %rotation matrix) by an angle 't'

gauss2 = fittype('a+b*exp(-((x-x0)*cos(t)+(y-y0)*sin(t))^2/(2*s1^2)-((y-y0)*cos
    (t)-(x-x0)*sin(t))^2/(2*s2^2))+c*exp(-((x-x02)*cos(t2)+(y-y02)*sin(t2))
    ^2/(2*s3^2)-((y-y02)*cos(t2)-(x-x02)*sin(t2))^2/(2*s4^2))',...
```

```
                'coefficients',{'x0','y0','s1','s2','b','a','t','x02','y02','s3
                    ','s4','c','t2'},...
                'independent',{'x','y'},...
                'dependent','gauss2',...
                'options',o);

[x1D, y1D, z1D] = imagevector(m);

fit2D = fit([x1D,y1D],z1D,gauss2); %fit the data to the 2 2D gaussians

f2D = coeffvalues(fit2D); %extract the coefficients from the fit data

end
```

E.6 SmoothOD2

```
function [iOD,iabs] = smoothOD2(img1,img2,img3)
%%%%%%%%%%%%%%%%%%%%%%%%%%%%%%%%%%%%%%%%%%%%%%%%%%%%%%%%%%%%%%%%%%%%
%% subroutine to smooth image and get the Optical Density smoothed
%% The input are three image matrics
%% The absorption should be iabs = (img1-img3)/(img2-img3)
%% iOD: image of in term of optical density
%%%%%%%%%%%%%%%%%%%%%%%%%%%%%%%%%%%%%%%%%%%%%%%%%%%%%%%%%%%%%%%%%%%%

iatom=im2double(imsubtract(img1,img3));
iprobe=im2double(imsubtract(img2,img3));

%save('probe_000.mat','iprobe');

[sizex, sizey] = size(iatom);

%% get rid of pixel of bad values (Inf and 0) before calculating absorption
%% image
for m= 1:sizex
    for n= 1: sizey
        if iatom(m,n)==Inf
            iatom(m,n)=1;
        end
        if iprobe(m,n)==Inf
            iprobe(m,n)=1;
        end
    end
end
for m= 1:sizex
    for n= 1: sizey
        if iatom(m,n)==0
            iatom(m,n)=0.00001;
            %iabs(m,n)=(iabs(m+1,n+1)+iabs(m-1,n-1)+iabs(m+1,n)+iabs(m-1,n)+iabs
                (m,n+1)+iabs(m,n-1)+iabs(m+1,n-1)+iabs(m-1,n+1))/8;
        end
```

```
        if iprobe(m,n)==0;
            iprobe(m,n)=0.00001;
        end
    end
end

%calculate the absorption image
iabs=imdivide(iatom,iprobe);

%imwrite(iabs,'iabs.tif');
%iabs=im2double(iabs);

%output the absorption image
%save('absorption_000.mat','iabs');

%% calculate Optical Density
%for ii=1:60
%   iabs(ii,:)=[];
%end
iOD = -log(iabs);

[sizex, sizey] = size(iabs);

%% get rid of bad optical density points (<0) y columns
badcolumnsizey = 0;
badcolumny(1,1)=1;
for n= 1:sizey
    if sum(iOD(:,n))<0
       badcolumny(1,badcolumnsizey+1)=n;
       [badcolumnsizex,badcolumnsizey]=size(badcolumny);
    end
end
iOD(:,badcolumny)=[];
iabs(:,badcolumny)=[];

%% get rid of bad optical density points (<0) x row
badcolumnsizex = 0;
badcolumnx(1,1)=1;
for n= 1:sizex
    if sum(iOD(n,:))<0
       badcolumnx(1,badcolumnsizex+1)=n;
       [badcolumnsizex,badcolumnsizey]=size(badcolumnx);
   end
end
iOD(badcolumnx,:)=[];
iabs(badcolumnx,:)=[];

[sizex, sizey] = size(iabs);

thresholdOD1 = 1;
```

```
for m= 2:sizex-1
    for n= 2: sizey-1
        if abs(iOD(m,n)-iOD(m+1,n+1))>thresholdOD1|abs(iOD(m,n)-iOD(m-1,n-1))>
            thresholdOD1|abs(iOD(m,n)-iOD(m+1,n))>thresholdOD1|abs(iOD(m,n)-iOD(
            m-1,n))>thresholdOD1|abs(iOD(m,n)-iOD(m,n+1))>thresholdOD1|abs(iOD(m
            ,n)-iOD(m,n-1))>thresholdOD1|abs(iOD(m,n)-iOD(m+1,n-1))>thresholdOD1
            |abs(iOD(m,n)-iOD(m-1,n+1))>thresholdOD1
            iOD(m,n)=(iOD(m+1,n+1)+iOD(m-1,n-1)+iOD(m+1,n)+iOD(m-1,n)+iOD(m,n+1)
                +iOD(m,n-1)+iOD(m+1,n-1)+iOD(m-1,n+1))/8;
            %iabs(m,n)=(iabs(m+1,n+1)+iabs(m-1,n-1)+iabs(m+1,n)+iabs(m-1,n)+iabs
                (m,n+1)+iabs(m,n-1)+iabs(m+1,n-1)+iabs(m-1,n+1))/8;
        end
    end
end

%% smooth again using lower threshold
thresholdOD2 = 0.3;
for m= 2:sizex-1
    for n= 2: sizey-1
        if abs(iOD(m,n)-iOD(m+1,n+1))>thresholdOD2|abs(iOD(m,n)-iOD(m-1,n-1))>
            thresholdOD2|abs(iOD(m,n)-iOD(m+1,n))>thresholdOD2|abs(iOD(m,n)-iOD(
            m-1,n))>thresholdOD2|abs(iOD(m,n)-iOD(m,n+1))>thresholdOD2|abs(iOD(m
            ,n)-iOD(m,n-1))>thresholdOD2|abs(iOD(m,n)-iOD(m+1,n-1))>thresholdOD2
            |abs(iOD(m,n)-iOD(m-1,n+1))>thresholdOD2
            iOD(m,n)=(iOD(m+1,n+1)+iOD(m-1,n-1)+iOD(m+1,n)+iOD(m-1,n)+iOD(m,n+1)
                +iOD(m,n-1)+iOD(m+1,n-1)+iOD(m-1,n+1))/8;
            %iabs(m,n)=(iabs(m+1,n+1)+iabs(m-1,n-1)+iabs(m+1,n)+iabs(m-1,n)+iabs
                (m,n+1)+iabs(m,n-1)+iabs(m+1,n-1)+iabs(m-1,n+1))/8;
        end
    end
end
%figure, imshow(iabs);colormap(jet(16));
```

E.7 atomDensity2

```
function [atomNumber, atomPeakDensity] = atomDensity2(width_x,width_y,peakOD)
%%%%%%%%%%%%%%%%%%%%%%%%%%%%%%%%%%%%%%%%%%%%%%%%%%%%%%%%%%%%%%%%%%%%%%%%%%%%
%% subroutine to calculate the atom density and number
%% width_x: x direction size from the 2D Gauss fit
%% width_y: y direction size from the 2D Gauss fit
%% peakOD : peak Optical Density get from the 2D Gauss fit. It is actuall
%%         the fitted peak_OD+offset here
%%%%%%%%%%%%%%%%%%%%%%%%%%%%%%%%%%%%%%%%%%%%%%%%%%%%%%%%%%%%%%%%%%%%%%%%%%%%

%% the optical magnification in (pixels/cm)
%% this is a estimation value for now
%% for camera one is 103 pixels/mm, for camera two the optical
%% magnification compared with one is 1.897. so the on screen magnification
%% of camrea two is in pixels/cm
```

```
%As of 3/9/09, the pixel pitch was changed to 7.4 microns with a
%mignification of 1.72, giving 2324.32 pixels/cm

pitch = 7.4*10^(-6); %pixel pitch
magnification = 1.72; %physical size of image is greater than object size
                      %by this factor
opticalM = magnification/(100*pitch); %pixels per cm

%% calculate resonance scattering cross section a0=3*Lambda^2*aTranS/(2pi)
%% where Lambda is the transition wavelength (in cm), p is the average
%% transition strength
%% for 85Rb
Lambda = 780.24*10^(-7);
tStrength = 28/135;
a0 = 3*tStrength*Lambda^2/(2*pi);

%% atom number
atomNumber = pi*2*width_x*width_y*peakOD/(opticalM^2*a0);

%% peak density, assume the z direction has the same size as y direction.
atomPeakDensity = atomNumber*opticalM^3/((2^1.5)*(width_y^2)*width_x*pi^(1.5));
```

E.8 plotGaussian_3

```
function fitOD = plotGaussian_3(f1Dx,f1Dy,m,f2D,residual)
%%%%%%%%%%%%%%%%%%%%%%%%%%%%%%%%%%%%%%%%%%%%%%%%%%%%%%%%%%%%
%% cx:
%% cy:
%% sx:
%% sy:
%% peakOD:
%% offsetx:
%% offsety:
%% m: the image to get the fit size here
%% using the above fitting parameters to generate the fitted image
%% 0.5*offsety+0.5*offsetx+peakOD*(exp(-(X-cx).^2./(sx^2)-(Y-cy).^2./(sy^2)))
%% for one direction, use the 1D format
%% offsetx+peakOD*exp(-(x-cx)/sx)^2;

%modified 27-Jan-2009 to reflect new width definition

%modified 18-Nov-2009 to match naming conventions of new imageAtoms3
%version and to change the way 1D fits are done
%%%%%%%%%%%%%%%%%%%%%%%%%%%%%%%%%%%%%%%%%%%%%%%%%%%%%%%%%%%%

[sizey sizex] = size(m);


%%%%%NOTE%%%%%
%The cy, cx below are extracted from the final fit data and are NOT the
```

```
%same cy, cx used to select the data to be fit in Gaussuan1D_3. We may want
%to change this behavior.
%%%%%%%%%%%%%%
xprofile = sum(m);         %adds all y-values for each x-value, giving summed x
     cross section, averaging by number of pixles
x1D = 1:sizex;
%% plot the fited curve out to compare
x = x1D;
x0 = f1Dx(1);
sx = f1Dx(2);
bx = f1Dx(3);
ax = f1Dx(4);


subplot(2,3,4),plot(x,xprofile),title('x direction');
hold on
plot(x, ax+bx*exp(-(x-x0).^2./(2*sx^2)), 'color', 'red');
axis tight;
hold off


yprofile = sum(m');        %adds all x-values for each y-value, giving summed y
     cross section
y1D = 1:sizey;
%% plot the fited curve out to compare
y=y1D;
y0 = f1Dy(1);
sy = f1Dy(2);
by = f1Dy(3);
ay = f1Dy(4);

subplot(2,3,2),plot(yprofile,y),title('y direction')
hold on
plot(ay+by*exp(-(y-y0).^2./(2*sy^2)), y, 'color', 'red')
axis tight;
set(gca,'YDir','reverse');
hold off

%% plot 2D fitted cloud
if (nargin==4)
    [X,Y] = meshgrid(1:sizex,1:sizey);

    x0 = f2D(1);
    y0 = f2D(2);
    s1 = f2D(3);
    s2 = f2D(4);
    b = f2D(5);
    a = f2D(6);
    t = f2D(7);
```

```
    for iii=1:sizex
        for jjj=1:sizey
            %mm(jjj,iii)=0.5*fp2D(7)+0.5*fp2D(6)+fp2D(5)*(exp(-(iii-fp2D(1))
                .^2./(fp2D(3)^2)-(jjj-fp2D(2)).^2./(fp2D(4)^2)));
            mm(jjj,iii) = a+b*exp(-((iii-x0)*cos(t)+(jjj-y0)*sin(t))^2/(2*s1^2)
                -((jjj-y0)*cos(t)-(iii-x0)*sin(t))^2/(2*s2^2));
        end
    end
    %figure;surf(mm); shading interp;
    %mm=m-mm;
    mm = 1-exp(-mm);
    %subplot(2,3,5);surf(mm); axis on; title('fit'); shading interp;
    subplot(2,3,5);imshow(mm); axis on; title('2D fit'); colormap(jet(256));
end

%% plot 2D fit residual instead
if (nargin>4)
    [X,Y] = meshgrid(1:sizex,1:sizey);

    x0 = f2D(1);
    y0 = f2D(2);
    s1 = f2D(3);
    s2 = f2D(4);
    b = f2D(5);
    a = f2D(6);
    t = f2D(7);

    for iii=1:sizex
        for jjj=1:sizey
            %mm(jjj,iii)=0.5*fp2D(7)+0.5*fp2D(6)+fp2D(5)*(exp(-(iii-fp2D(1))
                .^2./(2*fp2D(3)^2)-(jjj-fp2D(2)).^2./(fp2D(4)^2)));
            mm(jjj,iii) = a+b*exp(-((iii-x0)*cos(t)+(jjj-y0)*sin(t))^2/(2*s1^2)
                -((jjj-y0)*cos(t)-(iii-x0)*sin(t))^2/(2*s2^2));

        end
    end
    %figure;surf(mm); shading interp;
    mm=m-mm;
    %mm = 1-exp(-mm);
    leftover = sum(sum(mm))/sum(sum(m));
    leftover = num2str(leftover,'%10.4e');
    thetitle = strcat('residual', ' = ', leftover);
    subplot(2,3,5);imshow(mm); axis on; title(thetitle); colormap(jet(256));
end
```

E.9 plotGaussian_3a

```
function fitOD = plotGaussian_3a(f1Dx,f1Dy,m,f2D,residual)
%%%%%%%%%%%%%%%%%%%%%%%%%%%%%%%%%%%%%%%%%%%%%%%%%%%%%%%%%%%%
%% cx:
```

```
%% cy:
%% sx:
%% sy:
%% peakOD:
%% offsetx:
%% offsety:
%% m: the image to get the fit size here
%% using the above fitting parameters to generate the fitted image
%% 0.5*offsety+0.5*offsetx+peakOD*(exp(-(X-cx).^2./(sx^2)-(Y-cy).^2./(sy^2)))
%% for one direction, use the 1D format
%% offsetx+peakOD*exp(-(x-cx)/sx)^2;

%modified 27-Jan-2009 to reflect new width definition

%modified 18-Nov-2009 to improve readability and match naming conventions of
%new imageAtoms3 version and to change the way 1D fits are done

%the 3a variant is to fit two linearly added gaussians simultaneously
%%%%%%%%%%%%%%%%%%%%%%%%%%%%%%%%%%%%%%%%%%%%%%%%%%%%%%%%%%%%%%%%%%%

[sizey sizex] = size(m);

xprofile = sum(m);         %adds all y-values for each x-value, giving summed x
     cross section
x1D = 1:sizex;
%% plot the fited curve out to compare
x = x1D;
x0 = f1Dx(1);
sx = f1Dx(2);
bx = f1Dx(3);
ax = f1Dx(4);
%x02 = f1Dx(5);
%sx2 = f1Dx(6);
%cx = f1Dx(7);


subplot(2,3,4),plot(x,xprofile),title('x direction');
hold on
%plot(x, ax+bx*exp(-(x-x0).^2./(2*sx^2))+cx*exp(-(x-x02).^2./(2*sx2^2)), 'color
    ', 'red'); %two superimposed gaussians
plot(x, ax+bx*exp(-(x-x0).^2./(2*sx^2)), 'color', 'red'); %we are only fitting
    one gaussian in the x-direction
axis tight;
axis tight;
hold off

yprofile = sum(m');        %adds all x-values for each y-value, giving summed y
     cross section
y1D = 1:sizey;
%% plot the fited curve out to compare
```

```
y=y1D;
y0 = f1Dy(1);
sy = f1Dy(2);
by = f1Dy(3);
ay = f1Dy(4);
y02 = f1Dy(5);
sy2 = f1Dy(6);
cy = f1Dy(7);

subplot(2,3,2),plot(yprofile,y),title('y direction')
hold on
plot(ay+by*exp(-(y-y0).^2./(2*sy^2))+cy*exp(-(y-y02).^2./(2*sy2^2)), y, 'color
    ', 'red') %two superimposed gaussians
axis tight;
set(gca,'YDir','reverse');
hold off

%% plot 2D fitted cloud
if (nargin==4)
    [X,Y] = meshgrid(1:sizex,1:sizey);

    x0 = f2D(1);
    y0 = f2D(2);
    s1 = f2D(3);
    s2 = f2D(4);
    b = f2D(5);
    a = f2D(6);
    t = f2D(7);
    x02 = f2D(8);
    y02 = f2D(9);
    s3 = f2D(10);
    s4 = f2D(11);
    c = f2D(12);
    t2 = f2D(13);

    for iii=1:sizex
        for jjj=1:sizey
            %mm(jjj,iii)=0.5*fp2D(7)+0.5*fp2D(6)+fp2D(5)*(exp(-(iii-fp2D(1))
                .^2./(fp2D(3)^2)-(jjj-fp2D(2)).^2./(fp2D(4)^2)));
            mm(jjj,iii) = a+b*exp(-((iii-x0)*cos(t)+(jjj-y0)*sin(t))^2/(2*s1^2)
                -((jjj-y0)*cos(t)-(iii-x0)*sin(t))^2/(2*s2^2))+c*exp(-((iii-x02)
                *cos(t2)+(jjj-y02)*sin(t2))^2/(2*s3^2)-((jjj-y02)*cos(t2)-(iii-
                x02)*sin(t2))^2/(2*s4^2));
        end
    end
    %figure;surf(mm); shading interp;
    %mm=m-mm;
    mm = 1-exp(-mm);
    %subplot(2,3,5);surf(mm); axis on; title('fit'); shading interp;
    subplot(2,3,5);imshow(mm); axis on; title('2D fit'); colormap(jet(256));
```

```
end

%% plot 2D fit residual instead
if (nargin>4)
    [X,Y] = meshgrid(1:sizex,1:sizey);

    x0 = f2D(1);
    y0 = f2D(2);
    s1 = f2D(3);
    s2 = f2D(4);
    b = f2D(5);
    a = f2D(6);
    t = f2D(7);
    x02 = f2D(8);
    y02 = f2D(9);
    s3 = f2D(10);
    s4 = f2D(11);
    c = f2D(12);
    t2 = f2D(13);

    for iii=1:sizex
        for jjj=1:sizey
            %mm(jjj,iii)=0.5*fp2D(7)+0.5*fp2D(6)+fp2D(5)*(exp(-(iii-fp2D(1))
                .^2./(2*fp2D(3)^2)-(jjj-fp2D(2)).^2./(fp2D(4)^2)));
            mm(jjj,iii) = a+b*exp(-((iii-x0)*cos(t)+(jjj-y0)*sin(t))^2/(2*s1^2)
                -((jjj-y0)*cos(t)-(iii-x0)*sin(t))^2/(2*s2^2))+c*exp(-((iii-x02)
                *cos(t2)+(jjj-y02)*sin(t2))^2/(2*s3^2)-((jjj-y02)*cos(t2)-(iii-
                x02)*sin(t2))^2/(2*s4^2));

        end
    end
    %figure;surf(mm); shading interp;
    mm=m-mm;
    %mm = 1-exp(-mm);
    leftover = sum(sum(mm))/sum(sum(m));
    leftover = num2str(leftover,'%10.4e');
    thetitle = strcat('residual', ' = ', leftover);
    subplot(2,3,5);imshow(mm); axis on; title(thetitle); colormap(jet(256));
end
```

E.10 temp_fit3

```
function [temperature, gof, output] = temp_fit3(t_width)

%Using the standard ballistic expansion model in size.m, this script will
%estimate the temperature T in microkelvin. The parameter t_width is a 2xN
%matrix containing times in the first row and cloud diameters in the second
%row. Enter the matrix in the Command Window. It should look like
%x=[1 2 3; 112 245 362]. Then call this program by typing "temp_fit3(x)".;
```

```
%As of 3/9/09, the pixel pitch was changed to 7.4 microns with a
%mignification of 1.72, giving 232432 pixels/m

clf('reset')          %clear figure window so as to not overwrite
                      %  previous plots/data

pitch = 7.4*10^(-6);  %pixel pitch
magnification = 1.72; %physical size of image is greater than object size
                      %  by this factor
opticalM = magnification/pitch; %pixels per m

amu = 1.66053886.*10.^(-27);     %atomic mass unit
M = 84.9117893.*amu;             %atomic mass of Rb85
Kb = 1.3806503.*10.^(-23);       %SI Boltzmann constant

t = t_width(1,:)';               %time values, in milliseconds, as a column
    vector
width = t_width(2,:)'./opticalM; %diamter of cloud, in meters (entered in
    pixels),
                                 %  also a column vector

%diam = width(1); %size of first data point, in meters
diam = t_width(2,1);  %size of first data point, in pixels

o = fitoptions('Method','NonlinearLeastSquares',...
                  'Algorithm','Trust-Region',...
                  'Lower',[0,0],...
                  'Upper',[Inf,1000],...
                  'StartPoint',[diam,60],...      %initial guesses for fitted
                      coefficients
                  'TolFun',10^(-20),'TolX',10^(-20),...
                  'MaxFunEvals',1000,'MaxIter',1000);


diameter = fittype('sqrt((a./z).^2 +
    ((k./m).*T.*10.^(-6)).*(t.*10.^(-3)).^2)',... %fitting function definition
                  'coefficients',{'a','T'},...    %fitted coefficients
                  'dependent','diameter',...
                  'independent','t',...
                  'problem',{'k','m','z'},...         %unfitted coefficients
                  'options',o);

%coeffnames(diameter)    %lists the coefficient names in the order they
                         %must be used in for Upper and Lower
%probnames(diameter)     %list preoblem-dependent parameters in order

[temperature, gof, output] = fit(t,width,diameter,'problem',{Kb,M,opticalM});
    %the fit itself

gof;
```

```
output; %these values display data about the goodness of fit and fitting
    algorithm
        %they may be used to determine the quality of the fit coefficients

plot(temperature,t,width)

end
```

Bibliography

[1] E. L. Raab, M. Prentiss, Alex Cable, Steven Chu, and D. E. Pritchard. Trapping of neutral sodium atoms with radiation pressure. *Phys. Rev. Lett.*, 59:2631–2634, December 1987.

[2] Nobel Prize Committee. Nobelprize.org press release. `http://www.nobelprize.org/nobel_prizes/physics/laureates/1997/press.html`, October 1997. Accessed 5-18-2015.

[3] Harold J. Metcalf and Peter van der Straten. *Laser Cooling and Trapping*. Springer, 1999.

[4] Steven Chu, L. Hollberg, J. E. Bjorkholm, Alex Cable, and A. Ashkin. Three-dimensional viscous confinement and cooling of atoms by resonance radiation pressure. *Phys. Rev. Lett.*, 55:48–51, July 1985.

[5] M. H. Anderson, J. R. Ensher, M. R. Matthews, C. E. Wieman, and E. A. Cornell. Observation of Bose-Einstein condensation in a dilute atomic vapor. *Science*, 269(5221):198–201, 1995.

[6] K. B. Davis, M. O. Mewes, M. R. Andrews, N. J. van Druten, D. S. Durfee, D. M. Kurn, and W. Ketterle. Bose-Einstein condensation in a gas of sodium atoms. *Phys. Rev. Lett.*, 75:3969–3973, November 1995.

[7] U. Gaubatz, P. Rudecki, S. Schiemann, and K. Bergmann. Population transfer between molecular vibrational levels by stimulated Raman scattering with partially overlapping laser fields. A new concept and experimental results. *The Journal of Chemical Physics*, 92(9):5363–5376, 1990.

[8] K.-K. Ni, S. Ospelkaus, M. H. G. de Miranda, A. Pe'er, B. Neyenhuis, J. J. Zirbel, S. Kotochigova, P. S. Julienne, D. S. Jin, and J. Ye. A high phase-space-density gas of polar molecules. *Science*, 322(5899):231–235, 2008.

[9] F. Lang, K. Winkler, C. Strauss, R. Grimm, and J. Hecker Denschlag. Ultracold triplet molecules in the rovibrational ground state. *Phys. Rev. Lett.*, 101:133005, September 2008.

[10] S. E. Maxwell, N. Brahms, R. deCarvalho, D. R. Glenn, J. S. Helton, S. V. Nguyen, D. Patterson, J. Petricka, D. DeMille, and J. M. Doyle. High-flux beam source for cold, slow atoms or molecules. *Phys. Rev. Lett.*, 95:173201, October 2005.

[11] S. Charles Doret, Colin B. Connolly, Wolfgang Ketterle, and John M. Doyle. Buffer-gas cooled Bose-Einstein condensate. *Phys. Rev. Lett.*, 103:103005, September 2009.

[12] Hendrick L. Bethlem, Giel Berden, and Gerard Meijer. Decelerating neutral dipolar molecules. *Phys. Rev. Lett.*, 83:1558–1561, August 1999.

[13] F. Lang, K. Winkler, C. Strauss, R. Grimm, and J. Hecker Denschlag. Ultracold triplet molecules in the rovibrational ground state. *Phys. Rev. Lett.*, 101:133005, September 2008.

[14] E. S. Shuman, J. F. Barry, and D. DeMille. Laser cooling of a diatomic molecule. *Nature*, 467(7317):820–823, October 2010.

[15] Matthew T. Hummon, Mark Yeo, Benjamin K. Stuhl, Alejandra L. Collopy, Yong Xia, and Jun Ye. 2D magneto-optical trapping of diatomic molecules. *Phys. Rev. Lett.*, 110:143001, Apr 2013.

[16] J. F. Barry, D. J. McCarron, E. B. Norrgard, M. H. Steinecker, and D. DeMille. Magneto-optical trapping of a diatomic molecule. *Nature*, 512(7514):286–289, August 2014.

[17] H. R. Thorsheim, J. Weiner, and P. S. Julienne. Laser-induced photoassociation of ultracold sodium atoms. *Phys. Rev. Lett.*, 58:2420–2423, June 1987.

[18] P. D. Lett, P. S. Julienne, and W. D. Phillips. Photoassociative spectroscopy of laser-cooled atoms. *Annual Review of Physical Chemistry*, 46(1):423–452, 1995. PMID: 24329894.

[19] William C. Stwalley and He Wang. Photoassociation of ultracold atoms: A new spectroscopic technique. *J. Mol. Spectrosc.*, 195(2):194 – 228, 1999.

[20] Kevin M. Jones, Eite Tiesinga, Paul D. Lett, and Paul S. Julienne. Ultracold photoassociation spectroscopy: Long-range molecules and atomic scattering. *Rev. Mod. Phys.*, 78:483–535, May 2006.

[21] P Pillet, A Crubellier, A Bleton, O Dulieu, P Nosbaum, I Mourachko, and F Masnou-Seeuws. Photoassociation in a gas of cold alkali atoms: I. Perturbative quantum approach. *Journal of Physics B: Atomic, Molecular and Optical Physics*, 30(12):2801, 1997.

[22] D. Wang, J. Qi, M.F. Stone, O. Nikolayeva, B. Hattaway, S.D. Gensemer, H. Wang, W.T. Zemke, P.L. Gould, E.E. Eyler, and W.C. Stwalley. The photoassociative spectroscopy, photoassociative molecule formation, and trapping of ultracold $^{39}K^{85}Rb$. *The European Physical Journal D - Atomic, Molecular, Optical and Plasma Physics*, 31(2):165–177, 2004.

[23] Jayita Banerjee, David Rahmlow, Ryan Carollo, Michael Bellos, Edward E. Eyler, Phillip L. Gould, and William C. Stwalley. Direct photoassociative formation of ultracold KRb molecules in the lowest vibrational levels of the electronic ground state. *Phys. Rev. A*, 86:053428, November 2012.

[24] V. Sanchez-Villicana, S. D. Gensemer, K. Y. N. Tan, A. Kumarakrishnan, T. P. Dinneen, W. Süptitz, and P. L. Gould. Suppression of ultracold ground-state hyperfine-changing collisions with laser light. *Phys. Rev. Lett.*, 74:4619–4622, June 1995.

[25] John Brown and Alan Carrington. *Rotational Spectroscopy of Diatomic Molecules*. Cambridge University Press, 2003.

[26] Hélène Lefebvre-Brion and Robert W. Field. *The Spectra and Dynamics of Diatomic Molecules*. Elsevier Academic Press, 2004.

[27] Gerhard Herzberg. *Molecular Spectra and Molecular Structure: I. Spectra of Diatomic Molecules*. D. Van Nostrand Company, Inc., 1950.

[28] C. C. Tsai, R. S. Freeland, J. M. Vogels, H. M. J. M. Boesten, B. J. Verhaar, and D. J. Heinzen. Two-color photoassociation spectroscopy of ground state Rb_2. *Phys. Rev. Lett.*, 79:1245–1248, August 1997.

[29] C. Strauss, T. Takekoshi, F. Lang, K. Winkler, R. Grimm, J. Hecker Denschlag, and E. Tiemann. Hyperfine, rotational, and vibrational structure of the $a\,^3\Sigma_u^+$ state of $^{87}Rb_2$. *Phys. Rev. A*, 82:052514, November 2010.

[30] Peter F. Bernath. *Spectra of Atoms and Molecules*. Oxford University Press, 2005.

[31] R. J. Le Roy. *LEVEL 8.0: A Computer Program for Solving the Radial Schrödinger Equation for Bound and Quasibound Levels*. University of Waterloo Chemical Physics Research Report CP-663, 2007. see http://scienide2.uwaterloo.ca/%7erleroy/level/.

[32] R. J. Le Roy. *LEVEL 8.2: A Computer Program for Solving the Radial Schrödinger Equation for Bound and Quasibound Levels*. University of Waterloo Chemical Physics Research Report CP-663, 2014. see http://scienide2.uwaterloo.ca/%7erleroy/level/.

[33] William C. Stwalley, Michael Bellos, Ryan Carollo, Jayita Banerjee, and Matthew Bermudez. Shortcuts for understanding rovibronic spectroscopy of ultracold alkali metal diatomic molecules. *Molecular Physics*, 110(15-16):1739–1755, April 2012.

[34] Y. Huang. *Production, Detection, and Trapping of Ultracold Molecular Rubidium*. PhD thesis, University of Connecticut, 2006.

[35] M. N. R. Ashfold and J. D. Howe. Multiphoton spectroscopy of molecular species. *Annual Review of Physical Chemistry*, 45(1):57–82, 1994.

[36] R. Carollo, M. A. Bellos, D. Rahmlow, J. Banerjee, E. E. Eyler, P. L. Gould, and W. C. Stwalley. Observation and analysis of resonant coupling between nearly degenerate levels of the $2\,^1\Sigma_g^+$ and $1\,^1\Pi_g$ states of ultracold $^{85}Rb_2$. *Phys. Rev. A*, 87:022505, February 2013.

[37] M. A. Bellos, R. Carollo, D. Rahmlow, J. Banerjee, E. E. Eyler, P. L. Gould, and W. C. Stwalley. Photoassociation to the $2\,^1\Sigma_g^+$ state in ultracold $^{85}Rb_2$ in the presence of a shape resonance. *Phys. Rev. A*, 86:033407, September 2012.

[38] M. Bellos. *Short-Range Photoassociation and Trilobite-like States of Ultracold Rb_2*. PhD thesis, University of Connecticut, 2013.

[39] M. A. Bellos, D. Rahmlow, R. Carollo, J. Banerjee, O. Dulieu, A. Gerdes, E. E. Eyler, P. L. Gould, and W. C. Stwalley. Formation of ultracold Rb_2 molecules in the $v'' = 0$ level of the $a\,^3\Sigma_u^+$ state via blue-detuned photoassociation to the $1^3\Pi_g$ state. *Phys. Chem. Chem. Phys.*, 13:18880–18886, September 2011.

[40] M. A. Bellos, R. Carollo, J. Banerjee, E. E. Eyler, P. L. Gould, and W. C. Stwalley. Excitation of weakly bound molecules to trilobitelike Rydberg states. *Phys. Rev. Lett.*, 111:053001, July 2013.

[41] K. J. Weatherill, J. D. Pritchard, P. F. Griffin, U. Dammalapati, C. S. Adams, and E. Riis. A versatile and reliably reusable ultrahigh vacuum viewport. *Review of Scientific Instruments*, 80(2), 2009.

[42] S. N. Atutov, R. Calabrese, V. Guidi, B. Mai, A. G. Rudavets, E. Scansani, L. Tomassetti, V. Biancalana, A. Burchianti, C. Marinelli, E. Mariotti, L. Moi, and S. Veronesi. Fast and efficient loading of a Rb magneto-optical trap using light-induced atomic desorption. *Phys. Rev. A*, 67:053401, May 2003.

[43] J. Fortagh, A. Grossmann, T. W. Hänsch, and C. Zimmermann. Fast loading of a magneto-optical trap from a pulsed thermal source. *Journal of Applied Physics*, 84(12):6499–6501, 1998.

[44] Umakant D. Rapol, Ajay Wasan, and Vasant Natarajan. Loading of a Rb magneto-optic trap from a getter source. *Phys. Rev. A*, 64:023402, June 2001.

[45] Mary Frances Stone. Stabilized external-cavity diode lasers. Master's thesis, State University of New York at Stony Brook, 2001.

[46] Omur Sezerman and Garland Best. Accurate alignment preserves polarizarion. *Laser Focus World*, December 1997.

[47] H. K. Pechkis. *Ultracold Rb_2 Molecules: Formation, Detection and Trapping in an Optical Dipole Trap.* PhD thesis, University of Connecticut, 2010.

[48] D. A. Steck. Rubidium 85 line data. Revision 2.1.6, 2013. Available at http://steck.us/alkalidata/.

[49] Dick Stresau, Kevin L. Hunter, and Dietmar A. Fichter. Extending the limits for linear ion counting: An electron multiplier for high count rate mass spectrometry. In *Proceedings of the 40th ASMS Conference on Mass Spectrometry and Allied Topics*, 1992.

[50] N. Melikechi, S. Gangopadhyay, and E. E. Eyler. Phase dynamics in nanosecond pulsed dye laser amplification. *J. Opt. Soc. Am. B*, 11(12):2402–2411, December 1994.

[51] D. S. Bethune. Dye cell design for high-power low-divergence excimer-pumped dye lasers. *Appl. Opt.*, 20(11):1897–1899, June 1981.

[52] A. N. Nikolov, J. R. Ensher, E. E. Eyler, H. Wang, W. C. Stwalley, and P. L. Gould. Efficient production of ground-state potassium molecules at sub-mK temperatures by two-step photoassociation. *Phys. Rev. Lett.*, 84:246–249, January 2000.

[53] H. Lignier, A. Fioretti, R. Horchani, C. Drag, N. Bouloufa, M. Allegrini, O. Dulieu, L. Pruvost, P. Pillet, and D. Comparat. Deeply bound cold caesium molecules formed after 0_g^- resonant coupling. *Phys. Chem. Chem. Phys.*, 13:18910–18920, 2011.

[54] J. Deiglmayr, A. Grochola, M. Repp, K. Mörtlbauer, C. Glück, J. Lange, O. Dulieu, R. Wester, and M. Weidemüller. Formation of ultracold polar molecules in the rovibrational ground state. *Phys. Rev. Lett.*, 101:133004, Sep 2008.

[55] A. Wakim, P. Zabawa, M. Haruza, and N. P. Bigelow. Luminorefrigeration: vibrational cooling of NaCs. *Opt. Express*, 20(14):16083–16091, July 2012.

[56] N. Bouloufa-Maafa, M. Aymar, O. Dulieu, and C. Gabbanini. Formation of ultracold RbCs molecules by photoassociation. *Laser Physics*, 22:1502–1512, 2012.

[57] Colin Bruzewicz, Mattias Gustavsson, Toshihiko Shimasaki, and David DeMille. Continuous production of rovibrational ground state RbCs via photoassociation. *Bulletin of the American Physical Society*, 57(5):116, 2012.

[58] J. Lozeille, A. Fioretti, C. Gabbanini, Y. Huang, H.K. Pechkis, D. Wang, P.L. Gould, E.E. Eyler, W.C. Stwalley, M. Aymar, and O. Dulieu. Detection by two-photon ionization and magnetic trapping of cold Rb_2 triplet state molecules. *Eur. Phys. J. D*, 39(2):261–269, 2006.

[59] H. K. Pechkis, D. Wang, Y. Huang, E. E. Eyler, P. L. Gould, , W. C. Stwalley, and C. P. Koch. Enhancement of the formation of ultracold $^{85}Rb_2$ molecules due to resonant coupling. *Phys. Rev. A*, 76(2):022504, 2007.

[60] W. C. Stwalley, J. Banerjee, M. Bellos, R. Carollo, M. Recore, and M. Mastroianni. Resonant coupling in the heteronuclear alkali dimers for direct photoassociative formation of $X(0,0)$ ultracold molecules. *J. Phys. Chem. A*, 114(1):81–86, December 2010.

[61] P. Zabawa, A. Wakim, M. Haruza, and N. P. Bigelow. Formation of ultracold $X\,^1\Sigma^+\,(v''=0)$ NaCs molecules via coupled photoassociation channels. *Phys. Rev. A*, 84:061401, December 2011.

[62] C. M. Dion, C. Drag, O. Dulieu, B. Laburthe Tolra, F. Masnou-Seeuws, and P. Pillet. Resonant coupling in the formation of ultracold ground state molecules via photoassociation. *Phys. Rev. Lett.*, 86:2253–2256, March 2001.

[63] O. Dulieu and A. Gerdes. Private communication, 2011.

[64] R. A. Cline, J. D. Miller, and D. J. Heinzen. Study of Rb_2 long-range states by high-resolution photoassociation spectroscopy. *Phys. Rev. Lett.*, 73:632–635, August 1994.

[65] H. Suemitsu and James A. R. Samson. Relative photoionization cross sections of Cs, Cs_2, Rb, and Rb_2. *Phys. Rev. A*, 28:2752–2758, November 1983.

[66] C. Amiot, O. Dulieu, and J. Vergès. Resolution of the apparent disorder of the Rb_2 $A\,^1\Sigma_u^+\,(0_u^+)$ and $b\,^3\Pi_u\,(0_u^+)$ spectra: A case of fully coupled electronic states. *Phys. Rev. Lett.*, 83:2316–2319, September 1999.

[67] R. de L. Kronig. Zur deutung der bandenspektren ii. *Z. Physik*, 50(5-6):347–362, 1928.

[68] C.-C. Tsai, T. Bergeman, E. Tiesinga, P. S. Julienne, and D. Heinzen. Preliminary report on an extended analysis of hyperfine structure in the $^{87}Rb_2\, 1_g$ state below $5\,^2S + 5\,^2P_{1/2}$. Private communication, 2012.

[69] Hélène Lefebvre-Brion and Robert W. Field. *The Spectra and Dynamics of Diatomic Molecules*. Elsevier Academic Press, 2004.

[70] Robert J. Le Roy, Nikesh S. Dattani, John A. Coxon, Amanda J. Ross, Patrick Crozet, and Colan Linton. Accurate analytic potentials for $Li_2(X\,^1\Sigma_g^+)$ and $Li_2(A\,^1\Sigma_u^+)$ from 2 to 90 Å, and the radiative lifetime of Li($2p$). *The Journal of Chemical Physics*, 131:204309, 2009.

[71] C. Gabbanini and O. Dulieu. Formation of ultracold metastable RbCs molecules by short-range photoassociation. *Phys. Chem. Chem. Phys.*, 13:18905–18909, 2011.

[72] Zhonghua Ji, Hongshan Zhang, Jizhou Wu, Jinpeng Yuan, Yonggang Yang, Yanting Zhao, Jie Ma, Lirong Wang, Liantuan Xiao, and Suotang Jia. Photoassociative formation of ultracold RbCs molecules in the $(2)\,^3\Pi$ state. *Phys. Rev. A*, 85:013401, January 2012.

[73] M. A. Bellos, R. Carollo, J. Banerjee, M. Ascoli, A.-R. Allouche, E. E. Eyler, P. L. Gould, and W. C. Stwalley. Upper bound to the ionization energy of $^{85}Rb_2$. *Phys. Rev. A*, 87:012508, January 2013.

[74] C. Amiot. Laser-induced fluorescence of Rb_2: The $1\,^1\Sigma_g^+\,(X)$, $2\,^1\Sigma_g^+$, $1\,^1\Pi_u\,(B)$, $1\,^1\Pi_g$, and $2\,^1\Pi_u\,(C)$ electronic states. *The Journal of Chemical Physics*, 93(12):8591–8604, 1990.

[75] C. Amiot and J. Vergès. Optical-optical double resonance and Fourier transform spectroscopy: The Rb_2 $B\,^1\Pi_u$ electronic state up to the quasibound energy levels. *Chemical Physics Letters*, 274(1-3):91 – 98, 1997.

[76] Ning Yi Du and Chris H. Greene. Interaction between a rydberg atom and neutral perturbers. *Phys. Rev. A*, 36:971–974, July 1987.

[77] Chris H. Greene, A. S. Dickinson, and H. R. Sadeghpour. Creation of polar and nonpolar ultra-long-range Rydberg molecules. *Phys. Rev. Lett.*, 85:2458–2461, September 2000.

[78] Edward L Hamilton, Chris H Greene, and H R Sadeghpour. Shape-resonance-induced long-range molecular Rydberg states. *Journal of Physics B: Atomic, Molecular and Optical Physics*, 35(10):L199, 2002.

[79] V. Bendkowsky, B. Butscher, J. Nipper, J. B. Balewski, J. P. Shaffer, R. Löw, T. Pfau, W. Li, J. Stanojevic, T. Pohl, and J. M. Rost. Rydberg trimers and excited dimers bound by internal quantum reflection. *Phys. Rev. Lett.*, 105:163201, October 2010.

[80] Chris H. Greene, Edward L. Hamilton, Heather Crowell, Cedomil Vadla, and Kay Niemax. Experimental verification of minima in excited long-range Rydberg states of Rb_2. *Phys. Rev. Lett.*, 97:233002, December 2006.

[81] Vera Bendkowsky, Bjorn Butscher, Johannes Nipper, James P. Shaffer, Robert Low, and Tilman Pfau. Observation of ultralong-range Rydberg molecules. *Nature*, 458:1005 – 1008, April 2009.

[82] W. Li, T. Pohl, J. M. Rost, Seth T. Rittenhouse, H. R. Sadeghpour, J. Nipper, B. Butscher, J. B. Balewski, V. Bendkowsky, R. Lw, and T. Pfau. A homonuclear molecule with a permanent electric dipole moment. *Science*, 334(6059):1110–1114, 2011.

[83] J. Tallant, S. T. Rittenhouse, D. Booth, H. R. Sadeghpour, and J. P. Shaffer. Observation of blueshifted ultralong-range Cs_2 Rydberg molecules. *Phys. Rev. Lett.*, 109:173202, October 2012.

[84] D. Booth, S. T. Rittenhouse, J. Yang, H. R. Sadeghpour, and J. P. Shaffer. Production of trilobite Rydberg molecule dimers with kilo-debye permanent electric dipole moments. *Science*, 348(6230):99–102, 2015.

[85] Matthew T. Eiles and Chris H. Greene. Ultracold long-range Rydberg molecules with complex multichannel spectra. *Phys. Rev. Lett.*, 115:193201, November 2015.

[86] Spectra-Physics LAB-150 specifications. `http://www.spectra-physics.com/products/high-energy-pulsed-lasers/quanta-ray-lab#specs`. Accessed: Nov. 9, 2015.

[87] E. Tiemann. Private communication, 2015.

[88] I. Temelkov, H. Knöckel, A. Pashov, and E. Tiemann. Molecular beam study of the $a\,^3\Sigma^+$ state of NaK up to the dissociation limit. *Phys. Rev. A*, 91:032512, March 2015.

[89] J. E. Sansonetti. Wavelengths, transition probabilities, and energy levels for the spectra of rubidium (Rb I through Rb XXXVII). *Journal of Physical and Chemical Reference Data*, 35(1):301–421, 2006.

[90] Luther Davis, Bernard T. Feld, Carrol W. Zabel, and Jerrold R. Zacharias. The hyperfine structure and nuclear moments of the stable chlorine isotopes. *Phys. Rev.*, 76:1076–1085, October 1949.